UNSTEADY FREE SURFACE WAVES IN A REGION OF ARBITRARY SHAPE

by

A. K. Otta, I. A. Svendsen and S. T. Grilli

Research Report No. CACR-92-10

CENTER FOR APPLIED COASTAL RESEARCH
Department of Civil Engineering
University of Delaware
Newark, Delaware 19716

TABLE OF CONTENTS

LIST OF FIGURES

LIST OF TABLES

ABSTRACT

Understanding and modeling the behavior of the free surface motion is complicated due to the nonlinear free surface conditions that must be satisfied on a nonstationary surface. In coastal and offshore engineering, interaction of the free surface with the sea bottom and man-made structures present several problems where it is significant to account for the exact nonlinear conditions. Viscosity and turbulence have significant influences if breaking occurs or flow separation takes place. In many instances, however, the potential theory can be used to obtain valuable information. In the present work, we consider exact modeling of the free surface motion based on the potential theory. The problem formulated as an IBVP (Initial Boundary Value Problem) is solved numerically through a combination of a boundary integral procedure and a Lagrangian evolution of the free surface. Earlier development of such a procedure has been mostly used to study evolution and overturning of the free surface with assumed periodicity over space. We pursue here an approach through which diverse problems can be simulated by allowing the lateral conditions to be modeled according to each problem.

The numerical solution of the Laplace equation is based on the boundary integral formulation derived by using the free space Green's function. The present two-dimensional computation is performed over the physical domain. This choice is inspired by the flexibility and the conceptual simplicity of a computational formulation over the physical domain. This has the further advantage that the model can be extended to a three-dimensional space in a relatively straight-forward manner. The numerical difficulties associated with the approach are discussed. It is shown that these difficulties can be removed and a higher order, accurate procedure can be achieved. Another important aspect analyzed in the present work is the consistency of the lateral conditions with the free surface conditions

and the 'desired' simulation (when no precise mathematical formulation of the physical process is available).

Several computations have been presented to show the validity and the accuracy of the model in a range of problems. The model has been applied to the analyses of very steep solitary waves. Besides the new results that have been obtained on the run-up of steep solitary waves on slopes, these applications demonstrate the practical and theoretical utilities of such a model.

Chapter 1

INTRODUCTION

1.1 Water Wave Problems and Free surface Nonlinearity

Water wave problems possess the salient feature of the presence of a free surface. Close to the shoreline, bottom variation and breaking add to the complexities of the phenomena. The surf zone, the usual terminology for the region between breaking and the shoreline, is marked by turbulence and dissipation of energy. Offshore of the breaking point, it has been customary to ignore the effect of viscosity and assume the flow to be potential. This is justifiable for short distance of propagation while dealing with gravity waves. The factors of significance in the regime of potential flow are the free surface nonlinearity and the interaction with the bottom topography or man-made structures.

For waves of small amplitude, linearization of the free surface offers tremendous simplifications and possible analytical solutions may be sought for guidance. Free surface nonlinearity may then be introduced at different levels of approximation. Approximate nonlinear solutions to steady wave propagation have been obtained by Stokes' perturbation in deep water and by the formulation of Boussinesq theory in intermediate or shallow water. These formulations have also been extended to unsteady problems and have brought about significant improvements in the understanding and predictability of nonlinear propagation. A notable exception is the nonlinear long wave theory which does not permit any steady form, but is used extensively for unsteady problems such as propagation and runup over slopes. Typically, these formulations reduce the dimensionality of the problem by a rational assumption of the shape of the variation along certain directions, (usually over depth in two dimensional problems). The simplified formulations also often yield to a frequency domain analysis. Substantial numerical advantages result as a consequence

of the simplifications and, in some instances, these simplifications offer the only viable schemes capable of analyzing waves over large domains (relative to the wave length) or wide frequency range. The major disadvantages associated with these formulations are:

1. Formulation of the procedure to higher order gets increasingly difficult. Applicability is restricted to only moderate wave heights.

2. The range of application is usually specific to either deep water or intermediate and shallow water.

3. Modeling velocity variations in the presence of uneven bottom or other disturbances in the form of floating and submerged objects is difficult.

Conceptually, a numerical procedure capable of solving the governing Laplace equation over an arbitrary domain and satisfying the nonlinear free surface conditions exactly should remove these difficulties. One assumes implicitly here that a proper numerical formulation of the physical phenomenon desired to be studied is possible and that the numerical scheme is accurate and stable. In the context of nonlinear wave motion both these aspects are not straight forward. The present study is an endeavor to look at these aspects and illustrate the advantages and limitations of such an approach in the modeling of water waves.

1.2 Basic Equations

Shown in fig. 1.1 is a typical fluid domain over which the motion has to be solved. The domain Ω is bounded by a free surface η, a bottom of varying depth $h(x)$ and two lateral boundaries. In addition, objects, submerged or partially floating, may also be present. Denoting the vector coordinates by $\mathbf{x}$, a scalar potential $\phi(\mathbf{x})$ can be defined for an irrotational velocity field $\mathbf{u}$ such that

$$\mathbf{u}(\mathbf{x}) = \nabla\phi(\mathbf{x}) \tag{1.1}$$

where the operator ∇ denotes the vector gradient. The continuity equation

$$\nabla \cdot \mathbf{u} = \mathbf{0} \tag{1.2}$$

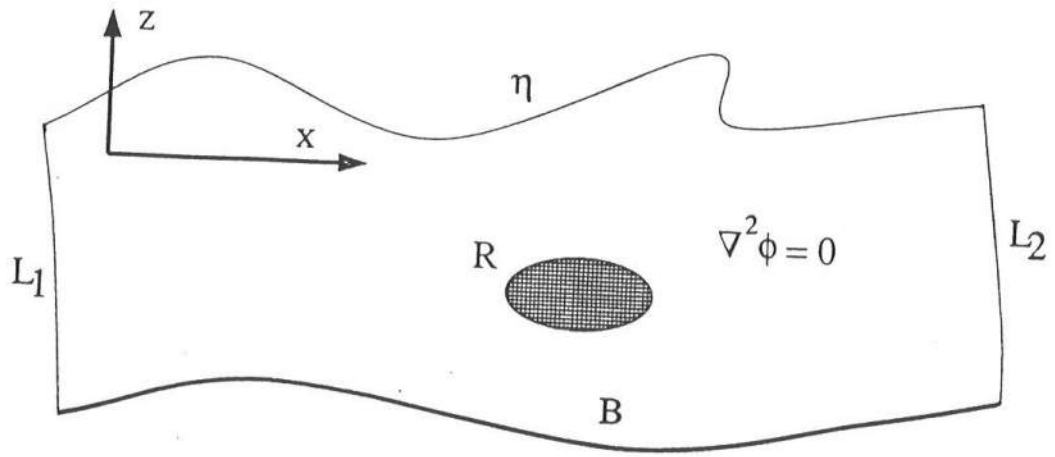

Figure 1.1: Schematic view of the domain. L_1 and L_2 represent the lateral sides. η, B and R represent the free surface, an impermeable bottom and the surface of a rigid body.

under the assumption of incompressibility leads to

$$\nabla^2\phi(\mathbf{x}) = 0; \quad \mathbf{x} \in \Omega. \tag{1.3}$$

Neglecting surface tension, the dynamic condition on the free surface is

$$P(\eta) = P_a \tag{1.4}$$

where P_a is the external applied pressure on η and $P(\eta)$ is fluid pressure just inside. With (1.4) the Bernoulli equation for unsteady irrotational flow becomes

$$\frac{\partial\phi}{\partial t} = -\frac{1}{2}|\mathbf{u}|^2 - gz - \frac{P_a}{\rho} + c_b(t); \quad \text{on } z = \eta. \tag{1.5}$$

The Bernoulli constant c_b, being only a function of time, may be absorbed in ϕ_t. From the kinematic condition on η the motion of a fluid particle on it is governed by

$$\frac{d}{dt}\mathbf{x}_p = \mathbf{u}(\mathbf{x}_p). \tag{1.6}$$

The subscript 'p' refers to a fluid particle and $\mathbf{x}_p$ is the position of the particle on the free surface. On a rigid surface R,

$$\phi_n(\mathbf{x}) = \mathbf{U}(\mathbf{x}) \cdot \mathbf{n}; \ \mathbf{x} \in \mathrm{R} \tag{1.7}$$

where ϕ_n, $\mathbf{n}$ and $\mathbf{U}$ are respectively the normal flux (outward of the fluid domain), the unit normal vector outward of the fluid domain on R and the velocity of R at $\mathbf{x}$. For an impermeable bottom B with no motion, this condition simplifies to

$$\phi_n(\mathbf{x}) = 0; \quad \mathbf{x} \in \mathrm{B}. \tag{1.8}$$

Boundary data on the lateral sides depend on the type of the problem studied. Some common forms of the lateral conditions are:

- spatial periodicity

- wave generation

- reflection from a vertical or a sloping wall

- wave radiation

Several different formulations are possible for wave generation or radiation, but these boundary data are normally of the Neumann or the Dirichlet type for the Laplace equation in the domain Ω.

1.3 Integral Representations of the Laplace equation

The fluid domain Ω is irregularly shaped and changing with time with the evolution of the free surface. Since the governing Laplace equation (1.3) has to be solved over a such domain, boundary integral method is best suited. The numerical grid points or the nodes are distributed only along the boundary in this method and can be easily adapted to a moving domain. The flow quantities at a point inside the computational domain can then be expressed in terms of the boundary values of ϕ and ϕ_n. This approach has been attempted by Svendsen (1971) in the context of investigating deformation of surface waves. Several integral representations of (1.3) are possible each offering different numerical advantages. Brief derivations of two familiar forms are presented in the following.

1.3.1 Integral Representation Based on Green's Theorem

For two functions f and g having continuous derivatives up to the second order, Green's second identity gives (*e.g.*, see Greenberg, 1978)

$$\int_{\Omega}(g\nabla^2 f - f\nabla^2 g)d\Omega = \int_{\Gamma}(gf_n - fg_n)d\Gamma \tag{1.9}$$

where the subscript 'n' denotes normal derivative on the boundary Γ of the domain Ω. We now consider a special function G which satisfies

$$\nabla^2 G(\mathbf{x},\mathbf{x}_0) = \delta(\mathbf{x}-\mathbf{x}_0) \tag{1.10}$$

and

$$\lim_{r\to\infty}\frac{\partial G}{\partial r} = 0 \tag{1.11}$$

where $\delta(\mathbf{x}-\mathbf{x}_0)$ is the Dirac delta function defined over the infinite space (called as the free space Green's function) in the same dimension of Ω. r is the distance from the point $\mathbf{x}_0$.

Let $\mathbf{x}_0$ be a point on Γ. We construct a new domain Ω' which is same as the domain Ω excluding a partial ball of radius ϵ around $\mathbf{x}_0$ (see fig. 1.2) and is bounded by Γ'. Since $\delta(\mathbf{x}-\mathbf{x}_0)$ is zero everywhere except at $\mathbf{x}=\mathbf{x}_0$, one has

$$\int_{\Gamma'}\left[G(\mathbf{x}-\mathbf{x}_0)\phi_n - \phi G_n(\mathbf{x}-\mathbf{x}_0)\right]d\Gamma' = \int_{\Omega'}\left[G(\mathbf{x}-\mathbf{x}_0)\nabla^2\phi - \phi\nabla^2 G(\mathbf{x}-\mathbf{x}_0)\right]d\Omega' = 0 \tag{1.12}$$

by replacing f and g by ϕ and G in (1.9) over the domain Ω'. As $\epsilon\to 0$, boundary Γ', excluding the partial circumference $c(\epsilon)$ around $\mathbf{x}_0$, tends to coincide with the boundary Γ leading to the relation

$$\begin{aligned}\int_{\Gamma}\left[G(\mathbf{x},\mathbf{x}_0)\phi_n - \phi G_n(\mathbf{x},\mathbf{x}_0)\right]d\Gamma &= \int_{\Gamma'}\left[G(\mathbf{x},\mathbf{x}_0)\phi_n - \phi G_n(\mathbf{x},\mathbf{x}_0)\right]d\Gamma' \\ &\quad - \int_{c(\epsilon)}\left[G(\mathbf{x},\mathbf{x}_0)\phi_n - \phi G_n(\mathbf{x},\mathbf{x}_0)\right]d\Gamma \\ &= -\int_{c(\epsilon)}\left[G(\mathbf{x},\mathbf{x}_0)\phi_n - \phi G_n(\mathbf{x},\mathbf{x}_0)\right]d\Gamma'. \end{aligned} \tag{1.13}$$

In order to evaluate the integral along $c(\epsilon)$, the function G must be specified. A function satisfying (1.10) and (1.11) in a two-dimensional space is

$$G(\mathbf{x},\mathbf{x}_0) = \frac{1}{2\pi}\ln r \tag{1.14}$$

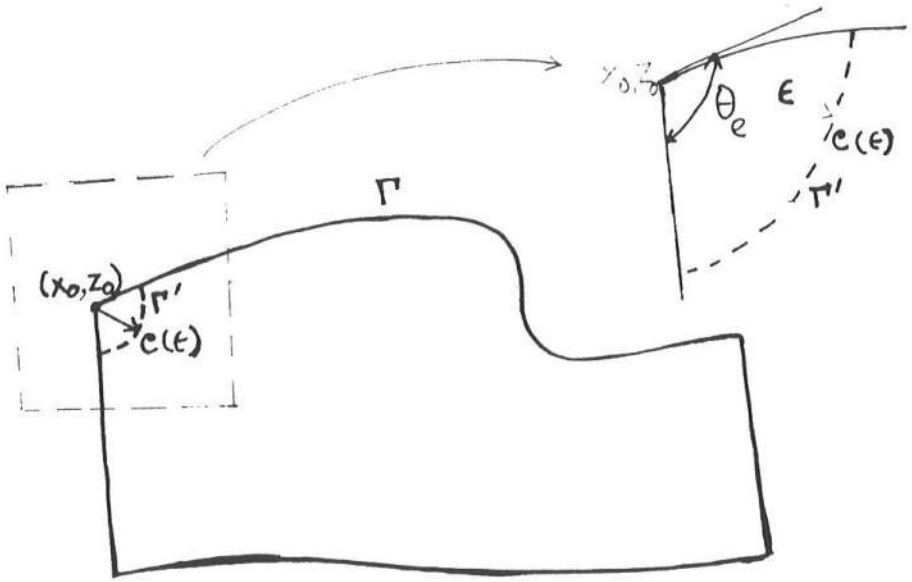

Figure 1.2: Definition sketch for the derivation of the integral equations. Boundary Γ' shown by the dotted line coincides with Γ (solid line) everywhere except for the partial circumference $c(\epsilon)$ around $\mathbf{x}_0$.

with $r = |\mathbf{x} - \mathbf{x}_0|$. G_n, the outward normal derivative to Γ', on $c(\epsilon)$ is

$$G_n(\mathbf{x}, \mathbf{x}_0) = -\left.\frac{\partial G(\mathbf{x}, \mathbf{x}_0)}{\partial r}\right|_{r=\epsilon} = -\frac{1}{2\pi\epsilon} \tag{1.15}$$

Using (1.14), (1.15) and $d\Gamma' = \epsilon d\theta$ on $c(\epsilon)$, one has

$$\int_{c(\epsilon)} \left[G(\mathbf{x}, \mathbf{x}_0)\phi_n - \phi G_n(\mathbf{x}, \mathbf{x}_0)\right] d\Gamma' = \frac{\epsilon \ln \epsilon}{2\pi} \int_{c(\epsilon)} \phi_n d\theta + \frac{1}{2\pi} \int_{c(\epsilon)} \phi d\theta. \tag{1.16}$$

ϕ being continuous in the partial ball of radius ϵ, it follows that

$$\lim_{\epsilon \to 0} \int_{c(\epsilon)} \phi d\theta = \theta_e(\mathbf{x}_0)\phi(\mathbf{x}_0) \tag{1.17}$$

where $\theta_e(\mathbf{x}_0)$ is the included angle at $\mathbf{x}_0$ between the two tangents to Γ and

$$\lim_{\epsilon \to 0} \frac{\epsilon \ln \epsilon}{2\pi} \int_{c(\epsilon)} \phi_n d\theta \leq \lim_{\epsilon \to 0} \frac{\epsilon \ln \epsilon}{2\pi} \theta_e \, |\phi_n|_{\max} = 0. \tag{1.18}$$

In arriving at the final equality in (1.18) it has been implicitly assumed that $|\phi_n|_{\max}$, the maximum absolute value of ϕ_n on $c(\epsilon)$, is bounded such that the limit exists. This condition and the continuity of ϕ assumed in the derivation are consistent with the restrictions

already set by the applicability of the Green's identity. Finally, using (1.18), (1.17) and (1.16) in (1.13) the following integral equation results:

$$\alpha(\mathbf{x}_0)\phi(\mathbf{x}_0) = \int_\Gamma [\phi G_n(\mathbf{x},\mathbf{x}_0) - \phi_n G(\mathbf{x},\mathbf{x}_0)]d\Gamma \tag{1.19}$$

with $\alpha(\mathbf{x}_0) = \theta_e(\mathbf{x}_0)/2\pi$. $\theta_e(\mathbf{x}_0)$ is π if $\mathbf{x}_0$ is on a smooth part of the boundary. (1.19) is the integral equivalent of (1.3).

1.3.2 Integral Representation Based on Cauchy's Theorem

A formulation due to Vinje and Brevig (1981) uses the Cauchy's theorem in the complex plane. Being based on the complex theory, the formulation is restricted to two-dimensional space.

Let ζ denote the complex variable $x+iz$. Since both the velocity potential ϕ and the stream function ψ satisfy the Cauchy-Riemann condition in the domain Ω, the complex potential $\phi + i\psi$ is analytic in Ω. According to the Cauchy's theorem (see Greenberg, 1978, p255),

$$\int_{\Gamma'} \frac{\phi + i\psi}{\zeta - \zeta_0} d\zeta = 0 \tag{1.20}$$

for a point ζ_0 lying outside the domain bounded by Γ' (fig. 1.2). The integral along the boundary Γ (in the sense of principal value) can be related to the integral along the boundary Γ' by letting $\epsilon \to 0$, *i.e.*,

$$\begin{aligned} \int_\Gamma \frac{\phi + i\psi}{\zeta - \zeta_0} d\zeta &= \lim_{\epsilon\to 0} \int_{\Gamma'} \frac{\phi + i\psi}{\zeta - \zeta_0} d\zeta - \lim_{\epsilon\to 0} \int_{c(\epsilon)} \frac{\phi + i\psi}{\zeta - \zeta_0} d\zeta \\ &= -\lim_{\epsilon\to 0} \int_{c(\epsilon)} \frac{\phi + i\psi}{\zeta - \zeta_0} d\zeta. \end{aligned} \tag{1.21}$$

Under the assumption that $\phi + i\psi$ is bounded and continuous in the partial ball around ζ_0, one has

$$\lim_{\epsilon\to 0} \int_{c(\epsilon)} \frac{\phi + i\psi}{\zeta - \zeta_0} d\zeta = [\phi + i\psi](\zeta_0) \lim_{\epsilon\to 0} \int_{c(\epsilon)} \frac{1}{\zeta - \zeta_0} d\zeta. \tag{1.22}$$

Using the relations

$$\zeta - \zeta_0 = \epsilon \exp(-i\theta), \tag{1.23}$$

$$d\zeta = -i\epsilon \exp(i\theta) d\theta \tag{1.24}$$

on $c(\epsilon)$, the integral in (1.22) reduces to

$$\begin{aligned}[\phi + i\psi](\zeta_0) \lim_{\epsilon \to 0} \int \frac{1}{\zeta - \zeta_0} d\zeta &= -[\phi + i\psi](\zeta_0) \int i d\theta \\ &= -i\theta_e(\zeta_0)[\phi + i\psi](\zeta_0). \end{aligned} \tag{1.25}$$

As before, $\theta_e(\zeta_0) = \pi$ in (1.25) if ζ_0 is on a smooth part of of the boundary. At a corner[1] $\theta_e(\zeta_0)$ assumes the value of the included angle between the two intersecting sides. Using (1.25) and (1.22) in (1.21), one obtains

$$-i\theta_e[\phi + i\psi](\zeta_0) + \int_\Gamma \frac{\phi + i\psi}{\zeta - \zeta_0} d\zeta = 0. \tag{1.26}$$

Splitting the real and imaginary parts of (1.26) yields

$$\theta_e(\zeta_0)\psi(\zeta_0) + \mathrm{Re} \int_\Gamma \frac{\phi + i\psi}{\zeta - \zeta_0} d\zeta = 0, \tag{1.27}$$

$$\theta_e(\zeta_0)\phi(\zeta_0) - \mathrm{Im} \int_\Gamma \frac{\phi + i\psi}{\zeta - \zeta_0} d\zeta = 0. \tag{1.28}$$

(1.27) is of the Fredholm's second type if ϕ is specified as the boundary condition. Conversely, (1.28) is of the Fredholm's second type for ψ specified on the the boundary. This feature allows an iterative solution and thus, (1.27) and (1.28) provide an efficient computational formulation in two-dimensional space.

In fact, (1.27) and (1.28) are valid for any analytical complex function in place of $\phi + i\psi$. Hence, for the complex velocity q defined as $q(\zeta) = [u - iw](\zeta)$, one has

$$-i\theta_e[u(\zeta_0) - iw(\zeta_0)] + \int_\Gamma \frac{u - iw}{\zeta - \zeta_0} d\zeta = 0. \tag{1.29}$$

Instead of u, w in (1.29), it is convenient to obtain an equivalent formulation in terms of ϕ_s, velocity along the boundary and ϕ_n, velocity normal to it. Along a boundary one has

$$u - iw = (\phi_s - i\phi_n)\frac{d\zeta^*}{ds} \tag{1.30}$$

where ds is an elemental length along the boundary and the superscript '*' denotes the complex conjugate. Using (1.30) in (1.26), one obtains

$$-i\left[\theta_e(\phi_s - i\phi_n)\frac{d\zeta^*}{ds}\right](\zeta_0) + \int_\Gamma \frac{\phi_s - i\phi_n}{\zeta - \zeta_0} ds = 0 \tag{1.31}$$

---

[1] In Vinje and Brevig (1981), θ_e has been assumed to be π. This is not true if the point ζ_0 is a corner point.

which, upon multiplication of $[d\zeta/ds](\zeta_0)$, gives

$$-i[\theta_e(\phi_s - i\phi_n)](\zeta_0) + \frac{d\zeta}{ds}(\zeta_0)\int_\Gamma \frac{\phi_s - i\phi_n}{\zeta - \zeta_0} ds = 0. \tag{1.32}$$

(1.32) can also be split to real and imaginary parts forming a pair of Fredholm's equation of the second type similar to (1.27) and (1.28). In some physical situations it is easier to construct the boundary conditions in terms of velocities (ϕ_s, phi_n) than in terms of the stream function and the potential. Computational formulation based on (1.32) has an advantage over that based on (1.26) in those situations. (1.32) is the basis of the formulation used by Dold & Peregrine (1986).

1.4 A Brief Review of Related Work

Methods satisfying the exact free surface conditions have existed for a long time (*e.g.*, Zaroodny & Greenberg, 1973). It is, however, after the work of Longuet-Higgins & Cokelet (1976) (hereafter referred to as 'L & C') that efforts in this direction gained momentum. A significant contribution of their work is the first successful demonstration of overtuning of steep waves on deep water.

The basic idea of the numerical scheme adopted by L & C is that the evolution of the free surface elevation η and potential ϕ is carried out by satisfying the exact conditions from an initial specification of η and ϕ. The velocity $\mathbf{u}$ on the free surface, necessary to determine the rate of the evolution, is determined by solving the integral equation (1.19). Instead of solving (1.19) over the actual fluid domain (which becomes infinite or very large along the depth for deep water), numerical solution is performed over a transformed domain. Assuming lateral periodicity in space, they consider a fluid domain (fig. 1.3) [2] extending over one wave length. The fluid domain is bounded by

$$0 \le x \le 2\pi; \quad -h \le z \le \eta \tag{1.33}$$

where the spatial coordinates x and z are normalized by $2\pi/\lambda$, λ being the wave length. A conformal mapping

$$r\exp(i\theta) = \exp(-i\zeta) \tag{1.34}$$

[2] A bottom at a finite depth is shown in the figure, though depth was assumed to be infinite in the work of Longuet-Higgins & Cokelet (1976).

is then used to map the fluid domain (left part of fig. 1.3) to a domain bounded by smooth contours. As shown in fig. (1.3), the free surface forms the contour C_1 and the two lateral

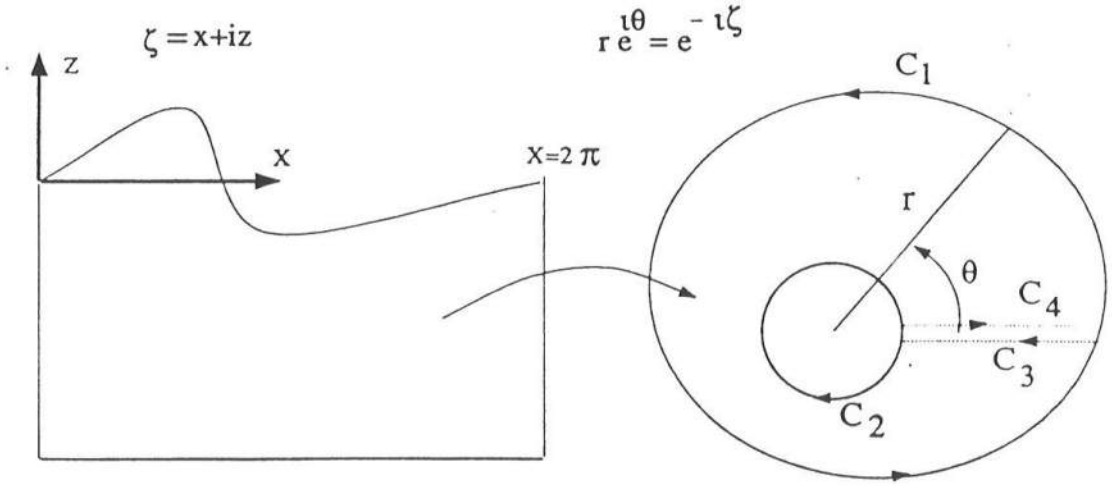

Figure 1.3: Conformally mapped domain

boundaries coalesce to $\theta = 0$ and $\theta = 2\pi$ respectively. Solution of (1.19) in the transformed domain is significantly simplified since the integrals along the lateral boundaries (C_3 and C_4) cancel each other under the assumption of periodicity. Consequently, the integration needs to be done only along two smooth contours C_1 and C_2. For infinite depth, as in the case of L & C, C_2 vanishes. This results in a a Dirichlet problem in the domain bounded by C_1 since the potential ϕ is specified as the boundary condition on the free surface or equivalently, on C_1. (1.19) subject to Dirichlet condition on the boundary is a Fredholm's equation of the first type and the integral equation is solved noniteratively.

The free surface becomes multiple-valued in the Cartesian coordinates during overturning. A Cartesian description of the free surface therefore becomes invalid during the development of a plunging breaker. L & C avoided this difficulty by adopting a Lagrangian description of the free surface. In this approach, the free surface is identified by a set of

discrete fluid particles on it. The position of a particle (or a computational node point) is governed by (1.6) whereas the evolution of ϕ following a free surface particle is given by

$$\frac{d\phi}{dt} = \frac{1}{2}|\mathbf{u}(\mathbf{x}_p)|^2 - gz_p - \frac{P_a}{\rho}. \tag{1.35}$$

A fourth order predictor-corrector approach, known as Adam-Bashforth-Multen (ABM) method, was used to carry out the numerical evolution of η and ϕ through (1.6) and (1.35) (since the computation was performed in the transformed domain, the actual numerical operation had also to be performed on the evolution equations expressed in the transformed domain). In the ABM method, the predicted value Y_{1p} and its corrected value Y_{1c} of a function Y after a time step Δt are given by

$$Y_{1p} = Y_0 + \frac{\Delta t}{24}(55Y'_0 - 59Y'_{-1} + 37Y'_{-2} - 9Y'_{-3}), \tag{1.36}$$

$$Y_{1c} = Y_0 + \frac{\Delta t}{24}(9Y'_{1p} + 19Y'_0 - 5Y'_{-1} + Y'_{-2}). \tag{1.37}$$

Y'_j in (1.36) and (1.37) denotes the time derivative of Y at $j\Delta t$ from the present time level. $\mathbf{x}_{p_{1c}}$ or ϕ_{1c} can be calculated from (1.36) and (1.37) by letting Y denote either $\mathbf{x}_p$ or ϕ. With η and ϕ known at time t_0, $d\mathbf{x}_p/dt$ and $d\phi/dt$ can be computed from (1.6) and (1.35) respectively after solving the Laplace equation to obtain u. Similarly, $d\mathbf{x}_{1p}/dt$ and $d\phi_{1p}/dt$ can be computed by solving the Laplace equation with ϕ_{1p} specified on η_{1p}.

A major disadvantage of using the ABM method is that the Laplace equation needs to be solved in two different domains at each time step to compute Y'_0 and Y'_{1p}. Further, the time step Δt needs to be constant during the entire computation since the procedure uses data from the previous time steps. The requirement of a constant time step is a serious constraint on the computational efficiency in applications where a smaller time step is necessary only over partial duration of the computation.

Following L & C, Vinje and Brevig (1981) presented a model in the physical space using a formulation based on (1.27) and (1.28). Similar to L & C, a Lagrangian description of the free surface is adopted and the the temporal evolution is described by a fourth order predictor-corrector approach, called the Hamming method. The choice of (1.27) and (1.28) gives the advantage that the integral equations can be solved iteratively

saving computational time. In addition, being formulated in the physical space with no assumption of lateral periodicity the model can be used to study interaction of waves with a bottom of varying depth and structures. The procedure, however, can not be extended to a three-dimensional space. Kim *et al.* (1983) studied run-up of solitary waves on steep slopes using a boundary integral method based on (1.19). They, however, did not adopt a Lagrangian description of the free surface. Instead, a modified Eulerian description was adopted. As a result, the procedure could not be applied to investigate phenomena involving overturning of the free surface.

Besides the formulations based on (1.19) or (1.26), a third type of integral equation based on vortex distribution was used by Zaroodny & Greenberg (1973), Baker *et al.* (1982) and Stansby & Slaouti (1984). In one of the most detailed descriptions, Baker *et al.* (1982) have shown the validity of this approach in modeling water waves in two-dimensional space. Though the formulation can in principle be extended to three-dimensions with the advantage of being iteratively solvable (see the discussion in Baker *et al.*, 1982) details of the formulation become quite complicated if floating bodies or submerged structures are to be included.

Dold and Peregrine (1986) (hereafter referred to as D & P) introduced a distinctly different higher order scheme to carry out the numerical evolution. They also obtained an efficient boundary integral solution of the Laplace equation. However, their formulations are based on the assumption of uniform depth and lateral periodicity. In a hypothetical fluid domain bounded by the free surface and its reflection about the bottom ($z = -h$), the physical condition of no flux through the bottom is satisfied by specifying

$$q^*(\zeta(\eta) - 2ih) = q(\zeta(\eta)) \tag{1.38}$$

where $q(\zeta)$ denotes the complex velocity, $u - iv$, at a point ζ and q^* is its complex conjugate. Using the mapping (1.34) D & P transformed the fluid domain between the free surface and its image to a domain bounded by two curves similar to that in L & C. The Laplace equation in this domain was solved by a boundary integral method based on (1.32). Using the relation (1.38) the integral along the reflection of the free surface in the transformed plane can be expressed in terms of the integral along the free surface. Consequently,

the only relevant boundary for the purpose of the numerical scheme is the free surface or equivalently, C_1 (fig. 1.3) in the transformed domain. The integral equation over the transformed domain was iteratively solved.

A distinct feature of the computational model of D & P is the scheme for numerical evaluation of the evolution equations (1.6) and (1.35). In marked difference to the implicit scheme used earlier by L & C, Vinje & Brevig (1981) and Baker *et. al* (1982), they developed a procedure for a higher order explicit scheme. This scheme is further discussed in chapter 2 in connection with the present work. Briefly, it proceeds as follows. $Y(t_0+\Delta t)$, value of a function Y at $t_0 + \Delta t$ is given by Taylor's expansion to be

$$Y(t_0 + \Delta t) = Y(t_0) + \Delta t Y'(t_0) + \frac{\Delta t^2}{2} Y''(t_0) + \cdots \tag{1.39}$$

where the superscript '$\prime$' denotes differentiation with respect to time. Denoting the Lagrangian position $\mathbf{x}_p$ or potential ϕ of a fluid particle on the surface by Y, we notice that the first derivative $Y'(t_0)$ is available after the solution of the Laplace equation for the velocity potential ϕ. In order to be able to use a higher order scheme, $Y'(t_0), Y''(t_0), \cdots$ need to be known. D & P utilized the fact that

$$\nabla^2 \left(\frac{\partial \phi}{\partial t} \right) = \nabla^2 \left(\frac{\partial^2 \phi}{\partial t^2} \right) = \cdots = 0 \tag{1.40}$$

since ϕ satisfies the Laplace equation $\nabla^2 \phi = 0$. In addition, it is possible to formulate the boundary conditions for each of these Laplace equations in a sequential manner. D & P showed (described in more details in chapter 2) that each higher order derivative in (1.39), *i.e.*, $d^2\mathbf{x}/dt^2$, $d^3\mathbf{x}/dt^3$ *etc.* for the position $\mathbf{x}$ and $d^2\phi/dt^2$, $d^3\phi/dt^3$ *etc.* for the potential ϕ could be obtained by solving in succession $\nabla^2\phi_t = 0$, $\nabla^2\phi_{tt} = 0$ *etc.* and using the conditions on the free surface. In principle, the scheme can be expanded to any order. This procedure for temporal evolution is later followed by Seo & Dalrymple (1990) in a model for periodic waves over finite depth.

Two distinct computational advantages result. Since the solution of each additional Laplace equation in ϕ_t, ϕ_{tt} *etc.* requires only a small fraction of the CPU time used for solving the first one, higher order updating is very efficient. Secondly, the time step Δt is free to be varied during the temporal evolution. This is particularly useful when smaller

time step should be used only over a short duration during the computation. It was also reported by D & P that the saw-tooth instability, observed during overturning in the work of L & C, was less prominent while using their model for similar situations. However, no insight was provided as to the reduction of the saw-tooth instability. Since the basic integral equations, the evolution scheme and the order of accuracy of the implemented numerical schemes are so very different, it is difficult to attribute this phenomenon to any single factor.

A two-dimensional computational model for nonlinear free surface flows with general applicability was introduced by Grilli *et al.* (1988, 89). In analogy with a physical wave tank, they conceived a "numerical wave tank" with the three basic elements of wave generation, wave propagation and radiation. The problem is formulated in the the physical domain using (1.19) as the integral representation of (1.3). The model is valid for a fluid domain of arbitrary shape with the boundary conditions being either of the Dirichlet or the Neumann type. A Lagrangian description of the free surface allows application of the model to wave motion that develop overturning surface. Numerical evaluation of the evolution equation is carried out explicitly to second order accuracy (truncation error is proportional to $(\Delta t)^3$) by extending the formulation of D & P to the computation over the physical domain. This computational model is again discussed in some details in chapter 2. A similar approach has also been pursued in Cointe (1990).

1.5 Description of the Present Study

In the present work we consider the physical and numerical aspects of a computational model satisfying the exact free surface conditions. Further, we require that the model be valid for bottoms of varying depth and presence of structures inside the fluid domain. Assumption of lateral periodicity as in L & C and D & P is no longer a valid choice. At the same time, a host of diverse situations can be simulated if we leave the boundary conditions on the lateral sides free to be specified. This flexibility can be accommodated in a computational model if the computation is done over the actual physical domain. One of the concerns then is that the specified boundary conditions lead to computationally

stable and physically desirable phenomena. To achieve understanding of these aspects we limit ourselves to only two-dimensional wave motions in the present dissertation.

A basic computational model with these scopes is that proposed by Grilli *et al.* (1989). An alternative formulation is that of Vinje & Brevig (1981) with the advantage that the integral equation is of the second kind. However, being based on the complex theory this formulation is limited to two-dimensional domains. This is a drawback since one of the underlying goals of the present work is that the knowledge gained from the two-dimensional model directly aids in developing a three-dimensional computational model. We have therefore adopted the model of Grilli *et al.* (1988, 89) as the basic framework.

The formulation based on Green's theorem has inherent numerical disadvantages compared to the formulations used by D & P and Vinje & Brevig (1981) over domains whose boundary is of the Dirichlet type (along the entire length or a large part) as in the case of nonlinear free surface flows. In addition, since the entire domain is discretized in the present model as opposed to only the free surface in the case of L & C and D & P, the computational efforts are significantly higher. Further difficulties are anticipated at the corners both in the solution of the Laplace equation and the temporal evolution of the free surface in the computation over the physical domain. Thus, sufficient care is necessary to ensure accuracy and stability of the method if reliable results are to be expected in application to diverse problems.

Finally, application of the method to some selected problems is considered with a view to emphasizing the theoretical and practical importance of such a procedure. Some of the problems considered go clearly beyond the validity of the approximate nonlinear methods like the nonlinear shallow water theory or the Boussinesq equations and some stress upon the need to account for the real bottom and the lateral conditions along with the exact modeling of the free surface nonlinearity.

1.6 Nondimensionalization Used in the Dissertation

The equations and derivations in the text are expressed in dimensional coordinates. However, the variables in the plots are presented in nondimensional form unless otherwise explained. The nondimensionalization is based on the following:

Length Scale The length scale for nondimensionalization is a representative depth of water h, which in most cases will be the uniform depth of water. Thus, $x^* = x/h$, $z^* = z/h$, $H^* = H/h$ and $L^* = L/h$. '*' denotes the nondimensional values.

Time Scale The time scale is the time taken for the shallow water wave to travel one unit length scale, which is $\sqrt{h/g}$. Thus, $t^* = t\sqrt{g/h}$.

With the length scale and time scale defined as above,
$\phi^* = \phi/(h\sqrt{gh})$, $u^* = u/\sqrt{gh}$, $u_t^* = u_t/g$ and $p^* = p/(\rho gh)$.
The superscript '' will be assumed implicit in the figures, unless otherwise specified.*

1.7 Outline of the Dissertation

The presentation of the work is organized in the following manner:

In chapter 2, the computational procedure adopted in this work is described. Besides the present developments, this includes the formulations and the algorithms reported in the earlier work by Grilli *et al.* (1988, 89).

Chapter 3 deals with the computational aspects of corners in a Boundary Integral model. Errors near a corner in the solution of nonsingular flows have been analyzed. Additional problems at the intersection of a moving boundary are discussed and a remedy is presented.

Chapter 4 discusses the issues involved in wave generation in a laboratory wave tank and a numerical model. Numerical generation of waves is verified by comparing with analytical results based on both linear and lower order nonlinear theories. Wave modulation due to the exact nonlinear conditions at the free surface and the wave maker is analyzed.

Radiation of nonlinear waves is discussed in chapter 5. A stable procedure is attained through a new numerical formulation of the radiation condition and has been shown to be highly accurate in case of waves of permanent form. Difficulties and some approximate methods are discussed for the application of the radiation condition to non-permanent waves. Chapters 4 and 5 form an important aspect of relating a finite domain computational model to an open sea.

Chapter 6 presents an application of the computational model to the study of steep solitary waves. A critical analysis of accuracy during the propagation of an extremely high solitary wave is undertaken. Runup of steep solitary waves on different slopes are studied and some aspects of breaking on the beach are discussed.

In chapter 7 an overall view of the undertakings in this dissertation is presented and some of the limitations are discussed along with suggestions of some future developments.

Chapter 2

COMPUTATIONAL PROCEDURE

2.1 Introduction

One of the peculiarities of nonlinear free surface motion is that the free surface defining a portion of the boundary enclosing the computational domain is nonstationary. The evolution of the free surface is governed by the kinematic and the dynamic conditions which are to be evaluated on the free surface. Thus, two basic steps in the numerical solution at a time level t are:

1. Solution of the governing Laplace equation subject to the boundary conditions at that instant. The solution provides the values necessary to determine the evolution of the free surface.

2. Evaluation of the new position of the free surface and the boundary data on it for the time level $t + \Delta t$.

A typical fluid domain is shown in fig. 2.1. The domain is bounded by the free surface, a bottom of varying depth and the lateral sides. In the presence of a submerged object, the fluid domain can be defined by a branch cut. Along with the evolution of the free surface, the boundary conditions and the geometrical positions of the lateral boundaries are to be determined at each time step. This aspect is no less critical than an accurate evolution of the free surface in computations over a physical domain. However, updating of the lateral boundaries depends on the type of the problem and we defer the description of the procedures to be undertaken in the context of the problems studied in the later chapters.

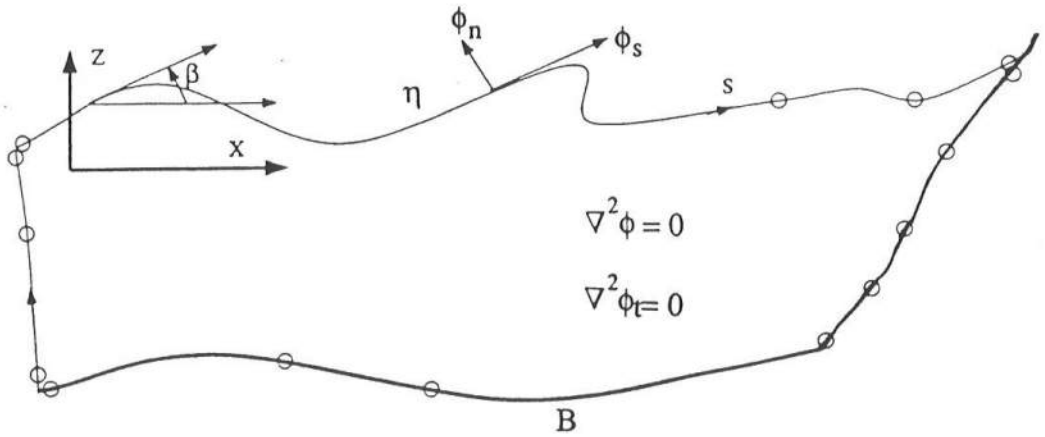

Figure 2.1: Sketch of a typical computational domain

2.2 Shape Function Approximation and Mapping

It is convenient to introduce the concept of shape functions (Banerjee & Butterfield, 1981 and Zienkiewicz & Morgan, 1983) here before proceeding with the computational procedure. The shape functions provide a computationally efficient local basis for approximation to the variation of the function based on its values at discrete nodal points.

A shape function $N_l(\mu)$ (fig. 2.2) is defined over $-1 \leq \mu \leq 1$ such that

$$\begin{aligned} N_l(\mu) &= 1;\ \mu = \mu_l \\ &= 0;\ \mu = \mu_m,\ m \neq l;\ (l, m = 1, 2, \cdots, jn) \end{aligned} \tag{2.1}$$

where jn is the number of nodes and

$$\mu_m = -1 + \frac{2}{jn - 1}(m - 1). \tag{2.2}$$

From (2.1), it is clear that $N_l(\mu)$ is a member of the Lagrange polynomials of order $(jn-1)$. Consider now the variation of a function $\mathcal{F}(\mu)$ over $-1 \leq \mu \leq 1$. Using the shape functions $\mathcal{F}^*(\mu)$, an approximation to $\mathcal{F}(\mu)$, is given in terms of its nodal values by

$$\mathcal{F}^*(\mu) = \mathcal{F}_l N_l(\mu);\ 1 \leq l \leq jn \tag{2.3}$$

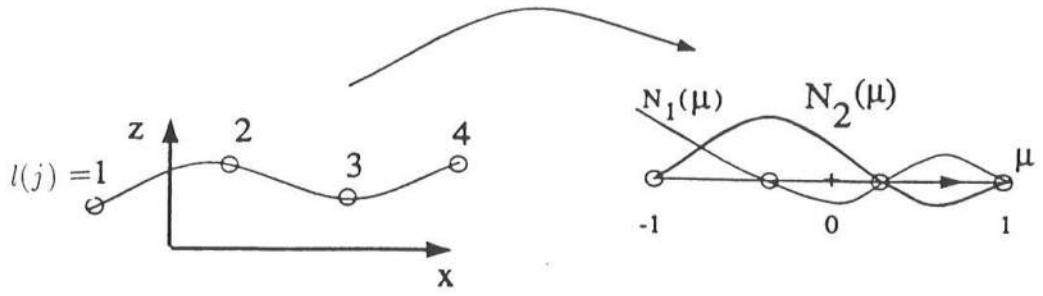

Figure 2.2: Shape functions and local mapping. $l(j)$ represents the local sequence l of the node j.

where $\mathcal{F}_l$ is the value of $\mathcal{F}(\mu)$ at the node l.

In the mapping of an interval consisting of jn nodes in the global coordinates (shown in the left of fig. 2.2) to the interval $[-1 \leq \mu \leq 1]$, $\mathcal{F}_l$ is same as the discrete value of the function at the node $j(l)$. $j(l)$ is the node in the global coordinates which is mapped to the node l. Conversely, we shall use $l(j)$ to denote the local index in the interval $[-1 \leq \mu \leq 1]$ of the node j. In order to complete the mapping (x, z) should be expressed in terms of μ. If the same shape function approximation is again used, *i.e.*,

$$\begin{aligned} x(\mu) &= x_{l(j)} N_l(\mu), \\ z(\mu) &= z_{l(j)} N_l(\mu);\ 1 \leq l \leq jn \end{aligned} \tag{2.4}$$

the mapping is known as isoparametric. It is, however, possible to use different mappings for the variation of the geometry and the function $\mathcal{F}$. An important advantage of isoparametric mapping is that the order of the approximation can be increased easily by including more number of nodes in the element. Further, the nodes in the x, z coordinates need not be uniformly spaced even though the nodes in $[-1 \leq \mu \leq 1]$ are placed at equal intervals.

2.3 Free Surface Updating

From a known value at time t_0, the change in a function $\mathcal{F}(t)$ after a short time interval Δt can be explicitly determined by the Taylor's expansion

$$\mathcal{F}(t_0 + \Delta t) = \mathcal{F}(t_0) + \Delta t \frac{d\mathcal{F}}{dt}(t_0) + \Delta t^2 \frac{d^2\mathcal{F}}{dt^2}(t_0) + O(\Delta t^3). \tag{2.5}$$

With reference to a Lagrangian description of the free surface, $\mathcal{F}$ in (2.5) denotes the Lagrangian coordinates $\mathcal{X}, \mathcal{Z}$ or the potential ϕ of a fluid particle on the free surface and the operator d/dt denotes the material derivative following the fluid particle. In the boundary integral model, ϕ, ϕ_t $(\partial\phi/\partial t)$ and their normal derivatives ϕ_n, ϕ_{tn} are explicitly known along the boundary. Thus, it is most convenient to express the derivatives $d\mathcal{F}/dt$ and $d^2\mathcal{F}/dt^2$ in terms of these quantities in order to determine the evolution through (2.5).

2.3.1 Lagrangian Derivatives Along the Free Surface

We consider the formulations for $d\phi/dt$ and $d\phi^2/dt^2$ along the free surface. From the dynamic condition on the free surface, one has

$$\frac{d\phi}{dt} = \frac{1}{2}(u^2 + w^2) - g\mathcal{Z} - \frac{P_a}{\rho} \tag{2.6}$$

where u and w represent the horizontal and the vertical velocity of a fluid particle on the surface, P_a denotes the atmospheric pressure and ρ the density of water. From fig. 2.1 it follows that

$$u = \phi_s \cos\beta - \phi_n \sin\beta, \tag{2.7}$$

$$w = \phi_s \sin\beta + \phi_n \cos\beta \tag{2.8}$$

where the subscript 's' denotes a derivative along the surface and β is the angle between the tangent and the x-axis. Using (2.7) and (2.8) in (2.6) one obtains

$$\frac{d\phi}{dt} = \frac{1}{2}(\phi_s^2 + \phi_n^2) - g\mathcal{Z} - \frac{P_a}{\rho}. \tag{2.9}$$

We show later how ϕ_s in (2.9) is derived from ϕ along the free surface. Thus, (2.9) gives the rate of evolution of ϕ following a fluid particle on the surface whose Lagrangian coordinates are $\mathcal{X}, \mathcal{Z}$.

An expression for $d^2\phi/dt^2$ is obtained by considering the operation d/dt on (2.6), *i.e.*,

$$\begin{aligned}\frac{d^2\phi}{dt^2} &= uu_t + ww_t + u(uu_x + ww_x) + w(uu_z + ww_z) \\ &\quad -g\frac{d\mathcal{Z}}{dt} - \frac{1}{\rho}\frac{dP_a}{dt}\end{aligned} \tag{2.10}$$

where each of the subscripts t, x and z denotes a derivative with respect to that variable. Similar to (2.7) and (2.8), it follows that

$$u_t = \phi_{ts}\cos\beta - \phi_{tn}\sin\beta, \tag{2.11}$$

$$w_t = \phi_{ts}\sin\beta + \phi_{tn}\cos\beta. \tag{2.12}$$

Next, we turn to the terms $(uu_x + ww_x)$ and $(uu_z + ww_z)$ in (2.10). Using (2.7) and (2.8), one can write

$$uu_x + ww_x = \phi_s[\cos\beta u_x + \sin\beta w_x] + \phi_n[-\sin\beta u_x + \cos\beta w_x]. \tag{2.13}$$

Recognizing that

$$\frac{d}{ds} = \frac{dx}{ds}\frac{\partial}{\partial x} + \frac{dz}{ds}\frac{\partial}{\partial z} = \cos\beta\frac{\partial}{\partial x} + \sin\beta\frac{\partial}{\partial z} \tag{2.14}$$

and

$$w_x = u_z;\ u_x = -w_z \tag{2.15}$$

for potential flow, (2.13) becomes

$$uu_x + ww_x = \phi_s\frac{d}{ds}u + \phi_n\frac{d}{ds}w. \tag{2.16}$$

Similarly, one obtains

$$uu_z + ww_z = \phi_s\frac{d}{ds}w - \phi_n\frac{d}{ds}u. \tag{2.17}$$

The kinematic condition on the surface gives

$$\frac{dZ}{dt} = w = \phi_s\sin\beta + \phi_n\cos\beta. \tag{2.18}$$

Using (2.11), (2.12), (2.16), (2.17), (2.7), (2.8) and (2.18) in (2.10) with u and w replaced respectively by by (2.7) and (2.8), one finally obtains

$$\begin{aligned}\frac{d^2\phi}{dt^2} = {} & \phi_s\phi_{ts} + \phi_n\phi_{tn} + \phi_s(\phi_s\phi_{ss} + \phi_n\phi_{ns}) \\ & -\phi_n(\phi_n\phi_{ss} - \phi_s\phi_{ns}) + \phi_n\beta_s(\phi_s^2 + \phi_n^2) \\ & -g(\phi_n\cos\beta + \phi_s\sin\beta) - \frac{1}{\rho}\frac{dP_a}{dt}.\end{aligned} \tag{2.19}$$

Equation (2.19) gives an expression for $d^2\phi/dt^2$ in terms of the free surface quantities. Expressions (2.9) and (2.19) are identical to those already used in Grilli *et al.* (1989).

Following similar procedures, the derivatives $d\mathcal{X}/dt$, $d\mathcal{Z}/dt$, $d\mathcal{X}^2/dt^2$ and $d\mathcal{Z}^2/dt^2$ can be derived in terms of the free surface quantities and their derivatives along the free surface. These expressions, satisfying the exact nonlinear free surface conditions, are

$$\frac{d\mathcal{X}}{dt} = \phi_s \cos\beta - \phi_n \sin\beta, \tag{2.20}$$

$$\frac{d\mathcal{Z}}{dt} = \phi_s \sin\beta + \phi_n \cos\beta, \tag{2.21}$$

$$\begin{aligned}\frac{d^2\mathcal{X}}{dt^2} &= \cos\beta\left[\phi_{ts} + \phi_s\phi_{ss} + \phi_n\phi_{ns}\right] + \\ &\quad \sin\beta\left[\phi_n\phi_{ss} - \phi_s\phi_{ns} - \phi_{tn} - \beta_s(\phi_s^2 + \phi_n^2)\right],\end{aligned} \tag{2.22}$$

$$\begin{aligned}\frac{d^2\mathcal{Z}}{dt^2} &= \cos\beta\left[\phi_{tn} - \phi_n\phi_{ss} + \phi_s\phi_{ns} + \beta_s(\phi_s^2 + \phi_n^2)\right] + \\ &\quad \sin\beta\left[\phi_{ts} + \phi_s\phi_{ss} + \phi_n\phi_{ns}\right].\end{aligned} \tag{2.23}$$

2.3.2 Computational Evaluation of the Lagrangian Derivatives

In order to compute the evolution of the free surface at time level t_0, the terms on the right hand sides of (2.9), (2.19) and (2.20)-(2.23) should be available. The derivative of a function along the free surface, denoted by d/ds or the subscript 's', can be computed in terms of its values at the neighboring nodal points. The exact numerical procedure is described in the following subsection.

The normal flux ϕ_n on the free surface η is obtained by solving the Laplace equation $\nabla^2\phi = 0$ with the appropriate boundary conditions on the boundary Γ. With ϕ (hence, ϕ_s) and ϕ_n known on η, ϕ_t is obtained from the dynamic condition

$$\phi_t = -\frac{1}{2}(\phi_s^2 + \phi_n^2) - gz - \frac{P_a}{\rho}. \tag{2.24}$$

Since the Laplace operator ∇^2 is only spatial it follows from the Laplace equation $\nabla^2\phi_t = 0$ that any time derivative of ϕ also satisfies the Laplace equation, *i.e.*,

$$\nabla^2\phi_t = 0;\ \nabla^2\phi_{tt} = 0;\ \cdots \tag{2.25}$$

ϕ_{tn} on η is then obtained by solving a second Laplace equation $\nabla^2\phi_t = 0$. Formulation of the second Laplace equation is made complete by specifying ϕ_t on the free surface as obtained from (2.24), $\phi_{tn} = 0$ on the impermeable boundary and the appropriate lateral conditions.

As initiated by Dold & Peregrine (1986), the process just described can be extended to set up a sequence of Laplace formulations for ϕ_{tt}, ϕ_{ttt} *etc.* assuming, of course, the lateral conditions can be found in each case. This will enable explicit determination of higher order derivatives to be used in the time updating so that larger time step Δt can be used without loss of necessary accuracy. Benefits of such a scheme are not clear in our case. Formulation of the lateral boundary conditions for the subsequent Laplace equations run into both numerical and physical difficulties. Besides, equations (2.9), (2.19) and (2.20)-(2.23) show that determination of each higher order Lagrangian derivatives involves derivatives of higher order of the variables ϕ, ϕ_t *etc.* along the free surface. The derivatives of a variable along the free surface are obtained by numerical differentiation based on the discrete values of the corresponding variable over a few nodes. It is well known that numerical differentiations become very sensitive to small errors, particularly at the node which is located at the end of the computational interval. For a computational domain with assumed periodicity, end points can be avoided by periodic extension of the free surface. This is not possible in the general case where the lateral conditions are not periodic. Thus, further efforts have not been directed towards extending the free surface updating to an order higher than two.

2.3.3 Computation of the Derivatives Along the Free Surface

In free surface motion ϕ_s is often of larger magnitude than ϕ_n on the free surface. Thus, the tangential[3] derivatives (ϕ_s compared to ϕ_n, ϕ_{ss} compared to ϕ_{ns} *etc.*) have a dominant influence in the evolution of the free surface and an accurate determination of these derivatives is imperative to the sound behavior of the numerical scheme.

Following Grilli *et al.* (1989), computation of the tangential derivatives is based on a set of higher order shape functions, defined in the interval $[-1 \leq \xi \leq 1]$. The derivatives

$$\mathcal{F}_s = \frac{d\mathcal{F}}{d\xi}\frac{d\xi}{ds}, \quad \mathcal{F}_{ss} = \frac{d^2\mathcal{F}}{d\xi^2}(\frac{d\xi}{ds})^2 - \frac{d\mathcal{F}}{d\xi}(\frac{d\xi}{ds})^3\frac{d^2s}{d\xi^2} \tag{2.26}$$

[3] The word 'tangential' is used here to denote the derivatives along the free surface, *not* in the direction of the tangent to the surface.

of a function $\mathcal{F}$ are expressed in terms of the shape functions and its nodal values by using

$$\frac{d\mathcal{F}}{d\xi} = \mathcal{F}_l N_l'(\xi), \tag{2.27}$$

$$\frac{d^2\mathcal{F}}{d\xi^2} = \mathcal{F}_l N_l''(\xi) \tag{2.28}$$

and

$$\frac{ds}{d\xi} = \sqrt{(x'(\xi))^2 + (z'(\xi))^2}, \tag{2.29}$$

$$\frac{d^2s}{d\xi^2} = \frac{x'(\xi)x''(\xi) + z'(\xi)z''(\xi)}{\sqrt{(x'(\xi))^2 + (z'(\xi))^2}} \tag{2.30}$$

where the superscript '$\prime$' denotes differentiation with respect to ξ. Using isoparametric elements $x'(\xi)$, $x''(\xi)$ and similarly, $z'(\xi)$, $z''(\xi)$ are obtained through (2.27) and (2.28) by substituting x or z for $\mathcal{F}$.

The accuracy of the computed derivatives at a node depends on the order of the shape functions (hence, the number of nodes chosen to find a local approximation to the variation of the function) and the location of the node in the interval of the approximation. Higher accuracy is achieved if the node of interest is the middle node of the interval. This principle is followed in the scheme by constructing an element of $2n + 1$ nodes with the node of interest at the middle (later referred to as the 'mid-point rule'). An exception to this principle is necessary while computing the derivatives at each of the first and the last n nodes of the free surface. In a physical domain the free surface intersects with the lateral boundaries and the tangent to the boundary abruptly changes direction across the intersection. As a result, computation of the derivatives at these nodes will incur serious error if mid-point rule is to be used extending over nodes from both the free surface and a lateral boundary. The tangential derivatives at each of these nodes are therefore calculated by considering the node to be at its respective position in an element consisting of $2n + 1$ nodes from the end of the free surface in the computational boundary.

In most of the computations in subsequent chapters derivatives based on a 5-node element (as developed in Grilli *et al.*, 1989) are used. This has been found to be satisfactory for moderately steep waves. For very steep waves (a study of which is undertaken in chapter 7) it becomes crucial to compute the derivatives with higher accuracy. For this

purpose, computation of the derivatives based on 11-node shape functions has been added to the scheme.

2.3.4 Numerical Evolution of the Free Surface

Each node on the free surface is treated as a Lagrangian particle. The truncation error in the present numerical scheme for carrying out the updating is $O(\Delta t)^3$. After the coefficients $d\mathcal{X}/dt$, $d^2\mathcal{X}/dt^2$, $d\mathcal{Z}/dt$ and $d^2\mathcal{Z}/dt^2$ are determined, each node on the free surface is moved to its new position according to (2.5). Since the free surface nodes at the intersections with the lateral boundaries also move, the lateral boundaries too need to change. We shall see in the subsequent chapters how the lateral boundaries are updated in conjunction with the free surface. The important point is that a new position of the computational boundary is defined for the next time level.

Along with the position of the free surface, the potential at each of the free surface nodes is determined for the next time level. This defines the boundary condition on the free surface. Thus, with a procedure for defining the boundary conditions on the lateral sides one has a procedure for studying the temporal evolution.

2.4 Solution of the Laplace Equation

In the present work we solve the integral form of the Laplace equation given by

$$\alpha(\mathbf{x}_0)\phi(\mathbf{x}_0) = \int_\Gamma [\phi_n G(\mathbf{x},\mathbf{x}_0) - \phi G_n(\mathbf{x},\mathbf{x}_0)]d\Gamma \tag{2.31}$$

where Γ is the the boundary of the fluid domain. It is further necessary to solve

$$\alpha(\mathbf{x}_0)\phi_t(\mathbf{x}_0) = \int_\Gamma [\phi_{tn} G(\mathbf{x},\mathbf{x}_0) - \phi_t G_n(\mathbf{x},\mathbf{x}_0)]d\Gamma \tag{2.32}$$

over the same domain Γ at each instant to carry out the free surface updating to second order as discussed earlier. Since (2.32) is identical to (2.31), all formulations derived in connection with (2.31) apply to (2.32) by a substitution of ϕ_t for ϕ. Hence, it is sufficient to limit the discussion to the solution of (2.31). The integration along the boundary Γ is implied to be clockwise with

$$G(\mathbf{x},\mathbf{x}_0) = \frac{1}{2\pi}\ln r. \tag{2.33}$$

Consequently,

$$G_n(\mathbf{x},\mathbf{x}_0) = \frac{1}{2\pi r^2}[(x-x_0)n^x + (z-z_0)n^z] \tag{2.34}$$

where n^x and n^z are the scalar components of the normal $\mathbf{n}$ to Γ at (x,z) and r is the distance $|\mathbf{x}-\mathbf{x}_0|$.

A critical aspect of a computational domain in the physical space is that the boundary Γ is not smooth, the normal vector being discontinuous at the intersection of two sides (*e.g.*, the free surface and a lateral side or a lateral side and the bottom). As a result, the normal flux is discontinuous too. A proper numerical procedure must allow for the multiplicity of the normal vector and the normal flux at the intersection. One technique through which this can be done is by using 'double nodes' at the corner (see Banerjee & Butterfield, 1981 for details). The 'double nodes' refer to two nodes having the same geometric coordinates (that of the corner point) but each one of which belongs to a different side. This technique has been used by Grilli *et al.* (1989) for the free surface problems and has been found to be quite successful. The same procedure is adopted here too. Thus, the boundary Γ is considered to be consisting of smooth sides between the corners instead of being treated as one smooth contour.

Discretization is the first step in the solution of (2.31). First, the integral on the right hand side of (2.31) is expressed as a sum of the integrals over small segments Γ_I's which comprise the boundary Γ:

$$\int_\Gamma [\phi_n G(\mathbf{x},\mathbf{x}_0) - \phi G_n(\mathbf{x},\mathbf{x}_0)]d\Gamma = \sum \int_{\Gamma_I} [\phi_n G(\mathbf{x},\mathbf{x}_0) - \phi G_n(\mathbf{x},\mathbf{x}_0)]d\Gamma. \tag{2.35}$$

Following the preceding comment on the discontinuity at a corner, we require that the boundary Γ be divided to Γ_I's such that no Γ_I contain a corner in its open interval. To proceed further, it is now necessary to approximate the variation of ϕ, ϕ_n and the geometry over each Γ_I in terms of the discrete nodal values. In the following sections we describe how higher order numerical approximation to the local variations of these quantities are made and highly accurate numerical integration is achieved.

2.4.1 Higher Order Discretization: Finite Element Approach

Higher order discretization based on the finite element approach is followed in Grilli *et al.* (1989). In this procedure, each interval Γ_I consisting of jn (two or more) nodes (fig. 2.3) is isoparametrically mapped to $[-1 \leq \mu \leq 1]$. One thus has

$$\int_{\Gamma_I} [\phi_n G(\mathbf{x}, \mathbf{x}_0) - \phi G_n(\mathbf{x}, \mathbf{x}_0)] d\Gamma = \int_{-1}^{1} [\phi_n G(\mathbf{x}, \mathbf{x}_0) - \phi G_n(\mathbf{x}, \mathbf{x}_0)] J(\mu) d\mu. \tag{2.36}$$

$J(\mu)$ in (2.36) is the Jacobian of the transformation $ds/d\mu$. By using (2.3) one has

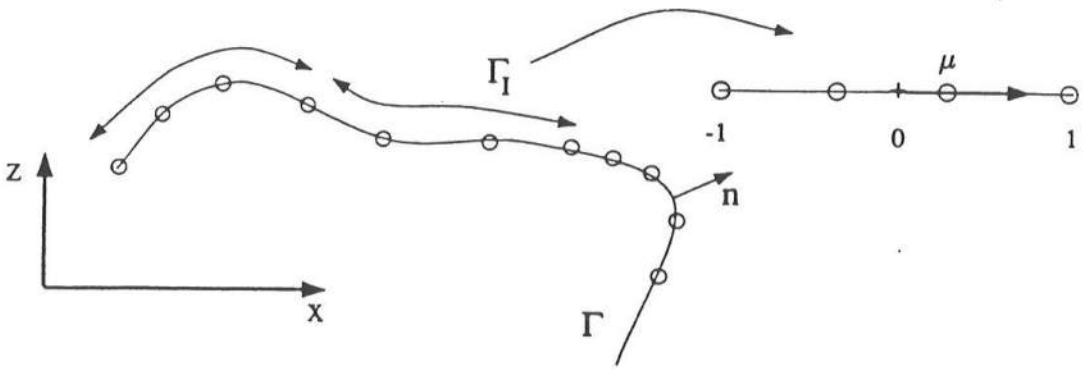

Figure 2.3: Finite element approach

$$\int_{-1}^{1} [\phi_n G(\mathbf{x}, \mathbf{x}_0) - \phi G_n(\mathbf{x}, \mathbf{x}_0)] J(\mu) d\mu = \phi_{n_{l(j)}} \int_{-1}^{1} N_l(\mu) G(\mathbf{x}(\mu), \mathbf{x}_0) J(\mu) d\mu$$
$$- \phi_{l(j)} \int_{-1}^{1} N_l(\mu) G_n(\mathbf{x}(\mu), \mathbf{x}_0) J(\mu) d\mu. \tag{2.37}$$

The geometrical parameters $[J(\mu),\ n^x,\ n^z]$

$$J(\mu) = \sqrt{\left(\frac{dx}{d\mu}\right)^2 + \left(\frac{dz}{d\mu}\right)^2}, \tag{2.38}$$

$$n^x = -\frac{dz}{ds} = -\frac{dz}{d\mu}\frac{d\mu}{ds}, \tag{2.39}$$

$$n^z = \frac{dx}{ds} = \frac{dx}{d\mu}\frac{d\mu}{ds} \tag{2.40}$$

are obtained by using (2.4) to evaluate $dx/d\mu$ and $dz/d\mu$ at a point μ. The integrands on the right side of (2.37) now involve completely known functions and the evaluation of the integrals can be carried out numerically. The integration procedure and the eventual solution of (2.31) are discussed in later sections.

If the interval Γ_I contains only two nodes, the flow quantities and the geometry are approximated by linear variation between the two nodes. Higher order approximation to the variation is achieved when each subinterval Γ_I (or an element) consists of more nodes. The higher order description leads to higher accuracy than using linear elements with the same nodal spacing. However, it has been found during applications to nonlinear free surface motions that the use of the higher order element leads to quick instabilities. Thus, the higher order description based on the 'Finite Element' approach can not be used to represent the free surface if the wave motion needs to be studied over a long time or the wave steepness is high.

A rigorous analysis of the causes of the instabilities has not been undertaken here. A consequence of the discretization based on the finite element approach is that the calculated normal vector (n^x, n^z) may be discontinuous near the intersection of two elements. With higher order elements, the discontinuities are likely to be more sensitive to small errors. It is believed that the instabilities on the free surface using the discretization based on finite element approach are related to this factor.

2.4.2 Higher Order Discretization: Quasi-Spline Method

To ensure continuity of the calculated normal vector (n^x, n^z) across the intersection of two elements, cubic spline approximation of the geometry has been used by Grilli & Svendsen (1989) and Svendsen & Grilli (1990). The formulations for cubic spline description of a curve in Cartesian coordinates can be found in standard numerical books (*e.g.*, Press *et al.*, 1986). The normally followed description in Cartesian coordinates is not valid to describe the free surface motion which may become multiple-valued during overturning. A parameter having monotonic behavior along the free surface is s, the length along the contour or equivalently an index τ equal to the node number j at the location of the node. If x and z are expressed in terms of the parameter τ, cubic spline approximation to the parametric description is possible using the standard procedure. Using $\mathcal{F}$ to denote either x or z, the cubic spline variation between two consecutive nodes is given by

$$\mathcal{F}(\tau) = A\mathcal{F}_j + B\mathcal{F}_{j+1} + C\mathcal{F}''_j + D\mathcal{F}''_{j+1} \tag{2.41}$$

where

$$A = \frac{\tau_{j+1} - \tau}{\tau_{j+1} - \tau_j}, \tag{2.42}$$

$$B = \frac{\tau - \tau_j}{\tau_{j+1} - \tau_j}, \tag{2.43}$$

$$C = \frac{1}{6}(A^3 - A)(\tau_{j+1} - \tau_j)^2, \tag{2.44}$$

$$D = \frac{1}{6}(B^3 - B)(\tau_{j+1} - \tau_j)^2 \tag{2.45}$$

and the superscript '$\prime$' denotes differentiation with respect to τ. Thus far, $\mathcal{F}''_j$ and $\mathcal{F}''_{j+1}$ are unknowns in (2.41). The necessary equations to determine the second order derivatives $\mathcal{F}''$ are obtained by requiring that the first order derivative $\mathcal{F}'_j$ at a node j calculated from (2.41) based on the interval between j and $j+1$ is same as that based on the interval between $j-1$ and j. These equations are however not defined at the two nodes at each end of a side. To complete the specifications, the first or the second order derivative at each end node needs to be specified. Only in a few cases, these conditions can be obtained from physical considerations; for example, the the free surface slope should be zero at a vertical reflecting wall. In other cases, the first derivatives at each end node is specified from a polynomial interpolation of third order based over four consecutive nodes at the end.

The spline approximation for the geometrical variation yields smooth variation of the calculated normal vector across the interface of two elements. However, this procedure can not be used to represent the variation of the unknown function ϕ_n on the free surface. Thus, while the geometry is approximated by a cubic spline, variation of the function is assumed to be linearly varying with τ between two consecutive nodes. Hence, the name 'quasi-spline' is used for this type of discretization.

If 'quasi-spline' discretization is adopted the subinterval Γ_I spans the length between two consecutive nodes $[\tau_j \leq \tau \leq \tau_{j+1}]$. For the numerical integration it is convenient to express this over $[-1, 1]$. This is done through a linear mapping of τ to μ given by

$$\tau(\mu) = \tau_j + (\tau_{j+1} - \tau_j)\frac{1+\mu}{2}. \tag{2.46}$$

Variation of the functions ϕ and ϕ_n over this interval are then expressed in terms of two-node shape functions. The Jacobian

$$\frac{ds}{d\mu} = \sqrt{\left(\frac{dx}{d\tau}\frac{d\tau}{d\mu}\right)^2 + \left(\frac{dz}{d\tau}\frac{d\tau}{d\mu}\right)^2} \tag{2.47}$$

of the transformation from s to μ is obtained from (2.41) and (2.46).

2.4.3 Higher Order Discretization: Mid-Interval Approximation Method

Though the calculated normal vector is continuous at the intersection of two elements in the spline description, the procedure is very restricted in that it applies only to the geometry and extension to higher order is difficult. Besides, it involves additional computation to determine the derivatives $d^2x/d\tau^2$ and $d^2z/d\tau^2$ at each node on the free surface. On the other hand, the higher order discretization based on the finite element approach has been found to be unsatisfactory for the free surface. This has led to developing a new procedure described in the following as 'Mid-Interval Approximation Method'.

Independent of the order of discretization used in this procedure Γ_I is always chosen to be the interval between two consecutive nodes. Thus,

$$\int_\Gamma [\phi_n G(x,x_0) - \phi G_n(x,x_0)]d\Gamma = \sum_{j=1}^{N-1} \int_{s_j}^{s_{j+1}} [\phi_n G(x,x_0) - \phi G_n(x,x_0)]d\Gamma \quad . \tag{2.48}$$

where N represents the total number of nodes and s_j represents the length along the contour at the node j measured from a reference point on the boundary. To approximate

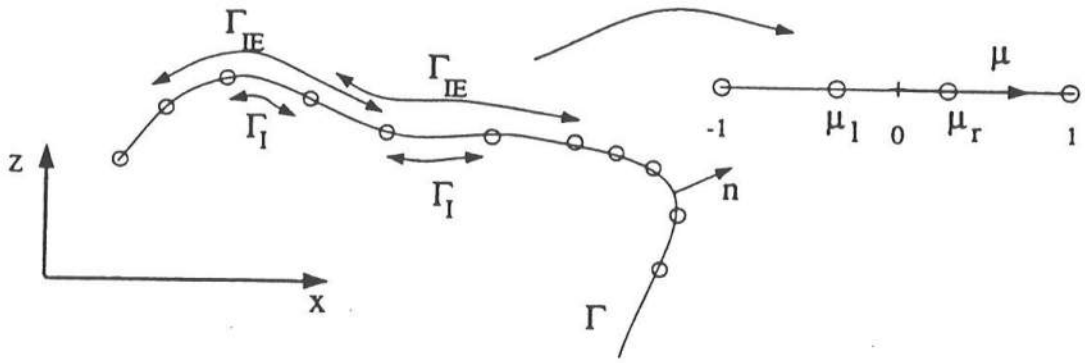

Figure 2.4: Mid-Interval element approach

the variation of ϕ and ϕ_n between s_j and s_{j+1}, we now construct an element of an even

number of $2n$ nodes over the interval Γ_{IE} (fig. 2.4) with j and $j+1$ being in the middle. Thus, with each new interval Γ_I a new element Γ_{IE} is constructed. An exception to this rule is necessary while considering an interval Γ_I (between two consecutive nodes) which forms one of the $(n-1)$ intervals on either end of a side. For these intervals, Γ_{IE} consists of the extreme $2n$ nodes at the respective end of the side. Using (2.3), the integrals in (2.48) can be expressed as

$$\int_{s_j}^{s_{j+1}} \phi G_n(\mathbf{x},\mathbf{x}_0)d\Gamma - \int_{s_j}^{s_{j+1}} \phi_n G(\mathbf{x},\mathbf{x}_0)d\Gamma = \phi_{l(j)} \int_{\mu_l}^{\mu_r} N_l(\mu) G_n(\mathbf{x}(\mu),\mathbf{x}_0) J(\mu) d\mu$$
$$-\phi_{n_{l(j)}} \int_{\mu_l}^{\mu_r} N_l(\mu) G(\mathbf{x}(\mu),\mathbf{x}_0) J(\mu) d\mu. \quad (2.49)$$

μ_l and μ_r denote the points in $[-1 \le \mu \le 1]$ to which s_j and s_{j+1} are respectively mapped and are given by

$$\mu_l = -1 + \frac{2(IL-1)}{2n-1}, \quad (2.50)$$

$$\mu_r = \mu_l + \frac{2}{2n-1} \quad (2.51)$$

where IL denotes the sequential number of Γ_I of interest in the element Γ_{IE} counted from the left. For an interval Γ_I not belonging to the $(n-1)$ end intervals, IL assumes the value n and μ_l and μ_r are the two middle nodes in Γ_{IE}. In this case, one simply has

$$\mu_l = -\frac{1}{2n-1}; \quad \mu_r = \frac{1}{2n-1}. \quad (2.52)$$

As before, it is convenient to express the integrals in (2.49) over the interval $[-1,1]$ which is done through a linear mapping of μ to ξ defined by

$$\mu(\xi) = \mu_l + (\mu_r - \mu_l)\frac{1+\xi}{2}. \quad (2.53)$$

The Jacobian

$$\frac{ds}{d\xi} = \frac{d\mu}{d\xi}\sqrt{\left(\frac{dx}{d\mu}\right)^2 + \left(\frac{dz}{d\mu}\right)^2} \quad (2.54)$$

of the transformation from s to ξ is obtained from (2.53) and (2.4) defining the mapping of x and z to μ.

The "mid-interval" approximation results in a stable scheme with the advantage that extension to higher order is almost automatic only by defining the higher-order shape

functions in the code. Numerical examples showing the difference between the quasi-spline discretization and this procedure are cited in connection with the propagation of steep solitary waves in chapter 6.

2.4.4 Evaluation of the Integrals

In all the three types of discretizations just described, one gets

$$\int_{\Gamma_I} [\phi_n G(\mathbf{x}, \mathbf{x}_0) - \phi G_n(\mathbf{x}, \mathbf{x}_0)]\, d\Gamma = \phi_{n_{l(j)}} K^q_{i,l(j)} - \phi_{l(j)} K^u_{i,l(j)} \tag{2.55}$$

where

$$K^q_{i,l(j)} = \int_{-1}^{1} N_l[\mu(\xi)] G[\mathbf{x}(\xi), \mathbf{x}_0] J(\xi) d\xi, \tag{2.56}$$

$$K^u_{i,l(j)} = \int_{-1}^{1} N_l[\mu(\xi)] G_n[\mathbf{x}(\xi), \mathbf{x}_0] J(\xi) d\xi. \tag{2.57}$$

$N_l(\mu(\xi))$ is a shape function defined over $[-1 \leq \mu \leq 1]$. In $K^q_{i,l(j)}$ and $K^u_{i,l(j)}$, 'i' refers to the index of the node at $\mathbf{x}_0$ and 'j' refers to a node in the element Γ_{IE} on the boundary Γ whereas '$l(j)$' denotes the local index of the node 'j' in the mapped space. It follows from the previous descriptions that $\mu = \xi$ if discretization based on 'finite element' or 'quasi-spline' approach is adopted. The relation between μ and ξ is given by (2.53) if 'mid-interval approximation' method is used. The Jacobian $J(\xi)$ is obtained from the mapping used for the geometry in each respective case.

The first numerical approximation in the solution of (2.31) is introduced through the assumptions of the variations of ϕ, ϕ_n and the geometry over the interval Γ_I. The second approximation now comes in through the numerical evaluation of the integrals (2.56) and (2.57). Thus, an accurate procedure of integration is one of the critical aspects of the scheme. How this can be achieved has been shown earlier in Grilli *et al.* (1989) in the context of the discretization based on the 'finite element' approach. Here a unified procedure is presented for all the three different discretizations.

The variations of the integrands in (2.56) and (2.57) are determined by the order of the shape functions used, the Jacobian, $G(\mathbf{x}, \mathbf{x}_0)$ and $G_n(\mathbf{x}, \mathbf{x}_0)$. If $\mathbf{x}_0$ belongs to the interval Γ_I over which the integration is performed $G(\mathbf{x}, \mathbf{x}_0)$, given by (2.33), develops

a logarithmic singularity and the numerical calculation of $G_n(\mathbf{x},\mathbf{x}_0)$ through (2.34) may lead to unacceptable errors. Thus, special procedures are necessary if $\mathbf{x}_0$ belongs to the Γ_I of interest.

For $\mathbf{x}_0 \notin \Gamma_I$, the integrands are regular. However, the order of the variation may be quite high due to the variation of the function $G(\mathbf{x},\mathbf{x}_0)$ or $G_n(\mathbf{x},\mathbf{x}_0)$. For this reason, Gauss-quadrature (see Atkinson, 1976; Abramowitz & Stegun, 1972) is used to evaluate the coefficients $K^q_{i,l(j)}$ and $K^u_{i,l(j)}$ accurately, *i.e.*,

$$K^q_{i,l(j)} = \sum_{ip=1}^{np} W_{ip} N_l[\mu(\xi_{ip})] G[\mathbf{x}(\xi_{ip}),\mathbf{x}_0] J(\xi_{ip}), \tag{2.58}$$

$$K^u_{i,l(j)} = \sum_{ip=1}^{np} W_{ip} N_l[\mu(\xi_{ip})] G_n[\mathbf{x}(\xi_{ip}),\mathbf{x}_0] J(\xi_{ip}) \tag{2.59}$$

where ξ_{ip} denotes an integration point and W_{ip} the weight at that point. np, the number of integration points, is chosen to be 10 in the computations cited in the present work. This rather high value for np virtually eliminates any error in the numerical integrations except in some special circumstances. These are discussed in the context of the computation of the interior field later in the present chapter and the evaluation of the coefficients near a corner in chapter 3.

Evaluation of $K^q_{i,l(j)}$ for $\mathbf{x}_0 \in \Gamma_I$

The integrand in this case has a singularity of the logarithmic type. A logarithmic singularity is integrable, but numerical integration using regular Gauss-quadrature weights is less accurate. Thus, a separate procedure, similar to that of Longuet-Higgins (1976), is first used to split the integrand to two parts, a regular integrand and a logarithmic part of the type $f(\xi)ln(\xi)$. This is briefly described as follows. Let ξ_0 be the point to which $\mathbf{x}_0$ is mapped in the interval $[-1 \le \xi \le 1]$. One then has

$$\begin{aligned} K^q_{i,l(j)} &= \frac{1}{2\pi}\int_{-1}^{1} N_l[\mu(\xi)]\ln(r)J(\xi)d\xi \\ &= \frac{1}{2\pi}\left[\int_{-1}^{\xi_0} N_l[\mu(\xi)]\ln(r)J(\xi)d\xi + \int_{\xi_0}^{1} N_l[\mu(\xi)]\ln(r)J(\xi)d\xi\right]. \end{aligned} \tag{2.60}$$

and further,

$$\int_{-1}^{\xi_0} N_l[\mu(\xi)]\ln(r)J(\xi)d\xi = \int_{-1}^{\xi_0} N_l[\mu(\xi)]\ln\left(\frac{r}{\xi_0-\xi}\right)J(\xi)d\xi + \int_{-1}^{\xi_0} N_l[\mu(\xi)]\ln(\xi_0-\xi)J(\xi)d\xi, \tag{2.61}$$

$$\int_{\xi_0}^{1} N_l[\mu(\xi)]\ln(r)J(\xi)d\xi = \int_{\xi_0}^{1} N_l[\mu(\xi)]\ln(\frac{r}{\xi-\xi_0})J(\xi)d\xi + \int_{\xi_0}^{1} N_l[\mu(\xi)]\ln(\xi-\xi_0)J(\xi)d\xi. \tag{2.62}$$

Combining (2.61) and (2.62) yields

$$\int_{-1}^{1} N_l[\mu(\xi)]\ln(r)J(\xi)d\xi = \int_{-1}^{1} N_l[\mu(\xi)]\ln\left(\frac{r}{|\xi-\xi_0|}\right)J(\xi)d\xi + \int_{-1}^{\xi_0} N_l[\mu(\xi)]\ln(\xi_0-\xi)J(\xi)d\xi + \int_{\xi_0}^{1} N_l[\mu(\xi)]\ln(\xi-\xi_0)J(\xi)d\xi. \tag{2.63}$$

That the integrand containing $\ln(r/|\xi-\xi_0|)$ is no longer singular can be proved by a simple analysis. The Taylor's expansion around $\mathbf{x}_0$ gives

$$x = x_0 + \Delta s\frac{dx}{ds}(\mathbf{x}_0) + \cdots \tag{2.64}$$

$$z = z_0 + \Delta s\frac{dz}{ds}(\mathbf{z}_0) + \cdots \tag{2.65}$$

Hence, for $\Delta s \to 0$ corresponding to $(\xi-\xi_0) \to 0$ one has

$$r = \sqrt{(x-x_0)^2+(z-z_0)^2} \approx \Delta s\sqrt{\left(\frac{dx}{ds}\right)^2+\left(\frac{dz}{ds}\right)^2} = \Delta s. \tag{2.66}$$

Using (2.66) one then obtains

$$\lim_{|\xi-\xi_0|\to 0}\ln\left(\frac{r}{|\xi-\xi_0|}\right) = \lim_{\Delta\xi\to 0}\ln(\Delta s/\Delta\xi) = \ln[J(\xi)]. \tag{2.67}$$

$J(\xi)$, the Jacobian of the transformation is always positive and sufficiently large unless the actual length of the element is too small. Hence, the first integral on the right side of (2.63) can be accurately evaluated by using the standard Gauss-quadrature rules. In the other two integrals, each integrand is first converted to the form $f(\psi)\ln(\psi)$ over the interval [0,1] through a linear transformation of ξ to ψ. Accurate numerical integration of an integrand of this form is achieved by using Berthod-Zabrowski quadrature (Stroud & Secrest, 1966).

Evaluation of $K^u_{i,l(j)}$ for $\mathbf{x}_0 \in \Gamma_I$

For $\mathbf{x}_0 \in \Gamma_I$, both the denominator and the numerator of $G_n(\mathbf{x},\mathbf{x}_0)$ go to zero as $\mathbf{x} \to \mathbf{x}_0$. The behavior of the integrand may be analyzed the following way. From (2.34) we have

$$G_n(\mathbf{x},\mathbf{x}_0)J(\xi) = \frac{1}{2\pi}\frac{(x-x_0)n^x + (z-z_0)n^z}{r^2}J(\xi). \tag{2.68}$$

Using the relations

$$n^x J(\xi) = -\frac{dz}{d\xi}; \quad n^z J(\xi) = \frac{dx}{d\xi} \tag{2.69}$$

(2.68) can be expressed as

$$G_n(\mathbf{x},\mathbf{x}_0)J(\xi) = \frac{1}{2\pi}\frac{-(x-x_0)\frac{dz}{d\xi} + (z-z_0)\frac{dx}{d\xi}}{r^2}. \tag{2.70}$$

It follows now that

$$G_n(\mathbf{x},\mathbf{x}_0)J(\xi) = -\frac{1}{2\pi}\frac{dv}{d\xi} \tag{2.71}$$

where the variable v is defined by the expression

$$v = \tan^{-1}\left[\frac{z-z_0}{x-x_0}\right]. \tag{2.72}$$

v, defined by (2.72) becomes singular if the interval Γ_I is aligned with the z-axis. To avoid this problem, this definition is used only when Γ_I is inclined more to the x-axis and we use the definition

$$v = -\tan^{-1}\left[\frac{x-x_0}{z-z_0}\right]. \tag{2.73}$$

when Γ_I is inclined more to the z-axis. Expression (2.71) is satisfied for both the definitions of v. Substituting (2.71) in (2.57) we have

$$\begin{aligned}\int_{-1}^{1} N_l[\mu(\xi)]G_n(\mathbf{x},\mathbf{x}_0)J(\xi)d\Gamma &= -\frac{1}{2\pi}\int_{-1}^{1} N_l(\mu(\xi))\frac{dv}{d\xi}d\xi \\ &= -\frac{1}{2\pi}\left[N_l[\mu(\xi)]v|_{-1}^{1} - \int_{-1}^{1} N_l'[\mu(\xi)]v d\xi\right]. \end{aligned} \tag{2.74}$$

The first part on the right hand side is a definite integral and is simple to calculate. Regular Gauss-quadrature can be used to evaluate the second part in (2.74). The angle v at the integration points is calculated from the respective definition (2.72) or (2.73). If the absolute value of the denominator in the definition of v is close to zero ($\leq \epsilon$; in the

numerical scheme we use $\epsilon = 10^-6$) at an integration point next to ξ_0, v is defined by the L'Hospital's rule, *i.e.*,

$$v = \tan^{-1}\left[\frac{dz}{d\xi}\Big/\frac{dx}{d\xi}\right] \tag{2.75}$$

corresponding to (2.72) or by

$$v = \tan^{-1}\left[\frac{dx}{d\xi}\Big/\frac{dz}{d\xi}\right] \tag{2.76}$$

corresponding to (2.73).

2.4.5 Discrete Form of the Integral Equation

Expression (2.55) relates the integral involving the continuous variation of ϕ, ϕ_n, G and G_n over the interval Γ_I to a linear algebraic form in terms of a few discrete nodal values of $\phi_{l(j)}$ and $\phi_{n_{l(j)}}$. $l(j)$, as defined earlier, is the local index of the node j in the mapped element. By carrying out the procedure over each interval of the entire boundary and grouping together the coefficients of each node j, the discrete form

$$\alpha_i\phi_i = K^q_{i,j}\phi_{n_j} - K^u_{i,j}\phi_j; \quad i,j = 1,2,3,\cdots,N \tag{2.77}$$

of the integral equation (2.31) is obtained. In (2.77), i denotes the index of the node at $\mathbf{x}_0$ and N denotes the total number of nodes used to discretize the boundary. Each $K^q_{i,j}$ is a sum of the $K^q_{i,l(j)}$'s having the same i and j from all the Γ_I's and each $K^u_{i,j}$ is a sum of the $K^u_{i,l(j)}$'s. Equation (2.77) represents a system of N linear equations which can be solved using a suitable matrix method if the system is well-posed.

2.4.6 Modification of the Discrete Equations for the Corner Nodes

It has been earlier mentioned that the technique of the 'double-nodes' is used here to properly represent the multi-valuedness of the normal vector to the boundary at an intersection of two sides. Each of the double-nodes has the same geometrical position as that of the corner (or the intersection) point. However, each one is considered to belong to a different side. The result is that the tangent to the boundary Γ at a corner node is the tangent to the side (as defined earlier, a side is a smooth contour between two consecutive corners on the boundary) to which it belongs, with similar implications for the normal vector $\mathbf{n}$ and the normal flux ϕ_n.

Let $I1$ and $I2$ denote the indices of the two nodes at an intersection. Due to their identical geometrical positions one has

$$K^u_{I1,j} = K^u_{I2,j}, \quad K^q_{I1,j} = K^q_{I2,j}, \quad \alpha_{I1} = \alpha_{I2} \tag{2.78}$$

in (2.77) following the definitions of the coefficients α_i, $K^u_{i,j}$ and $K^q_{i,j}$. Implications of (2.78) on the determinant of the system (2.77) have been discussed in Grilli et al. (1990) and Grilli & Svendsen (1990). The nature of the problem and the remedy depends on the types of the boundary conditions specified on the intersecting sides.

Intersection of Dirichlet-Dirichlet sides

If a Dirichlet type of condition is specified on each of the intersecting sides, the unknown to be solved at the node $I1$ or $I2$ is the normal flux. It is then seen that the coefficients of the unknown variables in the system (2.77) corresponding to the two rows $I1$ and $I2$ are identical due to (2.78). The redundancy in the system can be removed by replacing at least one of the equations corresponding to the rows $I1$ and $I2$ in (2.77) by an appropriate independent equation. From the uniqueness of the velocity (flux) vector at the corner one has the relation

$$\phi_{s_{I1}} \cos\beta_{I1} - \phi_{n_{I1}} \sin\beta_{I1} = \phi_{s_{I2}} \cos\beta_{I2} - \phi_{n_{I2}} \sin\beta_{I2} \tag{2.79}$$

by requiring that the velocity in the x-direction defined at the node $I1$ is same as that defined at the node $I2$ and similarly

$$\phi_{s_{I1}} \sin\beta_{I1} + \phi_{n_{I1}} \cos\beta_{I1} = \phi_{s_{I2}} \sin\beta_{I2} + \phi_{n_{I2}} \cos\beta_{I2} \tag{2.80}$$

by requiring that the velocity in the z-direction at the node $I1$ is same as that at the node $I2$. Since $\phi_{s_{I1}}$ and $\phi_{s_{I2}}$ can be expressed in terms of the nodal values ϕ_j's which are known on sides with Dirichlet type of conditions, $\phi_{n_{I1}}$ and $\phi_{n_{I2}}$ are the only unknowns in (2.79) and (2.80). Thus, (2.79) and (2.80) can be reorganized with the unknowns on the left hand sides respectively in the forms

$$\phi_{n_{I1}} \sin\beta_{I1} - \phi_{n_{I2}} \sin\beta_{I2} = \phi_{s_{I1}} \cos\beta_{I1} - \phi_{s_{I2}} \cos\beta_{I2}, \tag{2.81}$$

$$\phi_{n_{I1}} \cos\beta_{I1} - \phi_{n_{I2}} \cos\beta_{I2} = -\phi_{s_{I1}} \sin\beta_{I1} + \phi_{s_{I2}} \sin\beta_{I2}. \tag{2.82}$$

Either of (2.81) or (2.82) can be used to replace the row $I1$ or $I2$ of (2.77). The choice depends on the coefficient of the diagonal term: we choose (2.81) instead of (2.82) for the row $I1$ if $\sin\beta_{I1}$ is larger in magnitude than $\cos\beta_{I1}$ and *vice-versa*.

Intersection of Neumann-Dirichlet or Neumann-Neumann sides

If Neumann condition is specified on at least one of the sides, the problem of redundancy observed earlier in case of two intersecting Dirichlet sides changes. Let $I1$ denote the node which belongs to the side on which the specified condition is of the Neumann type. Hence, ϕ_{I1} is the unknown to be solved at this node. The coefficient of ϕ_{I1} in row $I1$ of (2.77) is $-\left(K^u_{I1,I1}+\alpha_{I1}\right)$ and in row $I2$ is $-K^u_{I2,I1}$. Thus, though one has $K^u_{I1,I1} = K^u_{I2,I1}$ according to (2.78) the coefficients of the unknown ϕ_{I1} in the two rows $I1$ and $I2$ are different. Hence, there is strictly no degeneracy in (2.77). However, the identities expressed by (2.78) lead to bad conditioning of the coefficient matrix. It has been found that the conditioning of the matrix is improved if the $I1$th row is replaced by

$$\phi_{I1} - \phi_{I2} = 0. \tag{2.83}$$

Expression (2.83) is a statement of the continuity of the potential at a corner and can, in fact, be also obtained by subtracting the $I2$th row from the $I1$th row of (2.77).

2.4.7 Solution of the Linear Algebraic System

Equation (2.77) is a system of N linear equations corresponding to the N nodes on the boundary. The linear system involves $2N$ variables of ϕ and ϕ_n, out of which N are specified as the boundary conditions. Writing (2.77) in the matrix form, one has

$$A\mathcal{F} = B \tag{2.84}$$

where

$$\begin{aligned} A_{i,j} &= -\left(K^u_{i,j}+\delta_{ij}\alpha_j\right) \qquad \text{if } \phi_{n_j} \text{ is specified;} \\ &= K^q_{i,j} \qquad\qquad \text{if } \phi_j \text{ is specified} \end{aligned} \tag{2.85}$$

with δ_{ij} being the Kronecker-delta function and

$$\mathcal{F}_i = \phi_i \quad \text{if } \phi_{n_i} \text{ is specified;} \tag{2.86}$$

$$= \phi_{n_i} \quad \text{if } \phi_i \text{ is specified.} \tag{2.87}$$

Before solving for $\mathcal{F}$'s in (2.84), $A_{i,j}$'s and B_i's are appropriately modified at rows corresponding to the corner nodes as discussed in the previous section.

We note that the coefficients of A, given by (2.85) or the modifications, depend only on the geometry of the domain and the type of the specified boundary conditions. The coefficient matrix will thus be identical for the two systems, given respectively by (2.31) and (2.32), provided the boundary condition is of the same type at every node in both. Dirichlet condition on the free surface and Neumann condition on the bottom are specified for both these systems. As will be seen later, the specified conditions on each lateral side can also be of the identical type in many applications. Keeping this in mind, the matrix is solved through LU decomposition (see Press et al., 1986) so that once the decomposition of the coefficient matrix is done, the linear system can be solved for a different right hand side [as that of the second system (2.32)] for a fraction of the CPU used for the first.

2.5 Computation of the Internal Field

Flow quantities at an interior point $\mathbf{x}_0$ are related to the boundary data through the integral equation

$$\alpha(\mathbf{x}_0)\phi(\mathbf{x}_0) = \int_\Gamma [\phi_n(\mathbf{x})G(\mathbf{x},\mathbf{x}_0) - \phi(\mathbf{x})G_n(\mathbf{x},\mathbf{x}_0)]d\Gamma \tag{2.88}$$

where $\alpha(\mathbf{x}_0) = 1$. Explicit equations for the velocity (ϕ_x, ϕ_z) can be obtained by differentiating (2.88) with respect to x_0. These are

$$\phi_x(\mathbf{x}_0) = \int_\Gamma \left[\phi_n \frac{\partial}{\partial x_0} G(\mathbf{x},\mathbf{x}_0) - \phi \frac{\partial}{\partial x_0} G_n(\mathbf{x},\mathbf{x}_0)\right] d\Gamma, \tag{2.89}$$

$$\phi_z(\mathbf{x}_0) = \int_\Gamma \left[\phi_n \frac{\partial}{\partial z_0} G(\mathbf{x},\mathbf{x}_0) - \phi \frac{\partial}{\partial z_0} G_n(\mathbf{x},\mathbf{x}_0)\right] d\Gamma \tag{2.90}$$

where

$$G(\mathbf{x},\mathbf{x}_0) = \frac{1}{2\pi} \ln r, \tag{2.91}$$

$$G_n(\mathbf{x},\mathbf{x}_0) = \frac{1}{2\pi}\left[\frac{x-x_0}{r^2}n^x + \frac{z-z_0}{r^2}n^z\right], \tag{2.92}$$

$$\frac{\partial G(\mathbf{x},\mathbf{x}_0)}{\partial x_0} = -\frac{1}{2\pi}\frac{x-x_0}{r^2}, \tag{2.93}$$

$$\frac{\partial G(\mathbf{x},\mathbf{x}_0)}{\partial z_0} = -\frac{1}{2\pi}\frac{z-z_0}{r^2}, \tag{2.94}$$

$$\frac{\partial G_n(\mathbf{x},\mathbf{x}_0)}{\partial x_0} = \frac{1}{2\pi}\left[-\frac{n^x}{r^2} + \frac{2(x-x_0)}{r^4}\{(x-x_0)n^x + (z-z_0)n^z\}\right], \tag{2.95}$$

$$\frac{\partial G_n(\mathbf{x},\mathbf{x}_0)}{\partial z_0} = \frac{1}{2\pi}\left[-\frac{n^z}{r^2} + \frac{2(z-z_0)}{r^4}\{(x-x_0)n^x + (z-z_0)n^z\}\right]. \tag{2.96}$$

Since both the potential and the normal flux are known on the boundary after the solution of the Laplace equation, the right hand sides of the equations (2.88) through (2.90) do not involve any unknowns and the internal field can be computed through a straightforward evaluation of the integrals using the same discretization of the boundary as used for the solution of (2.31). In analogy to (2.31) the integral along the boundary Γ is then expressed as

$$\int_\Gamma [*]d\Gamma = \sum \int_{\Gamma_I} [*]d\Gamma \tag{2.97}$$

where '[*]' refers to the integrand in (2.88), (2.89) or (2.90). For an interior point $\mathbf{x}_0$, these integrals are regular and Gauss-quadrature rule is used over a transformed map of Γ_I as during the solution of the Laplace equation. ϕ_t, ϕ_{tx} and ϕ_{tz} at an interior point $\mathbf{x}_0$ are also related to the boundary value of ϕ_t and ϕ_{tn} by a set of integral expressions obtained by substituting ϕ_t for ϕ in each of (2.88)-(2.90). With ϕ_t and the velocity (ϕ_x, ϕ_z) known at an interior point, the pressure at that point is determined by using the Bernoulli equation

$$\frac{P}{\rho} = -\phi_t - \frac{1}{2}(\phi_x^2 + \phi_z^2) - gz. \tag{2.98}$$

This procedure has been used by Grilli and Svendsen (1989) to obtain the velocity field during the runup of a solitary wave on a slope.

However, the computation of the velocity field through a straightforward evaluation of (2.97) becomes inaccurate if the point $\mathbf{x}_0$ approaches the boundary. We consider a simple example of a uniform steady flow of normalized velocity 0.9 in a rectangular domain. The normalized length and height of the domain are 22.5 and 1.0 respectively. Nodes are placed uniformly over the boundary with a spacing of 0.25. Linear elements are used and each

integration interval is thus the space between two consecutive nodes. Table (2.1) shows ϕ, ϕ_x and ϕ_z computed by using a 10-point Gauss integration at three internal points which are located close to the vertical boundary at $x = 22.5$. We note that the computed

Table 2.1: Computed ϕ, ϕ_x and ϕ_z at three interior points. The exact values are $\phi(x_0, z_0) = 20.2050$, $\phi_x(x_0, z_0) = 0.9$ and $\phi_z(x_0, z_0) = 0.0$ at all the three points.

x_0	z_0	ϕ	ϕ_x	ϕ_z
22.45	-0.1	20.228665080236	3.921784630152	-0.307378390224
22.45	-0.3	20.212650463433	1.843205927486	-0.637270784262
22.45	-0.7	20.212650463433	1.843205927487	-0.637270784262

values of ϕ_x and ϕ_z are completely wrong though the error in the computed ϕ is smaller. It is therefore necessary to develop a special procedure to enable accurate computation of the velocity field at points close to the boundary.

2.5.1 Computation of the Internal Field at Points Close to the Boundary

In the expressions (2.88)-(2.90) the variations of ϕ and ϕ_n over the boundary remain independent of the position of the internal point $\mathbf{x}_0$ with respect to the boundary. However, the variations of G, G_n and their derivatives with respect to (x_0, z_0) depend directly on the position of the point $\mathbf{x}_0$. As $\mathbf{x}_0$ approaches the boundary $\partial G_n/\partial x_0$ and $\partial G_n/\partial z_0$ have the variations of the type $1/r^2$. The integrands still remain nonsingular so long as $\mathbf{x}_0$ is not on the boundary. However, the behavior of $\partial G_n/\partial x_0$ and $\partial G_n/\partial z_0$ (and to a lesser extent that of $\partial G/\partial x_0$, $\partial G/\partial z_0$ and G as well) results in very steep variations of the integrands over a few adjacent intervals Γ_1 and Γ_2 (fig. 2.5) closest to the point $\mathbf{x}_0$. This is the essential problem of the computation of the internal field at a point close to the boundary being unacceptably erroneous. Though Gauss-quadrature rule normally has a high degree of accuracy, it is found in table 2.1 that even a 10-point Gauss integration fails to give satisfactory results in such a situation. Furthermore, as shown later in chapter 3 in a slightly different context, the accuracy of the integration can not be increased significantly by using a higher order quadrature rule. It turns out that the critical factor is the angle subtended by the interval of the integration at the point $\mathbf{x}_0$. An effective procedure in this

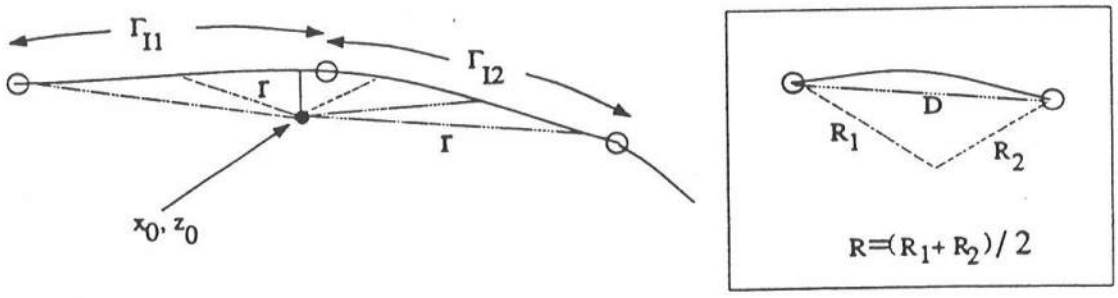

Figure 2.5: An internal point close to the boundary Γ

case is to split the integration over the original interval Γ_1 and Γ_2 as sum of integrations over several subintervals. Each subinterval is constructed such that the normally adopted integration procedure is adequately accurate for the integration over this range. This is possible through a simple criterion of limiting the range of the subinterval given by

$$\frac{D}{R} < \left[\frac{D}{R}\right]_c \tag{2.99}$$

where D and R for a subinterval are illustrated in fig. 2.5. The critical value $[D/R]_c$ depends on the procedure used for the integration. For a 10-point or 8-point Gauss integration a value of 0.5 for $[D/R]_c$ is found to be adequately accurate.

We again consider the same problem shown earlier in table 2.1. Results of the computation of ϕ, ϕ_x and ϕ_z at the same three locations are shown in table 2.2. Nodes on the boundary are still distributed with the same uniform spacing of 0.25. However, subintervals between two consecutive nodes are now used to perform the integrations. Fig. 2.6 shows the original configuration of the domain near the point of interest and the subdivisions of the usual integration intervals between consecutive nodes marked by circles. Solid bullets show the subdivisions. The actual procedure of deciding the subintervals is discussed in chapter 3; however, we note that the length of a subinterval gets smaller if the subinterval considered is closer to the interior point. It is clear from table 2.2 that the procedure developed for computing the internal field close to the boundary is very accurate. Besides enabling accurate computation of the velocity field close to the

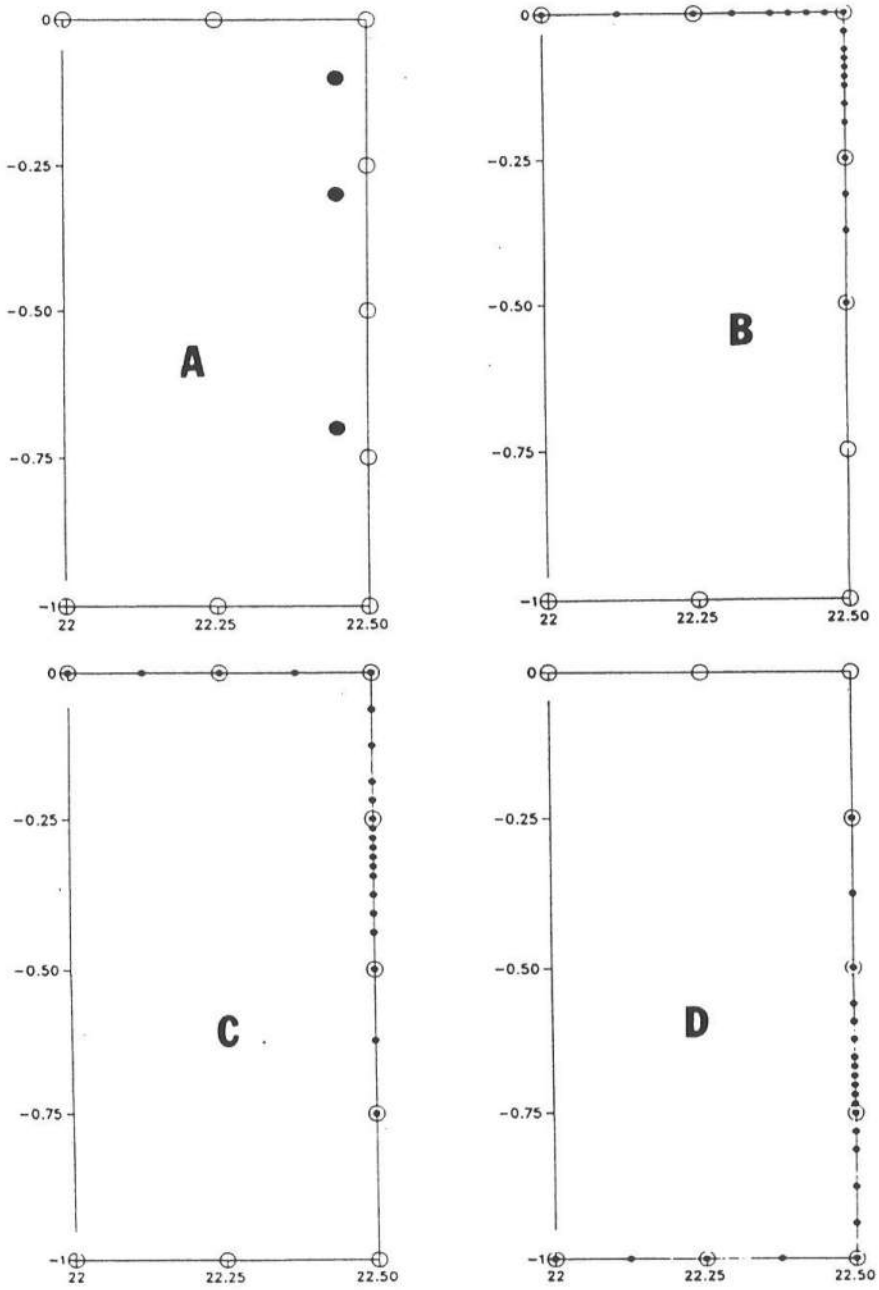

Figure 2.6: Original configuration and the locations of the three internal points (large bullets) are shown in A. Though not shown in the plot, each corner is treated by the 'double-node' technique. The subdivisions of each element are shown by the small bullets in B for the internal point having $z_0 = -0.1$, in C for $z_0 = -0.3$ and in D for $z_0 = -0.7$. $x_0 = 22.45$ for all the three internal points.

Table 2.2: Computed ϕ, ϕ_x and ϕ_z at three interior points using integration by subdivisions. The exact values are $\phi(x_0, z_0) = 20.2050$, $\phi_x(x_0, z_0) = 0.9$ and $\phi_z(x_0, z_0) = 0.0$.

Integration by subdivisions

x_0	z_0	ϕ	ϕ_x	ϕ_z
22.45	-0.1	20.204999999997	0.899999999996	0.000000000004
22.45	-0.3	20.204999999997	0.899999999996	0.000000000004
22.45	-0.7	20.204999999997	0.899999999997	0.000000000004

boundary, it has been a crucial factor in the implementation of the radiation boundary in chapter 5.

Chapter 3

CORNERS AND MOVING BOUNDARIES

3.1 Introduction

It is generally recognized that the boundary integral solution has large error and poor convergence near a corner (*e.g.*, Schultz and Hong, 1989; Grilli *et al.*, 1990 and Grilli & Svendsen, 1990). For boundary value problems over a large domain, these errors may not be of significance unless one is interested in accurate details near the corner. In a time marching scheme, however, the errors originated near the corner may not remain confined to the region of origin. In nonlinear free surface problems, both the potential and the position of the free surface are determined through a numerical evolution based on the solution at the previous time step. Thus, the propagation and the accumulation of these errors may have serious effects on the numerical stability and accuracy of the solution over a domain containing corners. Computational difficulties have been reported by several authors regarding the use of boundary integral methods on processes like wave generation (Dommermuth, 1988) and runup on slopes (Klopman, 1987). Thus, an attempt is made here towards understanding the nature of the difficulties near the corners and some remedies are developed. Further, the remedies presented here may also find use in boundary integral models using different formulations though the present discussion is based on the integral form of the Laplace equation derived by using Green's theorem.

3.2 Implications of a Corner in a Boundary Integral Model

Within the framework of potential theory singularities may exist at a corner in the behavior of the fluid motion under certain circumstances. A familiar example is the potential flow confined between two walls intersecting at an angle (interior to the fluid domain) exceeding π (see Batchelor, 1967). There are other examples of more complicated

problems one of which occurs during the impulsive start of a wave maker and is briefly discussed in the next chapter. Some important limitations exist in using a boundary integral method for potential flows which have singular solutions. First, we note that an assumption used during the derivation of (1.19) in chapter 1 is that ϕ_n remains bounded. As this assumption is likely to be violated for a singular flow, derivation of the integral form needs to be again looked at. Secondly, continuous variation of the integrand is approximated by a polynomial variation based on values at discrete nodal points as part of the discretization leading to the final solution of the integral equation as an algebraic system. Singular variation of the fluid motion can not be properly represented by using this type of discretization.

The presence of a corner in a computational domain does not, however, necessarily imply singularity in spite of the multi-valuedness of the normal vector to the boundary at the corner. It is, therefore, important to distinguish these two different situations for discussing the errors in the solution of a boundary integral model near a corner. In the present work fluid motion having singular or non-analytical behavior is not discussed. In nonsingular flows, the errors are caused due to numerical artifacts. We discuss these factors in the following, first by considering examples from steady flows and then looking at some particular problems at an intersection of two moving boundaries.

3.3 Multi-valuedness of the Normal Vector

The normal vector to the boundary changes its direction discontinuously across the corner. As a result, the normal derivative ϕ_n and the tangential derivative ϕ_s of the potential ϕ are discontinuous at the corner even though ϕ is well-behaved and analytical. Based on the earlier works, 'double-node' technique has been used here as mentioned in the previous chapter. This technique has been found to be an effective and accurate way for the numerical treatment of the multi-valuedness of the normal vector at the corner. It has also been discussed in several places in the previous chapter that one has to be careful about suitably modifying the discrete form of the integral equation so that the coefficient matrix does not degenerate to a lower rank or become ill-conditioned and follow a proper definition of the tangential and normal derivatives at the 'double-nodes'.

3.4 Variation of $G(\mathbf{x},\mathbf{x}_0)$ and $G_n(\mathbf{x},\mathbf{x}_0)$ Near a Corner

To illustrate the errors arising out of the variation of $G(\mathbf{x},\mathbf{x}_0)$ and $G_n(\mathbf{x},\mathbf{x}_0)$ near a corner we consider a simple flow of uniform current of normalized velocity 0.9 in a rectangular computational domain (fig. 3.1). Length and height of the domain are respectively 10 and 1 in normalized units. ϕ is specified on the free surface (top side) and ϕ_n on the rest

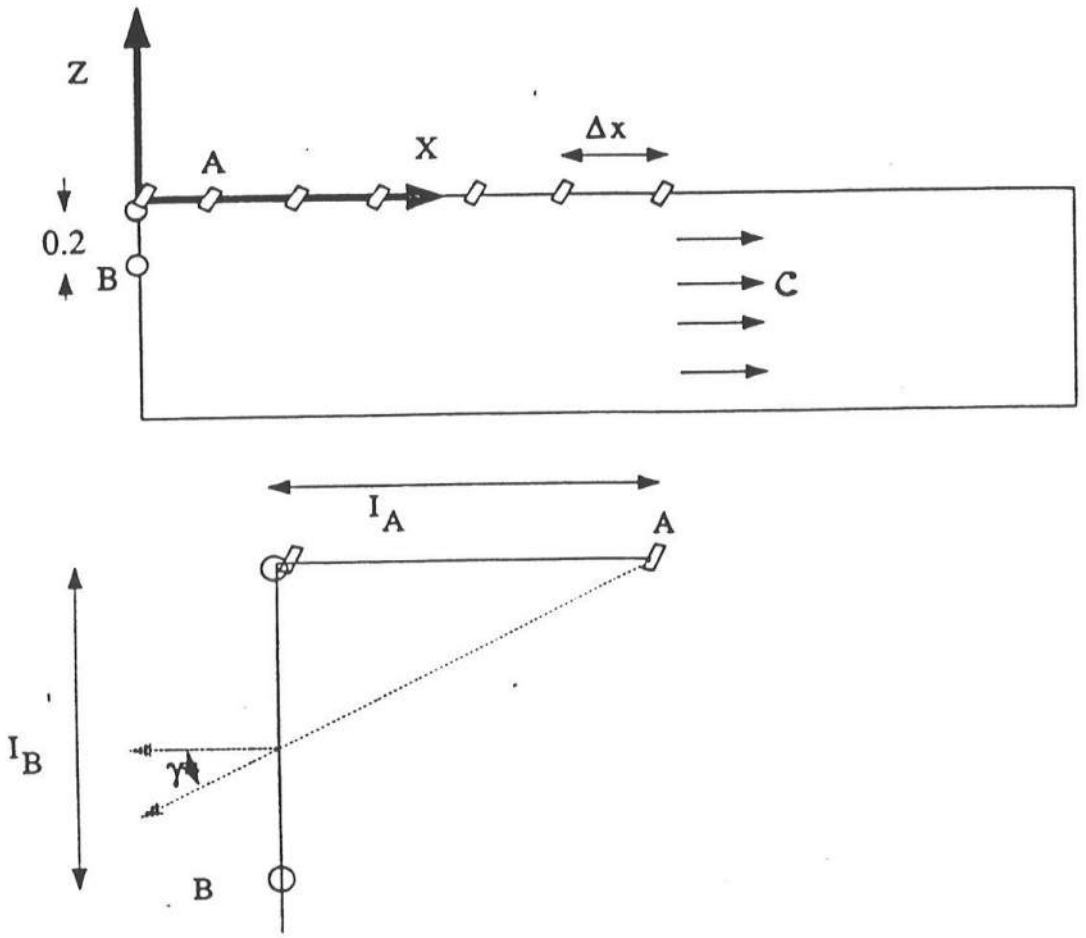

Figure 3.1: Top: computational domain for a uniform current C. Normalized length and height of the domain are respecitvely 10 and 1. Bottom: magnification of the corner at the origin. γ is the angle between the normal to the boundary and the coordinate vector from a collocation point.

of the boundary. The exact value of ϕ_n along the top side is zero for this case and hence, any nonzero value of the computed ϕ_n along this side reflects the error in the solution. The nodes are placed at an uniform spacing of 0.2 on all sides except on the top side. The

spacing Δx on the top side is uniform, but varies for each different computation. The boundary integral solution of this problem is obtained by using linear (2-node) elements with a 10-point Gauss-quadrature rule for the integration. Fig. 3.2 shows the computed ϕ_n for different Δx's on the top side. Though the errors shown in the figure are small, the

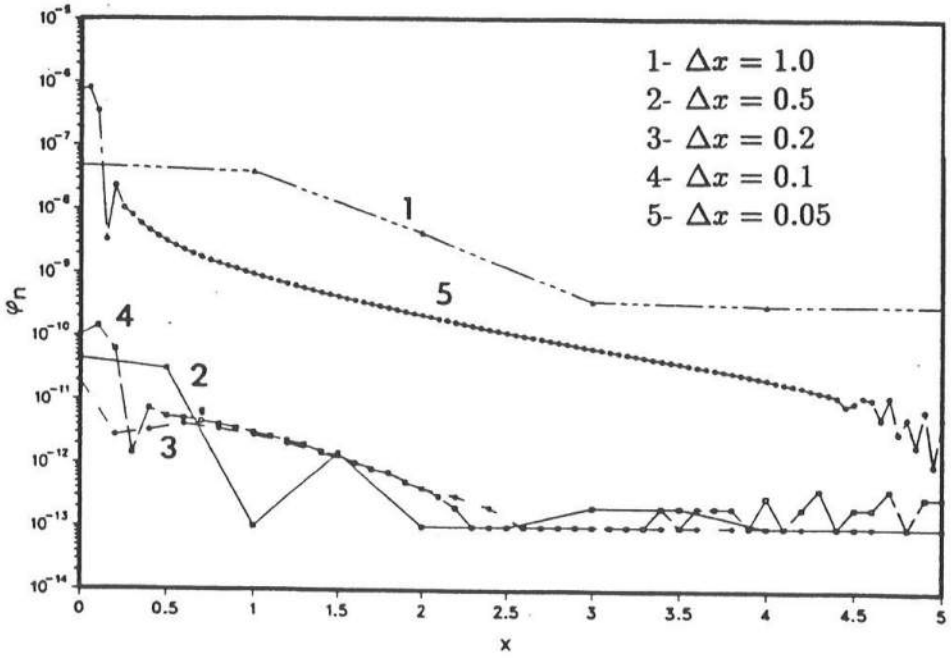

Figure 3.2: Errors in the computed ϕ_n on the free surface for a steady current of velocity 0.9 on uniform depth.

two chief features are:

1. errors in the computed ϕ_n are higher towards the corner in each case,

2. the solution is nonconvergent near the corner for decreasing Δx; errors decreasing initially for Δx reduced from 1 to 0.2 and then increasing again with further reduction of Δx.

3.4.1 Analysis of the Error

The accuracy of the solution of the integral equation (2.31) depends on the numerical evaluation of the coefficients $K^u_{i,l}$ and $K^q_{i,l}$. Recall from the previous chapter that these coefficients are

$$K^u_{i,l} = \int_{-1}^{1} N_l[\mu(\xi)] G_n(\mathbf{x}, \mathbf{x}_0) J(\xi) d\xi, \tag{3.1}$$

$$K^q_{i,l} = \int_{-1}^{1} N_l[\mu(\xi)] G(\mathbf{x}, \mathbf{x}_0) J(\xi) d\xi. \tag{3.2}$$

The variation of the functions $G(\mathbf{x},\mathbf{x}_0)$ and $G_n(\mathbf{x},\mathbf{x}_0)$ depend upon the position of $\mathbf{x}_0$ with respect to the interval of integration. Consider the evaluation of K^u and K^q on the interval I_B due to a collocation point $\mathbf{x}_A$ as shown in fig. 3.1. To emphasize the effect $G(\mathbf{x},\mathbf{x}_A)$ and $G_n(\mathbf{x},\mathbf{x}_A)$ have on the numerical evaluation of the coefficients, we consider the integrals

$$\int_{z_B}^{0} G_n(\mathbf{x},\mathbf{x}_A) dz = \frac{1}{2\pi} \int_{z_B}^{0} \frac{1}{\sqrt{x_A^2 + z^2}} \cos\gamma \, dz$$

$$= \frac{1}{2\pi} \int_{z_B}^{0} \frac{x_A}{x_A^2 + z^2} dz, \tag{3.3}$$

$$\int_{z_B}^{0} G(\mathbf{x},\mathbf{x}_A) dz = \frac{1}{2\pi} \int_{z_B}^{0} \ln\sqrt{x_A^2 + z^2} dz \tag{3.4}$$

Defining a new variable $z' = z/x_A$, one has

$$I_{G_n} = \int_{z_B}^{0} \frac{x_A}{x_A^2 + z^2} dz = \int_{z'_B}^{0} \frac{1}{1 + z'^2} dz', \tag{3.5}$$

$$I_G = \int_{z_B}^{0} \ln\sqrt{x_A^2 + z^2} dz = x_A \int_{z'_B}^{0} \left[\ln x_A + \frac{1}{2}\ln(1 + z'^2)\right] dz'. \tag{3.6}$$

Exact expressions for the two integrals on the right hand side of (3.5) and (3.6) can be found (see Gradshteyn & Ryzhik, 1980) and these are

$$I_{G_n} = -\arctan(z'_B), \tag{3.7}$$

$$I_G = -x_A z'_B \ln x_A - \frac{x_A}{2}\left[z'_B \ln(1 + {z'_B}^2) - 2z'_B + 2\arctan(z'_B)\right]. \tag{3.8}$$

The performance of the numerical evaluation of I_{G_n} and I_G can thus be assessed by comparing with the exact expressions (3.7) and (3.8). The error naturally depends on

Table 3.1: Error in the numerical evaluation of I_{G_n} and I_G as function of z'_B ($z'_B = z_B/x_A$). In these examples, z_B is constant (-0.2). x_A varies resulting in different values of z'_B.

Gauss points	$-z'_B$	$\lvert I_{G_n}\rvert$ (numerical)	|Error|	$\lvert I_G\rvert$ (numerical)	|Error|
10	1	0.7853981634	0.6357415E-13	1.6502378685	0.5107026E-14
10	2	1.1071487176	0.1808098E-09	0.7165866303	0.6212234E-10
10	4	1.3258163931	0.1270611E-05	0.1098278637	0.4893286E-07
10	8	1.4465419512	0.1006189E-03	-0.2365960245	0.4905177E-05
10	16	1.5055028224	0.2874694E-02	-0.4211769637	0.8284519E-04
10	32	1.5670170523	0.2746056E-01	-0.5166464843	0.1392123E-03

the integration procedure used. Table 3.1 shows the errors in the numerical integration if Gauss-quadrature rule is used with 10 Gauss points. It is clearly seen that the numerical integration deteriorates rapidly as z'_B (z_B/x_A) increases. It follows in a similar way that the numerical evaluation of I_{G_n} and I_G over the interval I_A due to a source point at B deteriorates as x_A/z_B decreases.

The errors in the numerical evaluation of I_{G_n} and I_G explain the observed errors in fig. 3.2 in the following way. With large Δx on the top side of the computational domain (relative to the spacing on the vertical side) the coefficients K^q and K^u evaluated on the interval I_A due to a collocation point at B become less accurate. This results in larger error in the computed solution near the corner. As Δx decreases on the top side, K^q and K^u evaluated on the interval I_B due to a collocation point at A become less accurate. This is the reason why the solution is non-convergent near the corner.

3.4.2 Accurate Evaluation of the Integrals near the Corner

The error and the nonconvergence near the corner can be removed by improving the numerical evaluation of $K^q_{i,l}$ and $K^u_{i,l}$. The errors in table 3.1 are based on 10-point Gauss-quadrature rule. Integrations by other formulae such as Newton-Cotes lead to much higher error (see Atkinson, 1976). Thus, as the first alternative numerical integration with more Gauss points may be considered to achieve higher accuracy. However, it is shown in table 3.2 that the error decreases very slowly when higher order quadrature rule is used.

Table 3.2: Error in the numerical evaluation of I_{G_n} and I_G as function of Gauss points.

Gauss points	$-z'_B$	I_{G_n} (numerical)	|Error|	I_G (numerical)	|Error|
8	16	1.5134486504	0.5071134E-02	-0.4210628484	0.1969604E-03
10	16	1.5055028224	0.2874694E-02	-0.4211769637	0.8284519E-04
12	16	1.5078529310	0.5245858E-03	-0.4212615105	0.1701680E-05
14	16	1.5085022165	0.1246997E-03	-0.4212633408	0.3531958E-05
16	16	1.5084179184	0.4040162E-04	-0.4212599931	0.1842508E-06

It is clear from table 3.1 that the error in the numerical integration gets rapidly smaller for smaller $|z'_B|$. Thus, an effective procedure to improve the numerical integration is to split the original integration interval Γ_I to several subintervals such that the equivalent $|z'_B|$ for each subinterval is desirably small. This can be done by requiring that θ, the angle subtended at a collocation point $\mathbf{x}_i$, by each subinterval is less than a preset value $\theta_{\max}$. The choice of $\theta_{\max}$ depends on the integration procedure used. If 10-point Gauss-quadrature is used it can be seen from table 3.1 that the error in the numerical integration is almost as low as the truncation error for $\theta_{\max} = 45°$. The integration over the original interval is then obtained as sum of the integrations over each subinterval.

The numerical procedure adopted for subdividing the original interval for the purpose of the integration is as follows:

1. Check if the subtended angle θ at the collocation point by the integration interval is greater than $\theta_{\max}$,
2. divide the interval to two equal halves if $\theta > \theta_{\max}$,
3. repeat the procedure for each subinterval.

An example of the resulting sets of subintervals are shown in fig. (3.3) of an element near the corner for different values of $\theta_{\max}$. The number of subintervals depend on the location of the collocation point. If the collocation point is located away from the corner no subdivision of the interval of integration is necessary. This way the actual integration interval is adapted to minimize the errors in the numerical evaluation of the coefficients K^q and K^u and this procedure is, henceforth, referred to as the 'adaptive integration'

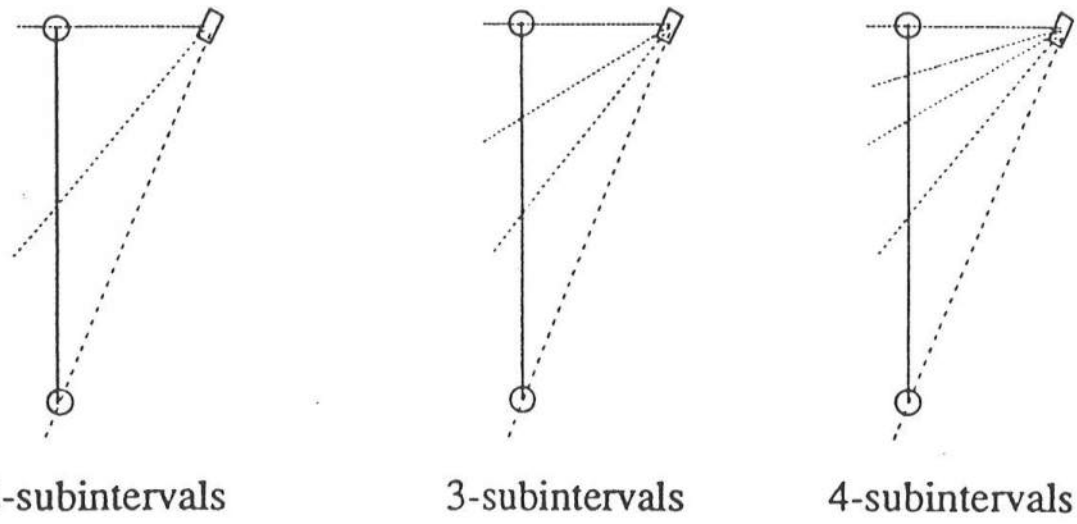

Figure 3.3: A typical scheme of subdivisions based on the subtended angle

technique. Table (3.3) shows the error in the numerical evaluation of I_{G_n} and I_G by using the 'adaptive integration' technique. It is significant to note that the error decreases dramatically by carrying out the adaptive integration than by increasing the number of Gauss points.

Table 3.3: Error in the numerical evaluation of I_{G_n} and I_G by using 'adaptive integration'.

Gauss points	no. of divs.	$-z'_B$	I_{G_n} (numerical)	|Error|	I_G (numerical)	|Error|
8	2	16	1.5074296064	0.947910E-03	-0.4212514568	0.835210E-05
8	3	16	1.5083987222	0.212054E-04	-0.4212599610	0.152116E-06
8	4	16	1.5083774873	0.295379E-07	-0.4212598091	0.236247E-09
10	2	16	1.5084781357	0.100618E-03	-0.4212622615	0.245258E-05
10	3	16	1.5083762462	0.127061E-05	-0.4212597966	0.122332E-07
10	4	16	1.5083775166	0.180810E-09	-0.4212598089	0.776499E-11

The computations reported in fig. (3.2) are now returned to with the coefficients $K^u_{i,l}$ and $K^q_{i,l}$ evaluated by the 'adaptive integration' technique just described. The results are shown in fig. 3.4. It is seen that the errors near the corner ($x = 0$) for all Δx's are almost as low as the truncation error and not higher than the error occurring in the middle

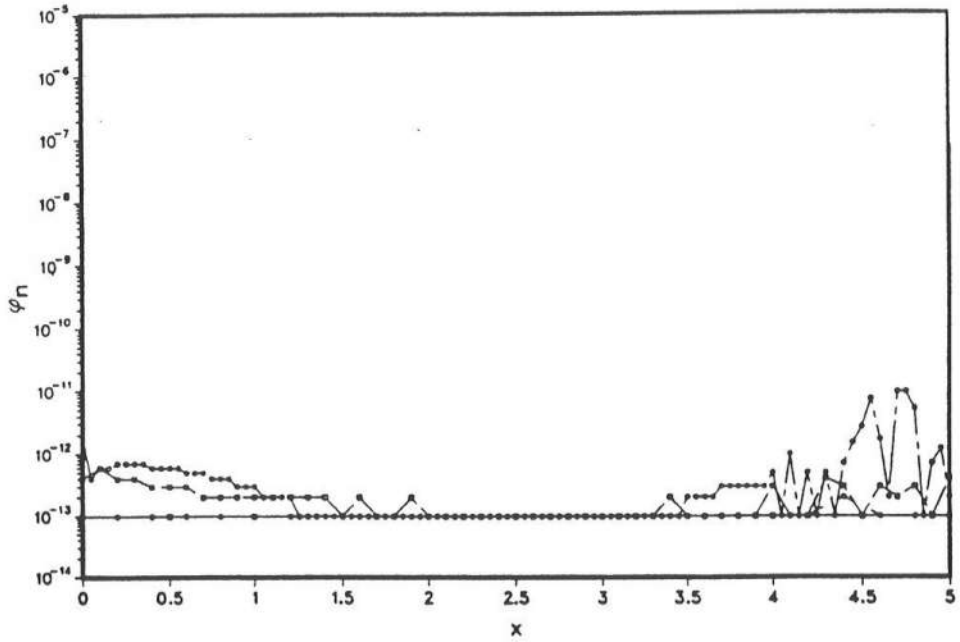

Figure 3.4: Errors in the computed ϕ_n on the top side of the domain shown in fig. 3.1 using 'adaptive integration'. The different curves correspond to different Δx's as in fig. 3.2, but are not marked since the errors are as low as the truncation error for all cases.

of the top side ($x = 5$). From the point of numerical efficiency, it is important to realize that the normally adopted 8-point or 10-point Gauss quadrature rule provides sufficient accuracy except at the corners. Thus, a proper criterion to identify the intervals requiring 'adaptive integration' for each collocation point is desirable to minimize unnecessary additional integrations. The criterion based on the subtended angle seems to be satisfactory for this purpose.

3.5 Rapid Variation of the Flow Variables Near a Corner

In case of uniform flow in a rectangular domain, variation of the potential ϕ is linear and ϕ_n is constant on each side. The role of G and G_n in the errors in the solution of (2.31) has been illustrated by considering such a flow in the previous section. It is, however, possible that the variation of ϕ or ϕ_n may itself be rapid near a corner in several situations. The numerical procedure must account for the rapid variation of the flow

quantities in addition to the difficulties arising out of the variation of G and G_n near a corner. It is difficult to present a general treatment of such types of flows. However, the interesting numerical aspects of a boundary integral solution of (2.31) for such a situation can be discussed by considering a flow confined by two intersecting walls .

The complex potential $W(\zeta)$ for the fluid motion confined between two intersecting walls is (see Batchelor, 1967)

$$W(\zeta) = A\zeta^n \tag{3.9}$$

with ζ as the complex coordinate $x + iz$, the origin being at the corner. n in (3.9) is related to θ_E, the angle between the two walls interior to the fluid domain, by

$$n = \pi/\theta_E \tag{3.10}$$

For real A, the potential ϕ, stream function ψ and the velocities (u, w) may be expressed in terms of the real variables r and θ as (see fig. 3.5)

$$\phi(r,\theta) = Ar^n \cos n\theta \tag{3.11}$$

$$\psi(r,\theta) = Ar^n \sin n\theta \tag{3.12}$$

$$\frac{dW}{d\zeta}(\zeta) = An\zeta^{n-1} \tag{3.13}$$

$$u(r,\theta) = Anr^{n-1} \cos(n-1)\theta \tag{3.14}$$

$$w(r,\theta) = -Anr^{n-1} \sin(n-1)\theta \tag{3.15}$$

For $n \geq 1$ ($\theta_E \leq \pi$), the flow is nonsingular everywhere. Thus, discretizations based on the polynomial approximation of the variation of ϕ and ϕ_n can be expected to lead to accurate solution.

As smaller θ_E is considered, order of the variation of ϕ and ϕ_n becomes higher. At the same time the subtended angle at a collocation point due to an interval of integration near the corner increases. As an example, we consider the boundary integral solution of the flow given by (3.9) with $n = 4$ and $A = 1$. The computational domain is shown in fig. 3.5 which is bounded by two artificial sides 3 and 4. Sides 1 and 2 represent the two impermeable walls intersecting at an angle of $\pi/4$. The specified boundary conditions are as follows: ϕ on sides 1 and 4 according to (3.11); ϕ_n on side 3 according to (3.14)

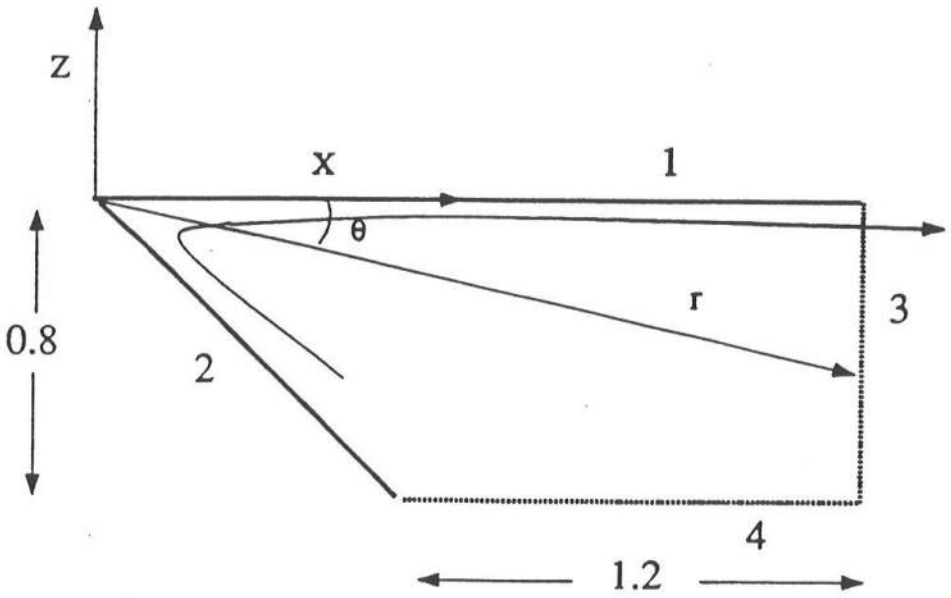

Figure 3.5: Computational domain for the flow between two intersecting walls (side 1 and side 2). Sides 3 and 4 are artificial computational boundaries.

and $\phi_n = 0$ on side 1. The exact value of ϕ_n on side 1 is zero. Thus, a measure of the computational accuracy is easily obtained by comparing the computed ϕ_n on side 1 with the exact value. The highest variation of ϕ on side 1 or of ϕ_n on side 2 is r^4 for this problem.

The computed ϕ_n on side 1 is shown in fig. 3.6 for each different computation. The discretizations are based on the 'Finite element approach' as described in chapter 2. Nodes are uniformly distributed on each side with the vertical spacing Δz on side 2 or 4 being equal to the horizontal spacing Δx on side 1 or 3. Fig. 3.6 shows that discretization based on 3-node elements (curve 4) results in significant drop in the error with the same nodal spacing than if 2-node elements (curve 3) are used. Computations with adaptive integration (not shown in the graph) show only marginal improvement in the case of 2-node or 3-node elements. This is due to the fact that the error in the computation in this case is largely due to the poor representation of the flow variation. Curves 5 and 6 correspond to the computations using 5-node element with $\Delta x = 0.1$ and

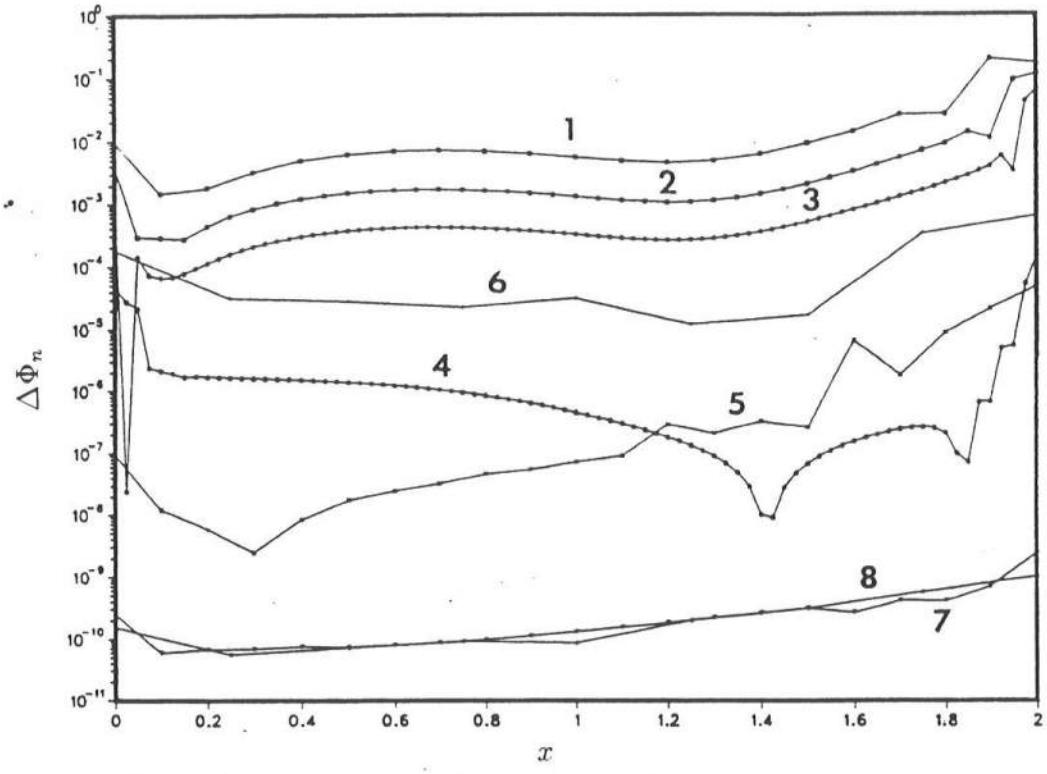

Figure 3.6: Errors in the computed ϕ_n on side 1 of the domain shown in fig. 3.5. Each curve is due to a different order of element used and/or different nodal spacing. Curves 1: 2-node, $\Delta x = 0.1$; 2: 2-node, $\Delta x = 0.05$; 3: 2-node, $\Delta x = 0.025$; 4: 3-node, $\Delta x = 0.025$; 5: 5-node, $\Delta x = 0.1$, no adaptive integration; 6: 5-node, $\Delta x = 0.25$, no adaptive integration; 7: 5-node, $\Delta x = 0.1$, adaptive integration; 8: 5-node, $\Delta x = 0.25$, adaptive integration.

$\Delta x = 0.25$, but with no adaptive integration at the corner. Since the variation of ϕ or ϕ_n is r^4 for the flow under investigation, an exact description of the variation is achieved by using 5-node elements independent of the nodal spacing. At the same time, however, the integration interval is larger since it spans more nodes and larger spacings are used for curves 5 and 6. This results in loss of accuracy in the evaluation of the coefficients K^q and K^u - a disadvantage associated with discretization based on 'finite element' approach. This disadvantage of using higher order elements and larger Δx can be removed by using the technique of 'adaptive integration'. Curves 7 and 8 show the computed results using the same discretizations as in 5 and 6 respectively with the difference that K^q and K^u are evaluated using adaptive integration. It is interesting to see that the errors in the

computation based on 3-node element is significantly large compared to that in curve 8 in spite of Δx being 10 times smaller! Further, both curves 7 and 8 yield the same level of accuracy in spite of the very different Δx used for the two.

Finally, the example shows that the boundary integral procedure can yield accurate and convergent solution near a corner effectively by using higher order elements and the 'adaptive integration' technique as described in this chapter.

3.6 Intersection of Moving Boundaries

In the previous sections, errors near the corner in the solution of (2.31) satisfying a set of properly specified boundary conditions have been investigated. In unsteady motions involving a moving free surface, both the position of the free surface and the boundary data on it are determined through numerical updating. Due to the numerical inaccuracies both the position and the boundary data are likely to develop some errors with evolution in time. At an intersection of two sides these errors may lead to unacceptable numerical behavior. The problem which arises near the intersection depends on the type of the boundary condition specified on each of the intersecting sides and the included angle between them. Thus, a general discussion of these problems is rather difficult.

To fix ideas, we consider an intersection of the free surface (Dirichlet condition) with a wave maker (Neumann condition) as shown in fig. 3.7. In fig. 3.7 the node, denoted by the index $I1$, belongs to the free surface and that, denoted by $I2$, belongs to the wave maker. In the case of generation by a rigid wave maker, the lateral boundary follows the motion of the wave maker. The free surface node $I1$ is free to move tangentially along the wave maker, but should have the same velocity normal to the wave maker as that of the wave maker itself. In the computational procedure, the new position of this node is evaluated according to the usual free surface updating described in chapter 2 whereas the new position of the wave maker is determined by an analytical function describing the wave maker motion. The kinematic boundary condition requires that the fluid particle on the wave maker stay on the wave maker. However, inexactness in the numerical updating may result in the free surface node not satisfying this condition exactly. This condition is enforced by modifying the position of the free surface node to its projection on the

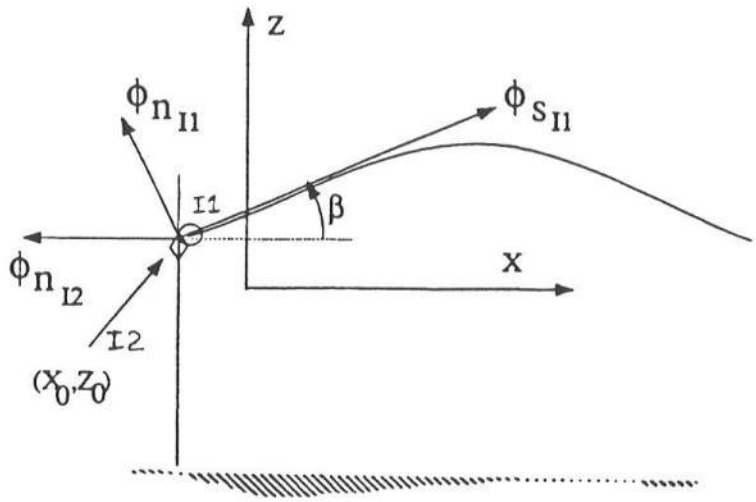

Figure 3.7: Sketch of an intersection of the free surface with a lateral Neumann boundary.

wave maker. This way the kinematic condition is satisfied with the minimum deviation of the actually computed position. Observations during typical computations show that the magnitude of of the necessary adjustment is very small, being of the order of $10^{-6}\Delta x$ at each time step. The modified position defines the new intersection point on the wave maker.

More attention becomes necessary for steep gravity waves. Though wave generation is discussed in more details in the following chapter we consider an example here (fig. 3.8) to illustrate the problem. Computations start with an initially still free surface and the wave maker displacement $\xi(t)$ is prescribed by the expression

$$\xi(t) = S(t)A(t)\sin\omega t \tag{3.16}$$

with

$$S(t) = \frac{\tanh(bt/T - \lambda) + \tanh\lambda}{1 + \tanh\lambda} \tag{3.17}$$

where T is the wave period and $\omega = 2\pi/T$. The values of b and λ used for the computations shown in fig. 3.8 are 1.981 and 4.0 respectively. The choice and significance of $S(t)$

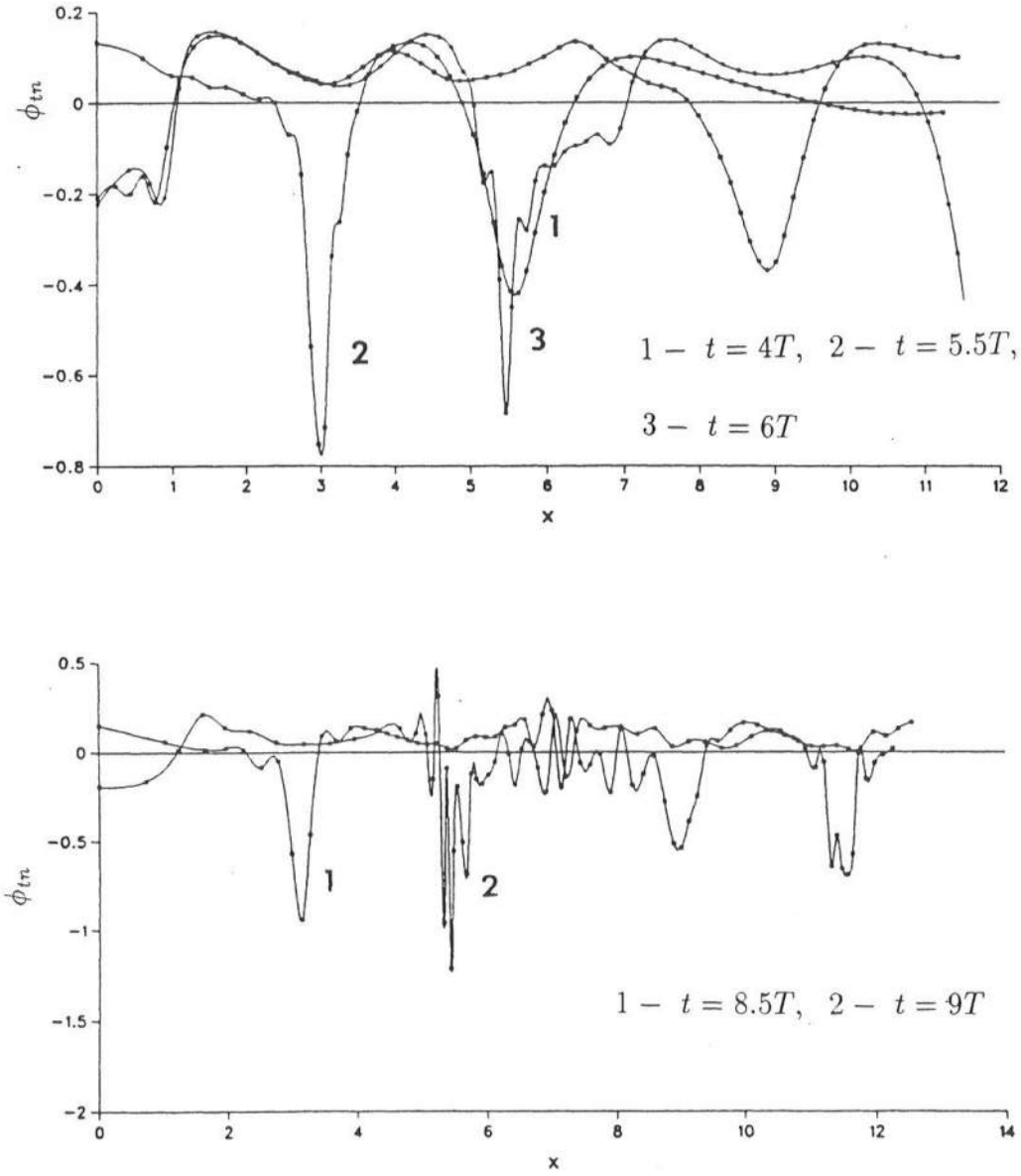

Figure 3.8: Growth of oscillations in the computed ϕ_{tn} on the free surface during generation by a piston wave maker. Normalized wave height near the wave maker is 0.375 and the normalized wave period T is 6.656. Quasi-spline elements are used on the free surface with initial $\Delta x = 0.175$. $\Delta t = 0.052$.

are discussed in the following chapter. The emphasis here is to draw attention to the oscillations which grow unacceptably high for the computation to continue.

3.6.1 Analysis of the Problem

During the temporal evolution of the free surface, normal flux ϕ_n is specified on the wave maker and the potential ϕ on the free surface is obtained following the updating procedure described in chapter 2. Solution of the Laplace equation at any instant subject to the specified boundary conditions must satisfy

$$(\phi_s \cos\beta - \phi_n \sin\beta)_{I1} = -\phi_{n_{I2}} \tag{3.18}$$

at the intersection. $\phi_{n_{I2}}$ is assumed specified exactly based on a predetermined motion of the wave maker whereas numerical inaccuracies in the updated ϕ may introduce small deviation in ϕ_s at the node $I1$. From (3.18), it follows that

$$\Delta\phi_{n_{I1}} = \frac{\cos\beta}{\sin\beta}\Delta\phi_{s_{I1}} \tag{3.19}$$

where $\Delta\phi_{n_{I1}}$ is the sensitivity of the computed $\phi_{n_{I1}}$ to a deviation $\Delta\phi_{s_{I1}}$ at the node $I1$. (3.19) shows that $\Delta\phi_{s_{I1}}$ results in a magnified deviation in $\phi_{n_{I1}}$ when the angle β is small. In turn, the magnified deviation in $\phi_{n_{I1}}$ causes magnified error in the updated position of the free surface node $I1$. This effect can then spread with time and away from the corner.

A particular case arises when $\beta = 0$. Expression (3.18), in this case, reduces to

$$\phi_{s_{I1}} = -\phi_{n_{I2}} \tag{3.20}$$

Equation (3.20) is in fact a statement on the requirement of the specified $\phi_{n_{I2}}$ and $\phi_{s_{I1}}$ when the angle β between the two intersecting sides is zero. $\phi_{s_{I1}}$, however, may not exactly satisfy (3.20) due to numerical inaccuracies in the updated ϕ. This corresponds to creating a mild singularity (sudden start of the wave maker) through the inconsistent boundary conditions. Analytical analysis of this kind of problem is rather complex (Chwang, 1982; Roberts, 1987) and we shall visit this problem briefly in chapter 4. Following Roberts (1987), it seems that such inconsistencies in the boundary condition may lead to much larger ϕ_n and faster oscillations of the free surface.

3.6.2 Solution Procedure

The idea pursued here is to minimize $\Delta\phi_{s_{I1}}$ in (3.19) and satisfy (3.20) for $\beta = 0$ by modifying ϕ near the intersection based on the specified ϕ_n on the Neumann boundary.

We first consider the case when $\beta = 0$ to present the basic idea of how the potential on the free surface obtained from regular updating is modified. Following the procedure described in chapter 2, $\phi_{s_{I1}}$ is expressed in terms of the discrete nodal values of ϕ by

$$\phi_{s_{I1}} = \sum_{l=1}^{P} \frac{d\xi}{ds} N_l'(\xi)\phi_l;\ \xi = -1 \tag{3.21}$$

where l denotes the local index of a node in $[-1 \leq \xi \leq 1]$ and $(P-1)$ denotes the order of the polynomial used to compute the derivative at the node $I1$. The node $I1$ corresponds to $l = 1$ ($\xi = -1$). In (3.21) the derivative $\phi_{s_{I1}}$ depends on P nodal values of ϕ. In principle, this leaves us with a wide range of choices as to how to modify the ϕ_l's already computed from the time-updating procedure if $\phi_{s_{I1}}$ should satisfy (3.20). Several possibilities have been investigated and it has been found that modifying only the value of ϕ_{I1} gives the best result. This in fact is also a satisfactory choice because it reduces the modification of the free surface potential computed by the regular procedure to a minimum. Thus, we satisfy (3.20) by modifying only ϕ_{I1} according to

$$\phi_{I1} = -\frac{1}{\mathrm{Cf}_1}\left[\phi_{n_{I2}} + \sum_{l=2}^{P} \mathrm{Cf}_l\phi_l\right] \tag{3.22}$$

where

$$\mathrm{Cf}_l = \frac{d\xi}{ds} N_l'(\xi);\ \xi = -1. \tag{3.23}$$

Extension of this procedure to the more general case of $\beta \neq 0$ meets with the difficulty that (3.18) is now to be satisfied instead of (3.20) and $\phi_{n_{I1}}$ in (3.18) is not known prior to the solution of the Laplace equation. However, if ϕ_{I1} is to be modified, ϕ_{I1} must be treated as an unknown in addition to $\phi_{n_{I1}}$ in the solution of the Laplace equation. (3.18) would then provide the additional equation which is needed for the extra unknown by way of ϕ_{I1} in the discrete system. This would result in a $(N+1, N+1)$ system as compared to the (N, N) system in the regular procedure and would not be a very attractive

numerical scheme. Therefore, a new procedure described below is developed to treat this case as a (N, N) matrix.

The effect of ϕ_{I1} can be eliminated from the discrete system (2.77) by using the equality of ϕ_{I1} and ϕ_{I2} [equation (2.83)]. If we now define a set of new coefficients $K^{u\prime}_{i,j}$ such that

$$K^{u\prime}_{i,I2} = K^{u}_{i,I2} + K^{u}_{i,I1} + \alpha_{I1}\delta_{i,I1}, \tag{3.24}$$

$$K^{u\prime}_{i,I1} = \alpha_{I1} = 0, \tag{3.25}$$

$$\alpha'_i = \alpha_i,\ i \neq I1, \tag{3.26}$$

$$K^{u\prime}_{i,j} = K^{u}_{i,j},\ j \neq I1, I2 \tag{3.27}$$

the modified form of (2.77) becomes

$$\alpha'_i\phi_i = K^{q}_{i,j}\phi_{n_j} - K^{u\prime}_{i,j}\phi_j. \tag{3.28}$$

Since the coefficients of ϕ_{I1} are set to zero, any value can be used for ϕ_{I1} with no effect in the solution of (3.28). Hence, one can seek a solution to (3.28) with $\phi_{n_{I1}}$ at node $I1$ and ϕ_{I2} at node $I2$ as the unknowns. Finally, the modified value of ϕ_{I1} can be obtained from the value of ϕ_{I2} by using the equality of the two. This is the procedure used here. As mentioned earlier in chapter 2, (3.28) should be replaced by an appropriate equation at one of the 'double-nodes'. This is done by using

$$\cos\beta[\mathrm{Cf}_1\phi_{I2} + \sum_{l=2}^{l=p}\mathrm{Cf}_l\phi_{I1+l-1}] - \sin\beta\phi_{n_{I1}} = -\phi_{n_{I2}} \tag{3.29}$$

for the $I2$th row corresponding to the node $I2$. Expression (3.29) is obtained from (3.18) by substituting

$$\phi_{s_{I1}} = \mathrm{Cf}_1\phi_{I2} + \sum_{l=2}^{l=p}\mathrm{Cf}_l\phi_{I1+l-1}. \tag{3.30}$$

This procedure is, henceforth, referred to as the "BC-correction" procedure for it contains a mechanism for correcting the updated free surface potential at the intersection based on the specified normal boundary condition.

Considerations for Large β

For a time-dependent boundary like the unsteady free surface the angle β changes from small to large and vice-versa during the temporal evolution. Recall that the angle β as defined in fig. 3.7 is such that the interior angle between the wave maker and the free surface is $(\pi/2 + \beta)$. The 'BC-correction' procedure discussed above seeks to reduce the errors only when β is small, though the procedure does not use any assumption of small β. It is found that the 'BC-correction' procedure introduces error in the solution near the corner when $|\beta|$ assumes a value close to $\pi/2$. This can also be expected from both physical and numerical reasons. For large $|\beta|$, $\phi_{s_{I1}}$ and $\phi_{n_{I2}}$ tend to be orthogonal to each other. Thus, any correction of the variation of ϕ on the free surface based on $\phi_{n_{I2}}$ will be extremely sensitive. Hence, 'BC-correction' procedure is used in the numerical code only if $|\beta| \leq \pi/4$.

Finally, though no mention is made of the procedure in connection with the Laplace equation for ϕ_t, all discussions apply identically when ϕ is replaced by ϕ_t. In the numerical algorithm, 'BC-correction' is used for both the systems.

We now return to the example shown earlier in fig. 3.8. With the same computational parameters, generation of waves by a piston wave maker is now performed using the 'BC-correction' procedure just described. The results are shown in fig. 3.9. It is significant that the spurious oscillations observed in fig. 3.8 can be so effectively reduced by modifying the way the intersection is treated.

3.7 Final Remarks

In this chapter, we have discussed the errors and identified the factors causing the errors in the solution of a boundary integral method based on the Green's theorem. The conclusions can be summarized as follows:

- Errors in the solution of (2.31) near a corner can be reduced to 'desirably' low level for steady, nonsingular flows by a proper treatment of the intersections of the sides of a computational domain.

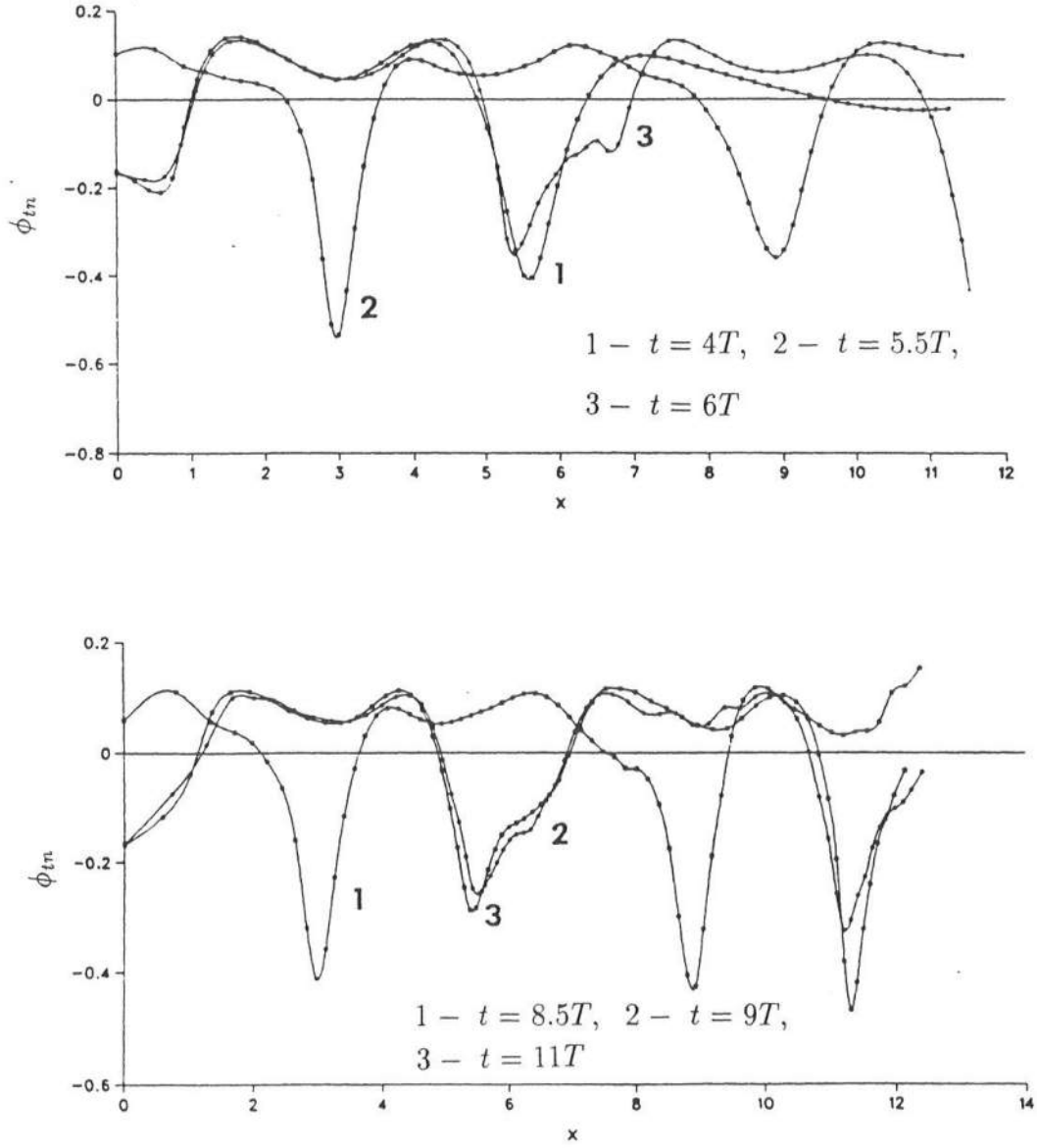

Figure 3.9: Computed ϕ_{tn} on the free surface during generation by a piston wave maker using the 'BC-correction' procedure. The computational parameters are same as in fig. 3.8.

- Behavior of $G(\mathbf{x},\mathbf{x}_0)$ and $G_n(\mathbf{x},\mathbf{x}_0)$ can cause nonconvergence of the numerical solution of (2.31). The nonconvergence can be effectively removed by adopting the adaptive integration procedure in the evaluation of the coefficients $K^q_{i,l}$'s and $K^u_{i,l}$'s.

- In case of unsteady problems, small errors near the corner can magnify and spread away from the corner with time. The spurious oscillations can be reduced by careful considerations of the boundary conditions and the included angle at an intersection.

The 'BC-correction' procedure presented here assumes an intersection of a Dirichlet side and a Neumann side where the Dirichlet side is time-updated through a numerical scheme. This is a commonly occurring problem in the context of nonlinear free surface problems. Reformulation of the procedure is necessary for different types of intersecting sides using the basic idea of removing the inconsistencies in the boundary conditions at the intersection during the temporal evolution.

Chapter 4

FORCED WAVES: GENERATION AND MODULATION

4.1 Introduction

An important element of a 'Numerical Wave Tank' is wave generation. It has been seen earlier that the computation of the unsteady free surface flow can proceed indefinitely from time t_0 if the free surface position η and the velocity potential ϕ on it are known along with a feasible procedure of specifying the lateral boundary conditions. It is usually difficult to find the potential distribution corresponding to an undulated free surface at the initiation of the computation except in a few specific cases. Consequently, in most cases of wave generation the computation must start from the still water condition, *i.e.*, $\eta(x, t = 0) = 0$ and $\phi(x, \eta, t = 0) = 0$. The wave motion may then be caused by the specified conditions on the lateral boundary or by varying the atmospheric pressure distribution on the free surface. In the present work, fluid motion generated by free surface pressure disturbance is not studied. Thus, modeling of the lateral boundary conditions and the resulting wave field are the aspects of wave generation that are under investigation in the following.

4.2 Theoretical Aspects of Transient Start of a Wave Maker

One of the earliest mathematical analyses of waves generated by a rigid body was presented by Havelock (1929). The solution is based on the linearized wave theory for a harmonic wave maker. The verification of the theory for waves of small amplitude by Ursell *et al.* (1960) has provided an important evidence in the validity of the potential theory for waves generated by a rigid body. A detailed account of the solution due to a harmonic wave maker can be found in Dean & Dalrymple (1984).

However, a clear understanding of the fluid behavior due to the transient motion of a wave maker is obscured apparently due to the singularities in the potential theory at the intersection of the free surface and the wave maker. The wave maker problem is formulated as follows. The fluid satisfies the Laplace equation

$$\nabla^2\phi = 0 \tag{4.1}$$

with the free surface conditions

$$\eta_t + \phi_x\eta_x = \phi_z, \ [z = \eta]; \tag{4.2}$$

$$\phi_t + \frac{1}{2}\nabla\phi \cdot \nabla\phi + g\eta = 0, \ [z = \eta]. \tag{4.3}$$

On a piston wave maker with translational velocity $U(t)$ one requires

$$\phi_x = U(t), \ [x = \xi(t)] \tag{4.4}$$

where ξ is the displacement of the wave maker. Impermeability condition is satisfied on the bottom ($z = -h$) and the fluid is assumed to extend to infinity away from the wave maker.

Chwang (1982) has presented a solution to the the nonlinear transient problem by expressing ϕ and η as perturbation series in time. The procedure is valid only for short time after the initiation of the motion. In an unpublished note, Peregrine (1972) also presents a solution to the leading order problem based on a perturbation series in time for the impulsive start of a wave maker. For consistency, we follow Roberts (1987) for the complete discussion. First, Roberts assumes the water depth to be infinite and uses the condition

$$\begin{aligned} \phi_x &= U(t), \ -d \leq z \leq 0 \\ &= 0, \ z \leq -d \end{aligned} \tag{4.5}$$

instead of (4.4) corresponding to non-zero displacement only over a finite depth of water. The vertical plate has a power law displacement $\xi(t)$ over $[-d \leq z \leq 0]$, namely

$$\begin{aligned} \xi(t) &= 0, \ t \leq 0, \\ &= \frac{\alpha t^{p+1}}{\Gamma(p+2)} \ t > 0. \end{aligned} \tag{4.6}$$

If a perturbation expansion in time is followed, *i.e.*,

$$\phi(x,z,t) = \sum_{m=0}^{\infty} t^{p+m}\phi_m(x,z), \tag{4.7}$$

$$\eta(x,t) = \sum_{m=0}^{\infty} t^{p+1+m}\eta_m(x) \tag{4.8}$$

the leading order problem becomes

$$\nabla^2\phi_0 = 0, \tag{4.9}$$

$$\phi_0(x,0) = 0, \quad (p+1)\eta_0 = \frac{\partial\phi_0}{\partial z}(x,0), \tag{4.10}$$

$$\frac{\partial\phi_0}{\partial x} = \frac{\alpha}{\Gamma(p+1)}, \ [x=0, \ z\leq -d],$$
$$= 0, \ [x=0, \ z\leq -d]. \tag{4.11}$$

The corresponding η_0 as obtained by Roberts (1987) is

$$\eta_0 = \frac{\alpha}{\pi\Gamma(p+2)}\ln\left(1+\frac{d^2}{x^2}\right) \tag{4.12}$$

which becomes

$$\eta_0 = \frac{2\alpha}{\pi\Gamma(p+2)}\ln\left(\frac{d}{x}\right), \ x\rightarrow 0. \tag{4.13}$$

A significant feature of following the perturbation expansions (4.7) and (4.8) is that the leading order problem is independent of gravity. Secondly, η_0 given by (4.13) is logarithmically singular at $x = 0$.

Roberts (1987) then shows that if a ϕ and η are expressed through a perturbation series based on the parameter α rather than in time as in (4.7) and (4.8) gravity is retained in the leading order problem, *i.e.*,

$$\phi = \alpha\phi_0(x,z,t) + O(\alpha^2) \tag{4.14}$$

$$\eta = \alpha\eta_0(x,z,t) + O(\alpha^2) \tag{4.15}$$

leads to

$$\frac{\partial\phi_0}{\partial t} + g\eta_0 = 0, \ [z=0] \tag{4.16}$$

as in the classical wave maker problem. This problem is now solved with the initial free surface condition

$$\phi(x, z=0, t=0) = 0, \quad \eta(x, t=0) = 0. \tag{4.17}$$

Roberts shows that for small t near the wave maker one has

$$\eta_0 \sim t^{p+1} \ln t, \tag{4.18}$$

$$\frac{\partial \phi_0}{\partial z} \sim t^p \ln t, \ [z = 0], \tag{4.19}$$

$$\beta \sim -\frac{\alpha}{g\Gamma(p)} t^{p-1} \tag{4.20}$$

where β denotes the maximum surface slope near the origin. Thus, in the wave maker motion given by (4.6), one should have $p > -1$ for η_0 to be bounded, $p > 0$ for $\partial\phi_0/\partial z$ to be bounded and $p \geq 1$ for β to be bounded. We note from (4.6) that the wave maker jumps to finite velocity α and its acceleration is infinite at $t = 0$ if $p = 0$. For $p = 1$, the initial acceleration is finite being equal to α and the velocity increases linearly with time.

An interesting feature of Roberts's analysis is that the surface slope can be indefinitely large if $p < 1$ even though the surface elevation may be bounded. This is due to a dispersive train of waves η_D with fast oscillations which develops near the origin and is of the form

$$\eta_D \sim 4\sqrt{\pi} 2^p \nu^{p+3/2} \cos\left(\frac{gt^2}{4x} + \frac{(1-2p)\pi}{4}\right), \ \nu \to 0, \ t \to 0 \ . \tag{4.21}$$

with the definition $\nu = x/(gt^2)$. Due to the large surface slope that results, nonlinear terms in the free surface conditions and viscosity and surface tension can no longer be assumed insignificant. Thus, the linear theory used to derive the solution is no longer strictly consistent. On a closer look, however, it is clear that the condition $\phi(x,0,0) = 0$ [(4.17)] and (4.4) are discontinuous at the intersection if $U(0) \neq 0$. Similarly, the condition $\eta(x,0) = 0$ or $\phi_t(x,0,0) = 0$ is discontinuous with $dU/dt(0) \neq 0$ at the intersection. If this discontinuity is to be removed the wave maker must be prescribed to start with a gradual acceleration from zero (a condition stronger than $p > 1$ as concluded by Roberts, 1987). In fact, one also finds in Roberts (1987) that the solution to the wave maker problem is analytically smooth if the wave maker starts with the velocity

$$U(t) = \alpha \exp(st), \ s > 0 \tag{4.22}$$

with t starting from $-\infty$. Thus, one may conclude that the transient wave maker problem does not have singular behavior if the wave maker starts smoothly from rest with an

initially still free surface. On the other hand, for jump to finite velocity (or even acceleration) of the wave maker the potential theory may predict nonanalytical behavior. From the physical point, viscosity and surface tension may have a stabilizing effect if the motion tends to develop fast oscillations as predicted by the analysis of Roberts. Secondly, the force transmission being over finite time, no matter how small, for a physically realistic system any real wave maker will start with a zero acceleration. A close physical example to the canonical impulsive motion (jump to finite velocity, infinite acceleration at the initial time) is the wave maker driven by a sledge hammer. In an experimental study of such a motion (Greenhow and Lin, 1983) photographs show that the surface elevation agrees well with the linear potential theory away from the wave maker. However, a thin water jet is formed after the start at the intersection of the free surface and the wave maker.

4.3 Computational Procedure for Wave Generation

In the present work, wave generation is studied in the presence of either a radiation boundary or a vertical reflecting boundary (all numerical examples presented here have the wave generation boundary at the left end and the radiation or the reflecting wall at the right end of the computational domain). A reflection boundary is implemented by specifying the normal flux ϕ_n (for $\nabla^2\phi = 0$) and ϕ_{tn} (for $\nabla^2\phi_t = 0$) to be zero. The position of this lateral boundary is stationary during the temporal evolution. Treatment of the radiation boundary is described in chapter 5. The two important aspects of a wave generating boundary are:

- Relocation of the nodes on the generating boundary itself and the intersecting sides (the free surface and the bottom) as temporal evolution takes place.

- Specification of the boundary conditions, the normal flux ϕ_n (for $\nabla^2\phi = 0$) and ϕ_{tn} (for $\nabla^2\phi_t = 0$), at the current position at each time step.

If a rigid wave maker is simulated, the lateral boundary follows the motion of the wave maker. The free surface node at the intersection (node $I1$ in fig. 4.1) is free to move tangentially along the wave maker, but should have the same velocity normal to the wave maker as the wave maker itself. As described in chapter 3, the node $I1$ is moved to its

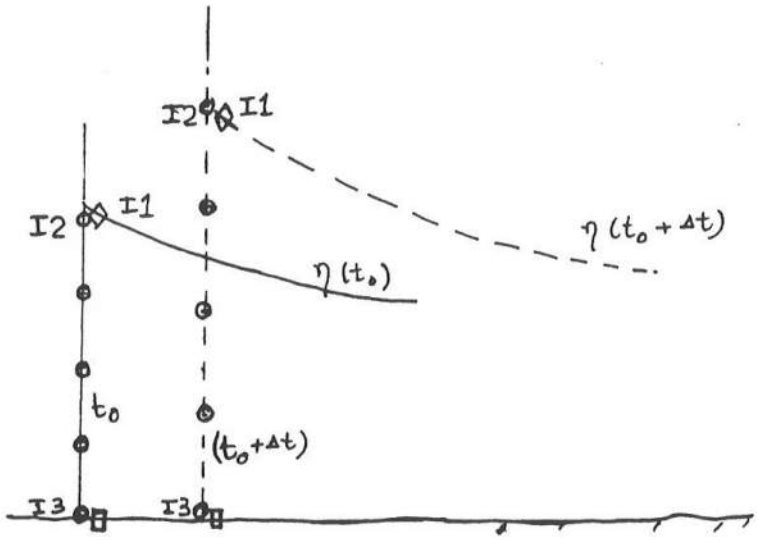

Figure 4.1: Relocation of the nodes due to a moving lateral boundary. The free surface change is exaggerated for clarity.

projection on the wave maker from its computed position through the free surface updating after each time step. As to the nodes on the lateral boundary, their relative positions along the wave maker need to be modified due to the change in the surface elevation. The nodes $I2$ and $I3$ (fig. 4.1) are moved to the new intersection points with the free surface and the bottom respectively. The intermediate nodes are distributed uniformly along the wave maker. Similarly, the nodes on the bottom are relocated at equal intervals between the new position of the wave maker and the right lateral boundary of the domain.

For a prescribed displacement $\mathbf{x}(t)$ of the wave maker ϕ_n on the lateral boundary is given by the kinematic condition

$$\phi_n = \frac{d\mathbf{x}}{dt} \cdot \mathbf{n} \tag{4.23}$$

where $\mathbf{n}$ is the normal vector to the wave maker pointing out of the fluid domain. In obtaining a formulation for ϕ_{tn}, careful consideration is necessary since ϕ_{tn} is different from the the acceleration of the wave maker (or the Lagrangian acceleration of a fluid particle on the wave maker). In fact, ϕ_{tn} is related to the Lagrangian acceleration through the flow quantities. For a plane, rigid body of translation α and rotation θ, this relation

is established to be (Cointe, 1989 and Grilli & Svendsen, 1990)

$$\phi_{tn} = \ddot{\alpha} \cdot \mathbf{n} + \dot{\theta}[(\ddot{\alpha} \cdot \mathbf{s}) - \phi_s] - \phi_{ns}(\ddot{\alpha} \cdot \mathbf{s}) + \phi_{ss}(\dot{\alpha} \cdot \mathbf{n}) \tag{4.24}$$

where $\ddot{\alpha}$ is the translational acceleration and $\dot{\theta}$ is the rotational velocity. For a piston wave maker [$\dot{\theta} = 0$ and $\mathbf{n} = (-1, 0)$] with a translational velocity of $\dot{\alpha} = (U, 0)$, (4.23) and (4.24) are respectively simplified to

$$\phi_n = -U, \tag{4.25}$$

$$\phi_{tn} = -\frac{dU}{dt} - U\frac{\partial^2 \phi}{\partial^2 s}. \tag{4.26}$$

ϕ_{ss} in (4.26) is computed from the discrete values of ϕ at the nodes of the generation boundary. ϕ is not known on the wave maker prior to the solution of $\nabla^2 \phi = 0$, but is a result of the boundary integral solution with ϕ_n specified as the boundary condition.

4.4 Generation of Solitary Waves and Initial Singularity

Goring (1978) showed that a solitary wave of small height can be generated in a wave tank without appreciable dispersive tails by moving the wave maker in a way that corresponds to the form of a steady solitary wave given by the Boussinesq theory. According to Goring's formulation the piston displacement ξ to generate a wave of height H over a depth of h is given by

$$\xi(t) = \frac{H}{h\kappa}[\tanh \kappa(ct - (\xi + \lambda)) - \tanh(-\kappa\lambda)] \tag{4.27}$$

where the wave number κ and the phase velocity c are $\sqrt{3H/(4h^3)}$ and $\sqrt{g(h+H)}$ respectively. λ is a free parameter having the dimension of length. The significance of this parameter is discussed shortly. The corresponding expressions for the velocity and the acceleration of the piston are

$$\frac{d\xi}{dt} = \frac{cH \operatorname{sech}^2 \kappa(ct - (\xi + \lambda))}{h + H \operatorname{sech}^2 \kappa(ct - (\xi + \lambda))} \tag{4.28}$$

$$\frac{d^2\xi}{dt^2} = (\frac{d\xi}{dt} - c)\frac{2cHh\kappa \operatorname{sech}^2 \kappa(ct - (\xi + \lambda)) \tanh \kappa(ct - (\xi + \lambda))}{(h + H \operatorname{sech}^2 \kappa(ct - (\xi + \lambda)))^2} \tag{4.29}$$

These expressions have been used by Kim *et al.* (1983) and Grilli & Svendsen (1989, 1990) in the boundary integral models to simulate generation of solitary wave by a moving piston.

The initial displacement ξ of the wave maker is set at zero at time $t = 0$ satisfying (4.27). The velocity and the acceleration of the piston have, however, nonzero values depending on the parameter λ. The starting velocity and acceleration tend to zero as $\lambda \to \infty$. The wave maker would then take infinitely long time to reach its maximum velocity. In practice, a smaller value of λ is used with the starting velocity and acceleration of the wave maker being only small fractions of their maximum values.

Fig. 4.2 shows an example of a solitary wave of height $0.4h$ computed using the motion of the piston prescribed by (4.27). To define the initial conditions for the computation, we have used $\lambda = 3.8/\kappa$ and the free surface in front of the wave maker is specified to be still; *i.e.*, $\eta(x, t = 0) = 0$ and $\phi(x, z = 0, t = 0) = 0$. The figure shows large oscillations

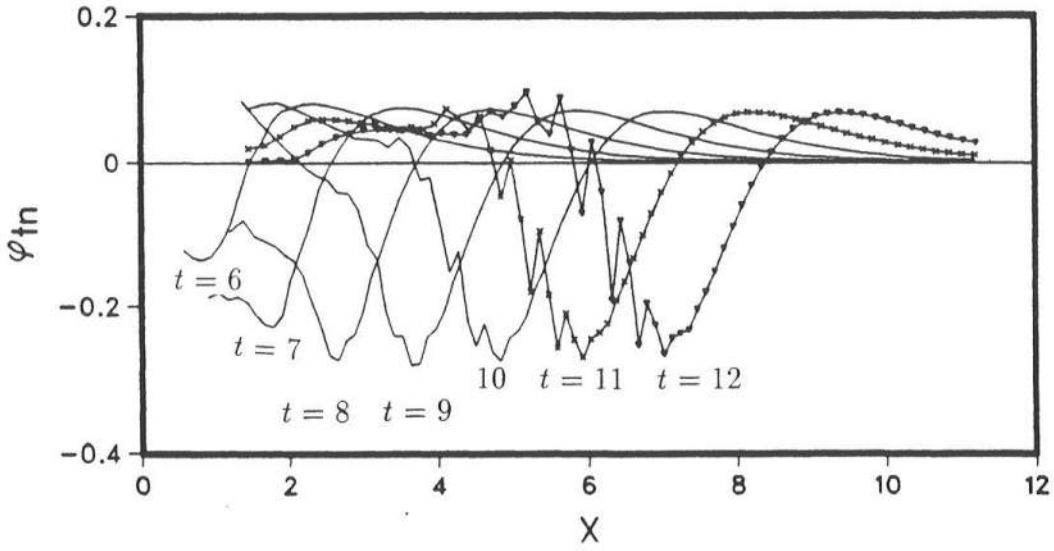

Figure 4.2: Computed ϕ_{tn} on the free surface at different stages of the propagation. The crest of the solitary wave is where ϕ_{tn} has the largest negative value. Quasi-spline elements are used on the free surface. $\Delta x = 0.175$; $\Delta t = 0.1$; $\lambda = 3.8/\kappa$. $\eta(x, t = 0) = \phi(x, z = 0, t = 0) = 0$.

in the computed ϕ_{tn} which quickly leads to instabilities. Noticeable fluctuations are not observed in the computed elevation η or potential ϕ at these times. This is the reason why ϕ_{tn} is shown instead of the other quantities. The oscillations depend on the height of

the wave generated and the discretizations used. The important point is that the initial conditions specified for this computation cause the oscillations observed in the figure. The reason for this is the following.

According to (4.28) and (4.29), the velocity and the acceleration of the piston at the initial time are $0.002\,cH/h$ and $0.004\,c^2\kappa H/h$ respectively. Clearly, these conditions are in conflict with the specified free surface condition at the initial time. In fact, these initial conditions correspond to the case of a wave maker whose motion jumps to a finite velocity: a motion which, according to the analysis of Roberts (1987), leads to fast oscillations of the free surface. Even though the starting velocity and acceleration of the wave maker for $H = 0.4h$ and $\lambda = 3.8/\kappa$ are small, the example indicates the sensitive nature of the problem even to a mild singularity imposed through the initial specifications.

To show that the oscillations observed in fig. 4.2 are indeed caused by the conflicting initial conditions, we carry out the computation with an increased λ resulting in a smaller velocity of the piston at the initial time. Fig. 4.3 shows the computed ϕ_{tn} on the free surface for $\lambda = 5.8/\kappa$. All other parameters are kept the same as those in the computation shown in fig. 4.2. Due to the larger λ used in this computation, longer time is necessary for the solitary wave to reach the same stage of the propagation as shown in fig. 4.2. Comparison of fig. 4.3 with fig. 4.2 shows noticeable improvement in the behavior of the computed ϕ_{tn} on the free surface.

We now consider an alternate approach to remove the singularity in the initial specification. In this approach, the discrepancy at the intersection is reduced by modifying the previous specification of still water conditions. For a wave maker starting with zero velocity and zero acceleration ($\lambda \to \infty$) with a flat free surface in front of it, there will be a pile-up of mass above the still water level at any instant after the initiation as the wave maker attains higher velocity. Thus, if the computation is started with a finite velocity and acceleration of the wave maker, the specified free surface conditions at the initial time must correspond to the undulation which is expected to exist at that velocity and acceleration of the piston. In order to do this, the free surface elevation and the potential

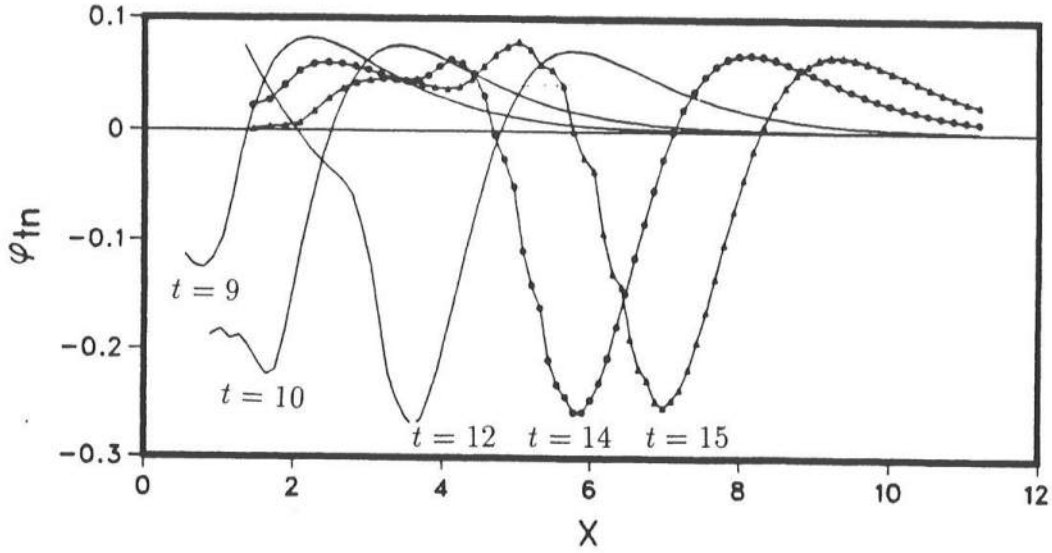

Figure 4.3: Computed ϕ_{tn} on the free surface. $\lambda = 5.8/\kappa$. All other parmeters are same as those used in the computation shown in fig. 4.2. Due to the larger λ used, the solitary wave takes longer time to reach the same stage of propagation as in fig. 4.2.

are assumed in an exponential form as follows.

$$\eta(x, t = 0) = A \exp(-2\kappa x), \tag{4.30}$$

$$\phi(x, t = 0) = B \exp(-2\kappa x) \tag{4.31}$$

where κ is once again defined to be $\sqrt{3H/(4h^3)}$. The coefficients A and B are found by satisfying the boundary condition at the wave maker:

$$\frac{\partial \phi}{\partial x}(x = 0, t = 0) = -2\kappa B = \frac{d\xi}{dt}(t = 0), \tag{4.32}$$

$$\frac{\partial^2 \phi}{\partial t \partial x}(x = 0, t = 0) = -\frac{1}{g}\frac{\partial \eta}{\partial x}(x = 0, t = 0) = 2\frac{\kappa}{g}A = \frac{d^2\xi}{dt^2}(t = 0). \tag{4.33}$$

Equations 4.32 and 4.33 are based on the linearized free surface conditions which are valid only for small undulations at the initial time.

Fig. 4.4 shows the computed ϕ_{tn} for the same case as in fig. 4.2 with the difference that the initial free surface variables η and ϕ are specified according to (4.30) and (4.31).

Comparison of fig. 4.4 with fig. 4.2 shows again that the oscillations in the behavior of ϕ_{tn}

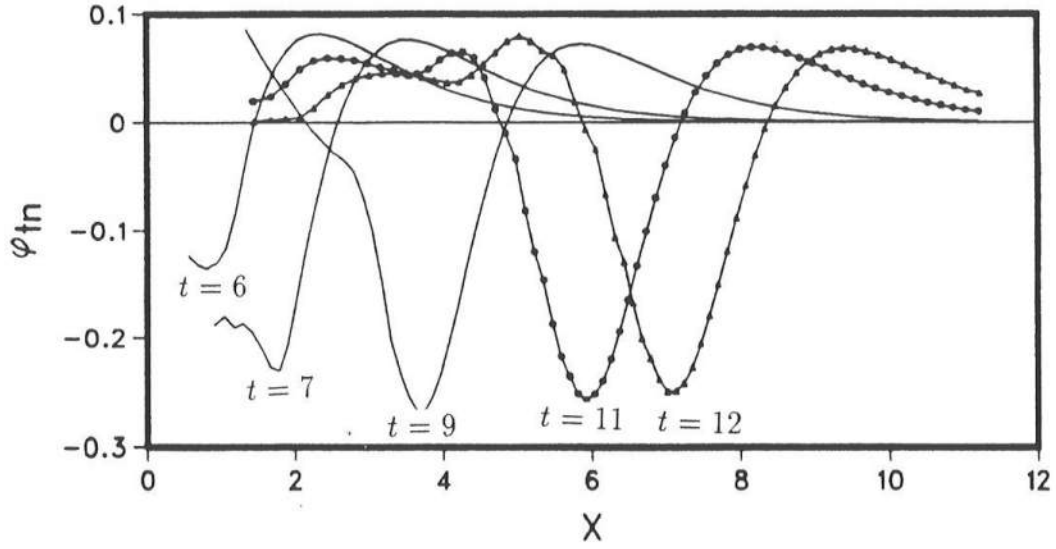

Figure 4.4: Computed ϕ_{tn} on the free surface. Initial η and ϕ are specified according to (4.30) and (4.31). All other parameters are the same as in fig. 4.2.

can be significantly reduced by removing the singularity in the specification of the initial conditions.

With the fast oscillations in the computed ϕ_{tn} nearly removed in fig. 4.4, attention is given to the smooth undulations to the left of the crest (position of the largest negative value of ϕ_{tn}). These are the results of the imperfect motion of the wave maker. First, the motion governed by the Boussinesq theory becomes deficient as higher waves are considered. Secondly, variation of the fluid velocity under a high solitary wave is significantly different from the uniform variation of the fluid velocity imposed by the piston wave maker across the depth.

4.5 Numerical Instabilities in the Generation of Oscillatory Waves

In many numerical studies of wave generation using boundary integral method, free surface instabilities have been reported (see, for example, Dommermuth *et al.*, 1988). The causes for the instabilities have sometimes been linked to singularities at the intersection

of the free surface and the wave maker (see Cointe, 1988). Though this is certainly a factor, numerical artifacts can also add to the instabilities. In the following we discuss the possible factors leading to the instabilities in the generation of oscillatory waves.

- It has been discussed and shown in chapter 3 how improper treatment of the intersection can cause errors and nonconvergence in the solution of a boundary integral method based on Green's theorem. It has also been shown that these disadvantages can be removed by careful numerical treatment of the intersections in the computational model.

- Numerical experiments during the generation of solitary waves described earlier in this chapter show how even small discrepancies at the intersection (or mild singularity) in the specified initial conditions can influence the results. Cointe (1988) has considered modeling the singular behavior by using the linear analytical solution near the wave maker. Though the linear solution can be used as indicative of the singular behavior, one must bear in mind that the solution becomes self-inconsistent with the linear theory. Thus, the linear solution should not be used as the replacement for the exact solution in the analysis of the nonlinear motion. On the other hand, in the procedure presented here the motion of the generation boundary is modeled so that the initial singularity is removed.

  Consider, for simplicity, wave generation by a rigid piston. If the dispacement $\xi(t)$ of the wave maker is prescribed to be

$$\xi(t) = A\sin(\omega t + \theta) \tag{4.34}$$

  as in Lin *et al.* (1984) or Cointe (1988) where A is the amplitude of the stroke and ω is the angular frequency, the wave maker starts with the initial velocity and acceleration given respectively by

$$U(0) = A\omega\cos(\theta), \quad \frac{dU}{dt}(0) = -A\omega^2\sin(\theta). \tag{4.35}$$

If the phase angle θ is assumed to be $\pi/2$, $U(0)$ is zero but the acceleration jumps to a finite value. To ensure a smooth start of the wave maker, we introduce a start-up function $S(t)$ such that

$$S(0) = 0,\ S(t)\rightarrow 1 \text{ for large } t, \tag{4.36}$$

$$\dot{S}(0) = \ddot{S}(0) = 0 \tag{4.37}$$

where $\dot{S}$ and $\ddot{S}$ denote the first and second time derivatives. The wave maker displacement $\xi(t)$ is now modeled as

$$\xi(t) = S(t)A_i \sin(\omega_i t + \theta_i) \tag{4.38}$$

An ideal function for $S(t)$ is given by

$$S(t) = \frac{\tanh(bt/T - \lambda) + \tanh\lambda}{1 + \tanh\lambda} \tag{4.39}$$

where T is a typical time scale (say equal to the wave period for a monochromatic signal) and b and λ are two constants. Equation 4.37 is strictly satisfied as $\lambda\rightarrow\infty$. In practice, only a finite value of λ will be chosen, but should be such that the initial velocity and acceleration are small enough not to create undesirable oscillations. The parameter b can be increased or decreased to speed up or slow down the start-up.

Figs. 4.5 and 4.6 show the significance of the parameter b. Amplitude of the wave maker stroke A and the angular frequency ω are chosen to be the same as in fig. 10 of Lin *et al.* (1984). For the larger b, the surface elevation shows small scale oscillations at the crest (fig. 4.5). The undesirable oscillations are more noticeable in the plot of ϕ_{tn} in fig. 4.6. The instabilities may be suppressed if smoothing is used. However, we show by considering a slower acceleration of the wave maker ($b = 3$) that the small scale oscillations disappear though the wave form is more or less similar to that obtained by using $b = 9$. In real fluid viscosity may play a role in smoothing out the small scale variations, but the examples strongly indicate that fast acceleration of the wave maker can also lead to instabilities.

- During the generation of oscillatory waves, the angle between the tangent to the free surface and the wave maker changes with time. If the magnitude of the tangential

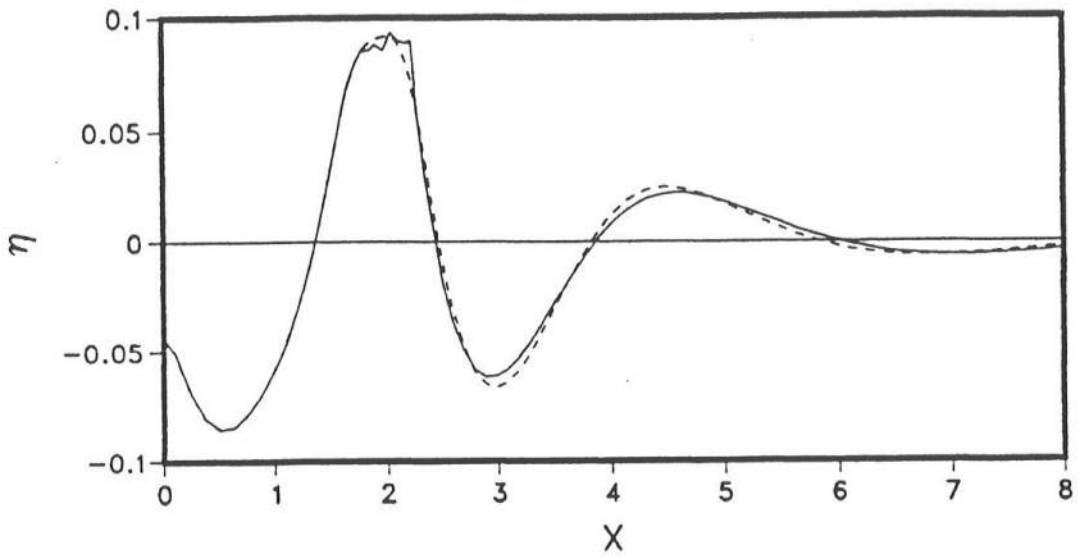

Figure 4.5: η at the same stage of propagation; solid line ($b = 9,\ \lambda = 4.0$), dotted line ($b = 3,\ \lambda = 4.0$). $A = 0.1, \omega = \pi/2$. The solid line shows η at $t = 12$ and the dotted line at $t = 16$.

velocity ϕ_{s_1} on the free surface and the normal velocity ϕ_{n_2} (fig. 4.7) are not equal at the instant the angle is $\pi/2$ a singularity is imposed. For a vertical wave generation boundary the angle between the tangent to the free surface and the wave maker becomes $\pi/2$ each time a local crest or trough appears. It has been discussed in chapter 3 how the magnitudes of ϕ_{s_1} and ϕ_{n_2} can be different at these instants during the temporal evolution of the free surface. For the computed results shown in fig. 3.8, the motion of the wave maker is prescribed according to (4.38). Computations with larger λ or smaller b do not show any improvement indicating that the oscillations observed in that figure are not caused by the start-up of the generation from the still water condition. On the other hand, these oscillations could be significantly reduced by using the 'BC-correction' procedure. This indicates that the spurious oscillations are caused by the conflicting boundary conditions at the intersection which may arise in the computations during the temporal evolution.

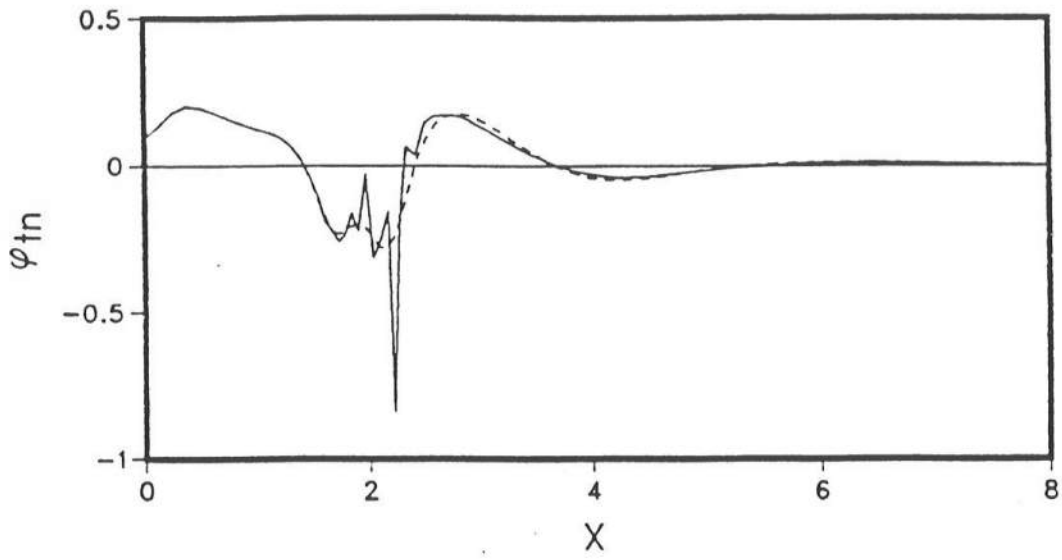

Figure 4.6: ϕ_{tn} on the free surface at the same stage of propagation; solid line ($b = 9,\ \lambda = 4.0$), dotted line ($b = 3,\ \lambda = 4.0$). $A = 0.1, \omega = \pi/2$. The solid line shows ϕ_{tn} at $t = 12$ and the dotted line at $t = 16$.

4.6 Generation of Waves Through Velocity Specification

A 'realistic wave field' is difficult to achieve through the motion of a rigid wave maker because such a wave generation also generates 'free' or 'spurious' components (see the review by Svendsen, 1985). This disadvantage may be removed in a numerical model, since arbitrary variation of velocity can be specified on a lateral boundary. Although this is computationally simple, at least in principle, the problem of modeling input for nonlinear waves is far more complex. Leaving aside the difficulties associated with quantifying a nonlinear wave field in the presence of reflection, there is no clear scheme to design velocity variation at a lateral boundary to achieve an observed time series of the surface elevation at a given point even in a unidirectional wave field. To the knowledge of the author, such a procedure in a boundary integral model has not been reported yet. In the present work, we limit the procedure to the generation of waves of permanent form starting from the still water condition.

A steadily propagating train of waves can be considered stationary if seen from a

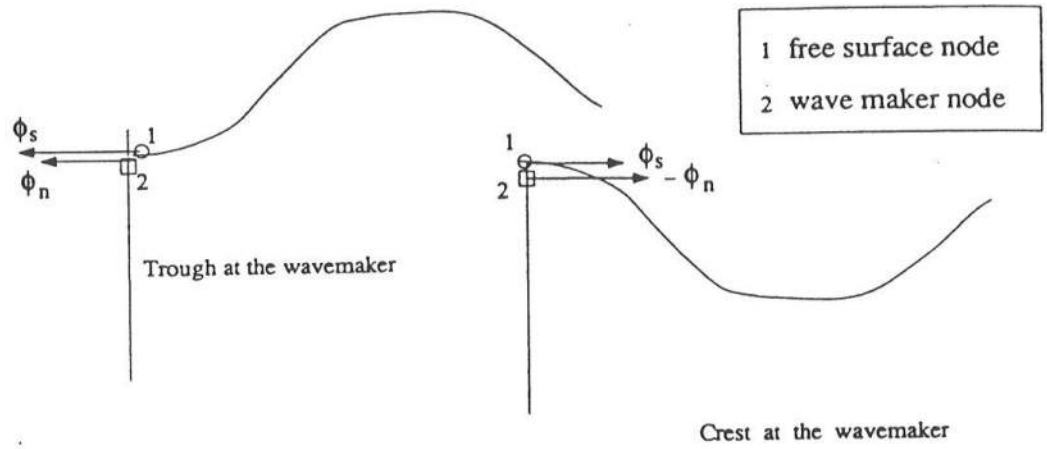

Figure 4.7: Conflicting conditions occur at the intersection at the instant a local crest or trough appears at a vertical generation boundary if the magnitudes of ϕ_s at 1 and ϕ_n at 2 are unequal.

reference frame moving with the phase velocity c. The velocity field under this stationary form can be obtained from the Stream Function theory of Rienecker & Fenton (1981). One can however easily express the velocity with respect to the stationary reference frame using the coefficients B_j's obtained from the theory. For a train of steady waves propagating over a depth of h with the phase velocity of c one has for the horizontal velocity $u^{sf}(x,z,t)$

$$u^{sf}(x,z,t) = \sum_{j=1}^{N} (jk)\, B_j \frac{\cosh jk(h+z)}{\cosh jkD} \cos jk(x-ct) \tag{4.40}$$

where the coefficients B_j's depend on the choice of D. The term $\cosh jkD$ is introduced in (4.40) to ensure the convergence of the series (see Rienecker & Fenton (1981) for a discussion on the choice of D). We have used a unit value of D for the computations presented here.

In the boundary integral computation, we assume the generation boundary to be vertical like a piston wave maker. However, the horizontal velocity U on the generation boundary is prescribed to be

$$U(\xi,z,t) = S(t)u^{sf}(\xi,z,t) \tag{4.41}$$

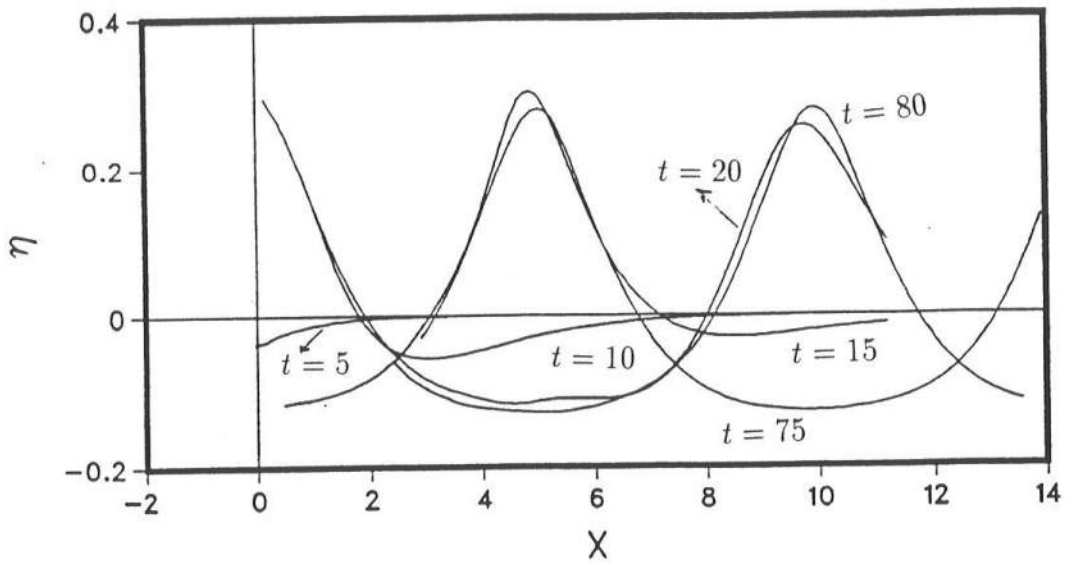

Figure 4.8: Transient generation of an unmodulated wave field through (4.41). The initial position of the generation boundary is at $x = 0$ [$\xi(0) = 0$]. The normalized height and period of the steady waves are 0.4 and 10 respectively.

where $\xi(t)$ is the x-coordinate of the generation boundary. $u^{sf}(\xi, z, t)$ is given by (4.40) and $S(t)$, given by (4.39), is multiplied to $u^{sf}(\xi, z, t)$ to ensure that the velocity $U(\xi, z, t)$ starts smoothly from zero. This is necessary to avoid the initial singularity at the intersection with a still free surface. The horizontal displacement $\xi(t)$ of the generation boundary is same as the horizontal displacement of the free surface node at the intersection which is computed from the updating procedure for the free surface. With time increasing, the specified velocity at the generation boundary approaches that under the stream function wave and the initially transient field evolves to a steady state if no reflection is present in the computational domain.

Surface elevations computed from the boundary integral model using (4.41) are shown in fig. 4.8 for a wave of height $H = 0.4h$ and $T = 10\sqrt{h/g}$. A radiation boundary described in chapter 5 forms the right lateral boundary for this computation. Nodes on the free surface are initially uniformly distributed with a spacing of $\Delta x = 0.175h$ and quasi-spline elements are used for the discretization. A time step of $\Delta t = 0.052\sqrt{h/g}$ has

been used in the computation. Table (4.1) shows the harmonics of the surface elevation at several locations. The harmonics are computed from the time series recorded at the respective locations after the wave field becomes steady. It can be easily seen that the

Table 4.1: Values of the first nine harmonics according to the Stream Function theory and the computed results. The computed results are obtained from Fourier analysis of the time records of the surface elevation at the respective locations during the 8th wave period after the transient start.

j	stream function	computed results		
		x/h=4.2	x/h=6	x/h=8.4
1	0.1728008990	0.1723554730	0.1711650490	0.1715103390
2	0.0686091185	0.0687872171	0.0680692196	0.0685715079
3	0.0247484073	0.0253041763	0.0257703178	0.0253391713
4	0.0093022734	0.0088652596	0.0102853999	0.0097292326
5	0.0037392378	0.0039088689	0.0041867122	0.0039189234
6	0.0015934634	0.0015381004	0.0019772022	0.0016338350
7	0.0007094676	0.0007612444	0.0008799590	0.0007010209
8	0.0003262556	0.0003306544	0.0004390327	0.0002578150
9	0.0001537243	0.0001545730	0.0002031644	0.0001799094

the computed results (after seven wave periods) agree with the stream function theory to within a very small percent. The accuracy of the BEM computations can be improved by decreasing Δx and Δt, but this is not considered necessary here for improving the comparison of the magnitudes of the harmonics with that given by the Stream Function theory.

4.7 Modulation of Waves Generated by a Rigid Wave Maker

Waves of finite amplitude generated by a rigid wave maker undergo spatial modulation. Modulation of the harmonics is caused by an imperfect motion of the wave maker and an imposed depth variation of velocity which is different from that under a uniform wave field. Whereas the depth variation of the imposed velocity depends only on the particular type of the wave maker used and can not be controlled in a physical wave tank, the motion of the wave maker can certainly be regulated. In the following, boundary integral analysis of the spatial modulation of the wave field generated by a rigid wave maker is presented. First, the simple harmonic motion of a piston wave maker is considered. Next,

we develop a modified motion with a view to generating an unmodulated field by a piston wave maker.

Since the assumed free surface conditions at the initial time correspond to the still water state, the wave field is allowed to develop to a steady state before analyzing the spatial modulation. A radiation condition (described in chapter 5) is used on the right lateral boundary to allow the generated waves to be transmitted through. The performance of the radiation boundary is found to be satisfactory with no noticeable reflection. Since the free surface nonlinearity and the condition at the wave maker are accounted for in an exact way in the present model, the analysis can be used to study modulation of large waves and arbitrary motion of the wave maker.

4.7.1 Harmonic Wave Maker

The second order wave field due to a harmonic wave maker has been analyzed by several authors (Madsen, 1971; Svendsen & Hansen, 1974 and Flick & Guza, 1980). One may write the second order propagating modes of the surface elevation η_2 due to a wave maker oscillating sinusoidally with an angular frequency of ω in the form

$$\eta_2 = A_{2s}\cos(2kx - 2\omega t) + A_{2f}\cos(\mu x - 2\omega t + \psi) \tag{4.42}$$

where A_{2s} and A_{2f} denote the amplitudes of the second order bound and free harmonic respectively. The Stokes wave number k satisfies the dispersion relation

$$\omega^2 = gk\tanh kh \tag{4.43}$$

and the wave number μ of the second order free harmonic is given by

$$4\omega^2 = g\mu\tanh\mu h. \tag{4.44}$$

It follows from (4.42) that the spatial modulation of the second order amplitude A_2 is

$$A_2(x) = \sqrt{A_{2s}^2 + A_{2f}^2 + 2A_{2s}A_{2f}\cos[(2k-\mu)x - \psi]} \tag{4.45}$$

For a given wave period, water depth and stroke of the wave maker, the amplitudes A_{2s}, A_{2f} and the phase ψ can be easily calculated from the equations described in Flick & Guza (1980).

Fig. (4.9) shows the computed second harmonics using the boundary integral model and that from the analytical prediction given by (4.45) for two different wave heights. The

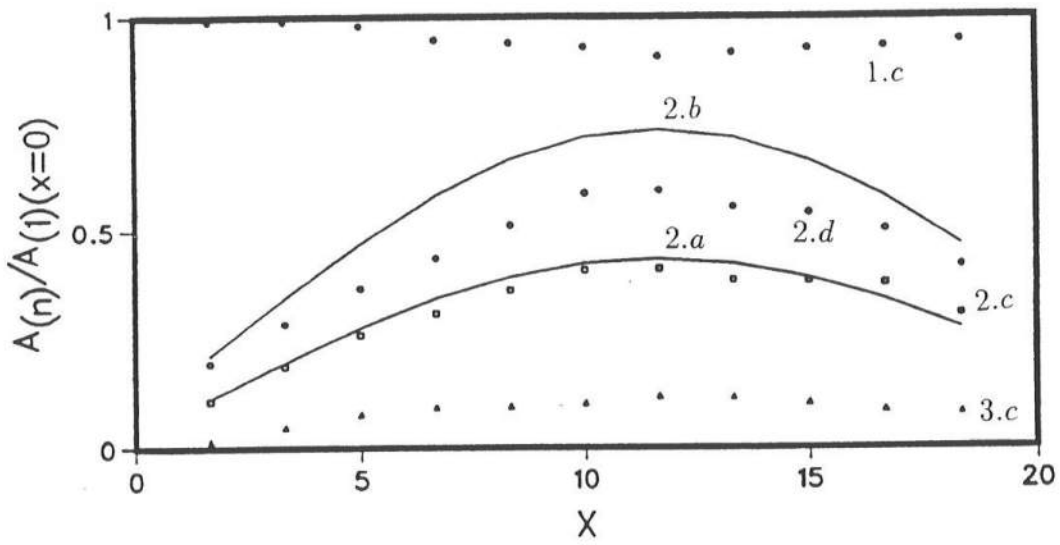

Figure 4.9: Spatial modulation of the harmonics due to the sinusoidal motion of a piston wave maker. Second order amplitudes predicted by (4.45) are shown by solid line 2.a for $A_1(x \approx 0) = 0.1$ and by solid line 2.b for $A_1(x \approx 0) = 0.175$. $A_1(x \approx 0)$ is the nondimensional first order amplitude close to the wave maker. Period T is 10.752 for both the waves with the Ursell parameter Ur= 20 and 35. Computed results are shown by the discrete points. Computed modulation of the first harmonic is shown by 1.c, second harmonic by 2.c and third harmonic by 3.c for $A_1(x \approx 0) = 0.1$. 2.d shows the computed modulation of the second order amplitude for $A_1(x \approx 0) = 0.175$.

second order theory agrees well with the computed results of the second order amplitude for the smaller waves. There is a corresponding modulation of the first harmonic and the harmonic at each higher order (Boczar-Karakiewicz, 1972), though the amplitude of the first order propagating mode is is assumed to be constant in the second order theory. Computed modulations of the first order and third order harmonics are shown in fig. 4.9. For the larger waves (Ur=35), the second order amplitude is overpredicted by the theory.

4.7.2 Periodic Waves of Permanent Form by a Piston Wave Maker

Fig. 4.9 shows the strong modulation of the wave field if the wave maker moves in a sinusoidal manner. One way to reduce the modulation and attain a less non-uniform wave field is to consider modifications of the simple harmonic oscillation of the piston wave maker. An exact expression for the depth averaged horizontal velocity $u_{\rm av}$ under a wave of permanent form is given by (Svendsen & Staub, 1981)

$$u_{\rm av} = \frac{c\eta^{\rm pm}}{h + \eta^{\rm pm}} \tag{4.46}$$

where $\eta^{\rm pm}$ denotes the surface elevation due to waves of permanent form with phase velocity c propagating over a depth of h. Expression (4.46) is valid if $\eta^{\rm pm}$ is measured from the mean water level and the net volume flux in the flow is zero. We now develop a modified motion of the wave maker based on (4.46).

In order to make the procedure applicable over a wide range of wave conditions, the surface elevation $\eta^{\rm pm}$ in (4.46) is obtained from the Stream Function theory which satisfies the nonlinear free surface conditions completely and is valid over a wide range from shallow to deep water. Using a Fourier series, $\eta^{\rm pm}$ is expressed in a convenient form as

$$\eta^{\rm pm}(x,t) = \sum_{j=1}^{N} P_j \cos jk(x - ct) \tag{4.47}$$

where P_j's, k and c are obtained from Rienecker and Fenton's surface profile. With $\eta^{\rm pm}$ specified by (4.47), the wave maker velocity $U(\xi,t)$ is prescribed to be

$$U(t) = S(t)\frac{c\eta^{\rm pm}(\xi,t)}{h + \eta^{\rm pm}(\xi,t)} \tag{4.48}$$

where ξ is the displacement of the wave maker. The function $S(t)$, given by (4.39), is introduced in (4.48) to ensure a smooth start form the initially still free surface. The acceleration of the piston follows directly from (4.48) by differentiation, *i.e.*,

$$\frac{dU}{dt} = \dot{S}(t)\frac{c\eta^{\rm pm}(\xi,t)}{h + \eta^{\rm pm}(\xi,t)} + S(t)\frac{ch}{[h + \eta^{\rm pm}(\xi,t)]^2}\frac{d\eta^{\rm pm}}{dt}. \tag{4.49}$$

By using (4.47), $d\eta^{\rm pm}/dt$ on the wave maker in (4.49) is given by

$$\frac{d\eta^{\rm pm}}{dt} = [c - U(t)]\sum_{j=1}^{N}(jk)P_j \sin jk(\xi - ct). \tag{4.50}$$

The wave maker position $\xi(t)$ can be found by integrating the velocity $U(t)$ given by (4.48). Since the expression contains ξ on the right hand side, an analytical integration in closed form does not seem straightforward. Consequently, $\xi(t)$ is found through a numerical scheme based on the Taylor's expansion

$$\xi(t + \Delta t) = \xi(t) + \Delta t\, U(t) + \Delta t^2 \frac{dU}{dt} + O(\Delta t^3) \tag{4.51}$$

where $U(t)$ and $\frac{dU}{dt}$ are given by (4.48) and (4.49) respectively.

Fig. (4.10) shows the spatial variation of the harmonic amplitude of the surface elevation at different orders due to the motion of the piston given by (4.49). The harmonics are computed after the wave field becomes steady. The generated amplitude of

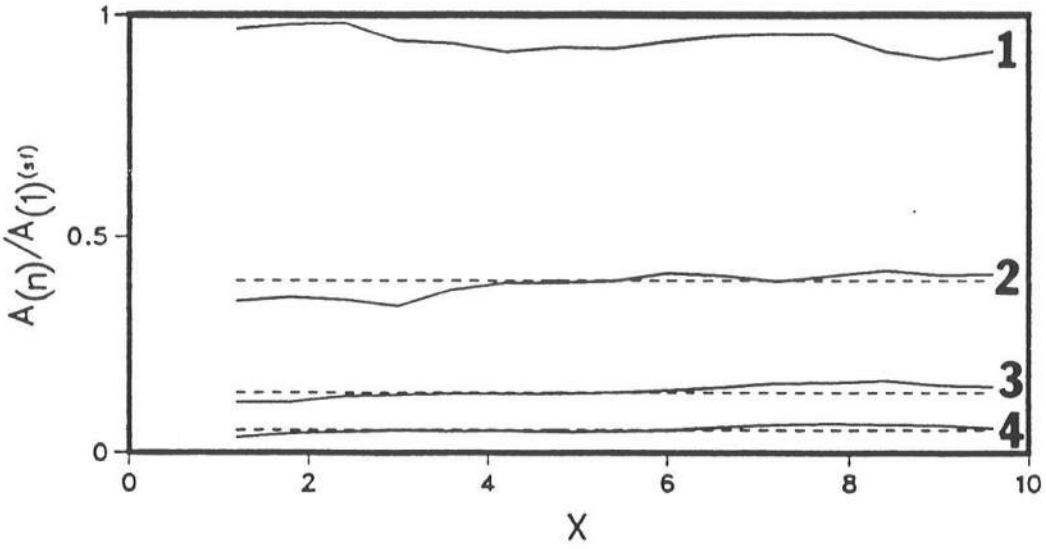

Figure 4.10: Modulation of the amplitudes of the first four harmonics due to a piston moving according to (4.49). $H = 0.4$, $T = 10$, $A_1^{sf} = 0.172$. The computed amplitudes (solid lines) are shown against the uniform stream function values (dotted line).

the first harmonic is somewhat smaller than the target wave. However, the near constant variation of the harmonics and their agreement with the stream function values are encouraging. In particular, comparison of fig. 4.10 with fig. 4.9 emphasizes the effect of the modification of the wave maker motion from the oft-used simple harmonic motion. Thus,

these computations suggest that though the exact permanent form waves may be difficult to generate by a piston wave maker substantial improvement in the regularity of the wave (*i.e.*, reduction in the spurious components) can be achieved simply by specifying the velocity of the piston according to (4.48) and using a high order stream function solution. Further modifications to the motion of the wave maker are possible. The exercise here is not intended to suggest that motion based on the depth averaged velocity is necessarily the optimum one in the sense of creating the wave field with the least deviations from the target permanent form wave. Analysis or formulation for designing the 'optimum motion' has not been pursued further.

4.8 Generation and Propagation of Irregular Waves

Several phenomena are critically associated with the generation and propagation of irregular waves. To begin with, a procedure for generating a desired irregular wave field in a finite computational domain is not clear for nonlinear free surface motion. During propagation nonlinear interaction gives rise to sub and super harmonics creating several scales of wave motion. Additional problems arise if small-scale local breaking or white capping occurs.

To keep things simple and gain a preliminary knowledge of generation of irregular waves we consider here computations with linearized conditions on the free surface and the generation boundary. Though the linearized formulation does not reflect many problems associated with waves of finite amplitude, it reflects partially the problems at the intersection between the free surface and the generation boundary and the scales of motion created by the combination of several components.

4.8.1 Linear Analytical Solution on Uniform Depth

Roberts' solution which was used earlier to gain insight to the initial behavior of the fluid motion cannot be used due to the assumed power law motion of the wave maker. However, the solutions of Kennard (1949) or Lee *et al.* (1990) can be used to express analytically the wave motion generated by arbitrary movement of the wave maker. Here, we follow Lee *et al.* (1990) for its simplicity. The wave maker problem has earlier been

described by (4.1) - (4.4). The solution of Lee *et al.* (1990) uses a Laplace transform in time t and a Fourier transform in x. For a piston located at $x = 0$ and a reflecting wall at $x = L$, Laplace transform of the linearized formulation yields

$$\nabla^2\overline{\phi} = 0,\ [-h \le z \le 0, 0 \le x \le L], \tag{4.52}$$

$$-s^2\overline{\phi} + g\frac{\partial\overline{\phi}}{\partial z} = 0,\ [z = 0], \tag{4.53}$$

$$\frac{\partial\overline{\phi}}{\partial x} = \overline{U},\ [x = 0], \tag{4.54}$$

$$\frac{\partial\overline{\phi}}{\partial x} = 0,\ [x = L], \tag{4.55}$$

$$\frac{\partial\overline{\phi}}{\partial z} = 0,\ [z = -h] \tag{4.56}$$

where the overbar denotes the Laplace transform of the quantity from time t to s. Expression (4.53) is based on the assumption of the free surface being initially still; *i.e.*, $\phi(x,0,0) = \phi_t(x,0,0) = 0$. As the second step, the partial differential system is turned into an ordinary differential equation by a Fourier transform in x. The Fourier pairs are defined by

$$\hat{\overline{\phi}}_n(z,s) = \int_0^L \overline{\phi}(x,z,s)\cos(k_n x)\,dx, \tag{4.57}$$

$$\overline{\phi}(x,z,s) = \frac{\hat{\overline{\phi}}_0(z,s)}{L} + \frac{2}{L}\sum_{n=1}^{n=\infty}\hat{\overline{\phi}}_n(z,s)\cos(k_n x) \tag{4.58}$$

where

$$k_n = n\pi/L. \tag{4.59}$$

The solution to $\hat{\overline{\phi}}_n$ satisfying the conditions at $z = -h$ and $z = 0$ is obtained easily at each n. Finally, the solution in time domain is obtained by the inverse Laplace transform of $\overline{\phi}(x,z,s)$. Surface elevation η follows directly from $\phi(x,z,t)$ through the condition $\eta = -\phi_t/g$. For a piston wave maker of velocity $U(t)$, we have the expressions

$$\phi(x,z,t) = \frac{U(t)}{L}(\frac{z^2}{2} + hz) - \frac{gh}{L}\int_0^t (t-\tau)U(\tau)d\tau - 2\frac{U(t)}{L}\sum_{n=1}^{\infty}\frac{\cos k_n x}{k_n^2}$$
$$-\frac{2}{L}\sum_{n=1}^{\infty}\cos k_n x\frac{\cosh k_n(h+z)}{k_n^2\cosh k_n h}[-U(t) + p_n\int_0^t U(\tau)\sin p_n(t-\tau)d\tau \tag{4.60}$$

$$\eta(x,t) = \frac{h}{L}\int_0^t U(\tau)d\tau + \frac{2}{L}\sum_{n=1}^{\infty}\cos k_n x\frac{\tanh k_n h}{k_n}\int_0^t U(\tau)\cos p_n(t-\tau)d\tau \tag{4.61}$$

where

$$p_n^2 = gk_n \tanh k_n h. \tag{4.62}$$

Two features of the solution are worth noting. First, (4.58) with (4.59) implies that $\phi_x = 0$ at $x = 0$. Hence, the solution (4.60) does not satisfy condition $\phi_x(0, z, t) = U(t)$ in the $(x - z)$ space. The solution is convergent in the L_2-norm and may not be exact close to the wave maker. Secondly, the solution satisfies a reflecting condition at $x = L$. Free propagation over a finite length from the wave maker can be studied by assuming a large value for L. This necessitates taking more terms (larger n) in evaluating ϕ through (4.60) to achieve convergence.

4.8.2 Computational Results, Linear Case

For verification of wave generation against (4.60), the boundary element scheme is modified to be in accordance with the linear wave theory. Thus, the nonlinear terms are eliminated from the free surface updating and the linearized free surface conditions are applied at $z = 0$. Similarly, the wave maker conditions are applied at a fixed position unlike in the exact case where the conditions are applied at the moving position of the wave maker.

We choose here to create the irregular wave field by a combination of 7 components. The wave maker displacement is specified by the expression

$$\xi(t) = S(t) \sum_{i=1}^{7} A_i \sin(\omega_i t + \theta_i) \tag{4.63}$$

with the amplitudes A's, frequencies ω's and phase angles θ's shown in table (4.2). A

Table 4.2: A_i, ω_i, θ_i of the 7 components used to generate the irregular waves in fig. 4.11.

A	0.254	0.092	0.046	0.027	0.021	0.017	0.015
ω	0.628	0.942	1.256	1.571	1.884	2.198	2.512
θ	2.572	5.891	6.266	1.384	0.0	0.0	0.0

reflecting wall is located at $x = 11.2h$. Fig. 4.11 shows the comparison of the computed η with (4.61). 2-node, 3-node (not shown in the figure) and 5-node elements have been

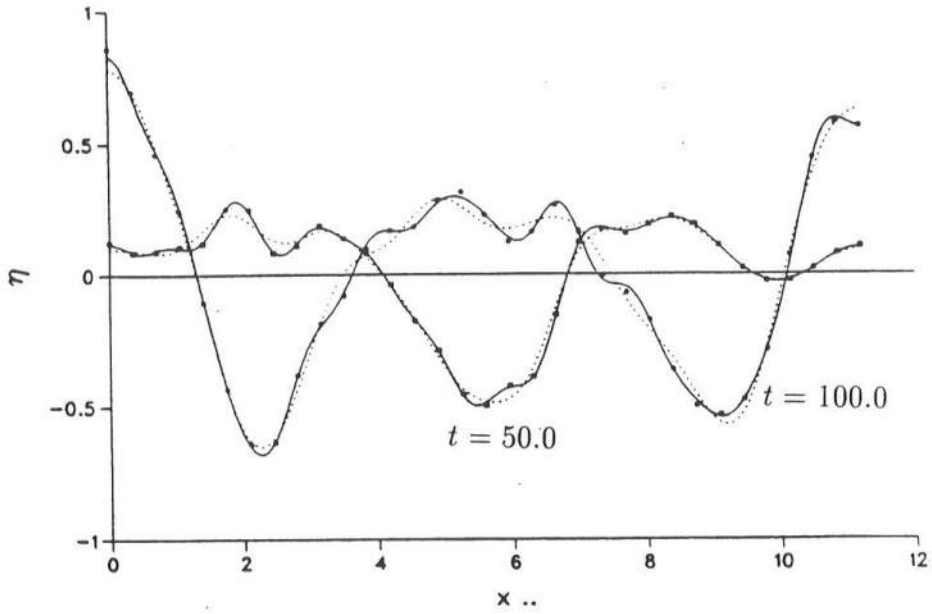

Figure 4.11: Comparison of the computed and analytical prediction of η generated according to (4.63). Analytical results are shown by the discrete solid dots. Computed results are shown by the dotted line [$\Delta x = 0.35$, $\Delta t = 0.1$] and by the solid line [$\Delta x = 0.175$, $\Delta t = 0.05$]. 5-node elements are used for the discretization for both the cases.

used for this computation. Fig. 4.11 shows that even the small scale variations can be produced accurately by reducing Δx from 0.35 to 0.175 while using 5-node elements for the discretization. The convergence to the solution is much slower while using 2-node or 3-node elements. Thus, the example emphasizes the significance of higher order discretization to model free surface motion if small-scale variations are present.

Chapter 5

RADIATION BOUNDARY

5.1 Introduction

Numerical simulation of many wave propagation problems requires an artificial boundary in order to limit the computational domain. Conceptually, the requirement of the artificial boundary is that the outgoing wave is not disturbed by its presence. However, it is often difficult to obtain a mathematical formulation of this statement. In the present chapter we consider several aspects of a radiation boundary for the nonlinear free surface motion. Water wave problems differ from other propagation phenomena (*e.g.*, sound waves or electromagnetic waves) in the sense that while the fluid motion possesses significant vertical structure the propagation is mostly in the horizontal plane. For propagation away form a source of finite size in a three-dimensional domain, amplitude of the surface elevation decreases with distance. Radiation boundary in this case may be based on the simplification that linear wave theory is valid in the far field. This is not true in all cases of two-dimensional propagations (three-dimensional fluid domain) and certainly not when the propagation is largely one-dimensional as in a two-dimensional domain. No exact solution is known for unsteady, nonlinear free surface motion. We discuss in the following an approximate procedure in connection with the boundary integral model and the advantages and disadvantages of the approach.

5.2 Review of the Radiation Conditions

The radiation problem may sometimes be circumvented by assuming periodicity or by choosing a long domain with the condition of boundedness (usually zero flux). Another procedure used sometimes is the one-sided differencing method. The applicability and effectiveness of these type of conditions are very limited. In a well-known work Engquist

& Majda (1977) discuss a procedure of obtaining radiation conditions through the classical wave equation (the symbols used here differ from those in their paper)

$$\frac{\partial^2 \eta}{\partial t^2} = \frac{\partial^2 \eta}{\partial x^2} + \frac{\partial^2 \eta}{\partial y^2}, \quad t, x \geq 0. \tag{5.1}$$

One is interested in this case to specify the radiation condition at $x = 0$. Engquist & Majda (1977) show how a hierarchy of local boundary conditions can be obtained with reduced reflection at each higher order for an incident wave packet containing components at several angles of incidence. For example, from Engquist & Majda (1977) one has for the wave equation (5.1)

$$\text{1st approximation:} \qquad \left(\frac{\partial}{\partial x} - \frac{\partial}{\partial t}\right)\eta = 0, \quad x = 0; \tag{5.2}$$

$$\text{2nd approximation:} \qquad \left(\frac{\partial^2}{\partial x \partial t} - \frac{\partial^2}{\partial t^2} + \frac{1}{2}\frac{\partial^2}{\partial y^2}\right)\eta = 0, \quad x = 0. \tag{5.3}$$

The reflection coefficient R of a component having incidence angle θ is

$$R = \frac{1 - \cos\theta}{1 + \cos\theta} \tag{5.4}$$

if the '1st approximation' is used and

$$R = \left(\frac{1 - \cos\theta}{1 + \cos\theta}\right)^2 \tag{5.5}$$

if the '2nd approximation' is used. We note that while both the approximations yield perfect radiation condition for normal incidence ($\theta = 0$) the second order approximation gives much improved results for waves incident at other angles. Stable approximate radiation conditions for (5.1) up to 4th order have been derived in Engquist & Majda (1977).

The procedure is appealing since one can obtain an almost non-reflecting condition for components over a range of frequencies and angles of incidence in the incident wave packet. This basic idea has been successfully utilized by other authors (*e.g.*, Behrendt, 1985; Kirby, 1989 in the context of the Helmholtz's equation). A detailed account of how the method can be used in engineering applications can also be found in Giles (1988).

There are, however, several drawbacks. As pointed out by Engquist & Majda , naive approximation may lead to unstable condition. Furthermore, there are practical

difficulties in the numerical implementation of the higher order conditions due to the higher order derivatives involved. Most critically, there is sometimes a fundamental problem in extending the procedure to problems governed by other equations. In obtaining the hierarchy of boundary conditions, Engquist & Majda (1977) expressed the wave field as a sum of individual wave components of the form

$$\eta = \hat{a}(\omega, l) \exp\left\{ i \left(\sqrt{\omega^2 - l^2}\, x + \omega t + l y \right) \right\} \tag{5.6}$$

with ω as the angular frequency, l as the wave number in the y direction and $\hat{a}(\omega, l)$ as the associated amplitude. Expression (5.6) represents a train of plane waves traveling left for $\omega \geq 0$ and $\omega^2 - l^2 \geq 0$. The corresponding radiation condition is then given by

$$\left(\frac{d}{dx} - i\omega \sqrt{1 - \frac{l^2}{\omega^2}} \right) \eta = 0, \quad x = 0. \tag{5.7}$$

Condition (5.7) is the starting point of obtaining the generalized condition (5.3).

In fact, the essential problem in one dimensional wave propagation is to derive the equivalent expression of (5.7) valid for unsteady free surface motion (in water wave propagation (5.1) corresponds to only linearized shallow water theory with a nondimensional phase speed of unity). The Sommerfeld condition in its familiar form

$$\frac{\partial \psi}{\partial t} = -C \frac{\partial \psi}{\partial x} \tag{5.8}$$

with C as the phase velocity of a wave quantity ψ (like potential ϕ or elevation η) is strictly valid only in limited cases. Orlanski (1976) considers a modification of the Sommerfeld condition in application to time-dependent geophysical processes. By assuming that a condition of the type (5.8) should be valid near the radiation boundary, Orlanski argued that the derivatives ψ_t and ψ_x at previous time step and adjacent grids can be used to compute the value C in (5.8). Explicitly, Orlanski's condition reads

$$\frac{\partial \psi}{\partial t} = -C^{\psi}(t) \frac{\partial \psi}{\partial x} \tag{5.9}$$

where C^{ψ} for each wave quantity ψ is now computed from the data in the computational domain. Orlanski's condition has been widely used in atmospheric and geophysical models.

Performances of several numerical forms of this approach have been studied in a linear barotropic coastal model by Chapman (1985). Yen and Hall (1981) have used this approach in their study of waves created by a moving object in a finite element model.

An alternative approach to radiation problems is to use damping. The basic ideas behind using damping have been illustrated by Israeli & Orszag (1981). Consider, for example, the one dimensional wave equation

$$\frac{\partial^2 \eta}{\partial t^2} = \frac{\partial^2 \eta}{\partial x^2}, \quad 0 \leq x \leq L. \tag{5.10}$$

where the variables are assumed to be in nondimensional form. In order to simulate a radiation condition through wave damping, the original equation is first modified to introduce damping. A suitable damped system for (5.10) is

$$\frac{\partial^2 \eta}{\partial t^2} = \frac{\partial^2 \eta}{\partial x^2} + \nu(x)\frac{\partial}{\partial x^2}\frac{\partial \eta}{\partial t} - \mu(x)\frac{\partial \eta}{\partial t} \tag{5.11}$$

where $\nu(x)$ and $\mu(x)$ are respectively the viscous damping and 'Newtonian cooling' coefficients. Assuming then that the damping dissipates the energy one can impose the condition

$$\eta(L,t) = 0 \tag{5.12}$$

at the outgoing end of the domain. The benefit of the wave damping concepts is that the radiation condition based on this procedure can be easily formulated for different systems. The two main disadvantages of the procedure concern with the loss of a large portion of the computational domain and the persistence of the ringing modes. For a simple case of $\mu(x) = 0$ and $\nu(x)$ constant, Israeli & Orszag (1981) have shown that the maximum error $\varepsilon(x)$ in the steady oscillatory solution of (5.11) with the condition (5.12) is

$$\varepsilon(x) = \left| \frac{\sin \alpha(L-x)}{\sin \alpha L} - \exp(-i\omega x) \right|, \quad \left(\alpha = \frac{\omega}{\sqrt{1 + i\omega\nu}} \right) \tag{5.13}$$

for an excitation of $\eta_t(0,t) = \sin \omega t$. If ν is chosen such that $\nu\omega >> 1$ the waves are distorted. On the other hand, for $\nu\omega << 1$ and $\nu\omega^2 L >> 1$, the error $\varepsilon(x)$ behaves like

$$\varepsilon(x) \sim 1 - \exp\left(-\frac{1}{2}\nu\omega^2 x\right). \tag{5.14}$$

Israeli and Orszag (1981) show that

$$\frac{x_0}{L} = \frac{2\varepsilon_m}{\ln(1/\varepsilon_m)}, \quad \nu\omega^2 x_0 \sim 2\varepsilon_m \tag{5.15}$$

for a maximum error of ε_m for $[0 \leq x \leq x_0]$. As an example, one has $x_0/L = 1/250$ for $\omega = 1$ and $\varepsilon_m = 0.01$. Thus, this is far from being a satisfactory solution since 99.6

An improvement of the constant viscous damping is obtained by allowing ν to be a function of x (sponge layer). A simple example of a sponge layer is

$$\begin{aligned} \nu(x) &= 0, \quad 0 \leq x \leq x_0, \\ &= \nu_0, \quad x_0 \leq x \leq L \end{aligned} \tag{5.16}$$

where ν_0 is a constant value, sufficiently large to damp out the incoming waves in the region $x_0 \leq x \leq L$. However, such abrupt change in the coefficient also results in strong reflection from $x = x_0$. Thus, the change must be gradual, *i.e*, ν_0 must be a function of x being equal to zero at $x = x_0$. Israeli & Orszag (1981) show that the damping based on Newtonian cooling is more effective over a broad spectrum of waves than that based on viscous damping.

The idea of sponge layers in nonlinear free surface flows has been used by Baker *et al.* (1981) and Cointe (1990) through a modified free surface evolution. In brief, the evolution equations are written as

$$\frac{d}{dt}\mathcal{F} = R - \mu(x)\mathcal{F} \tag{5.17}$$

where $\mathcal{F}$ refers to the surface elevation, the vortex strength or the potential and R is the evolution rate of the corresponding quantity according to the inviscid formulation. $\mu(x)$ has been assumed in the form

$$\begin{aligned} \mu(x) &= 0, \; x < x_0 \\ &= \mu_0(x - x_0)^2, \; x \geq x_0. \end{aligned} \tag{5.18}$$

This formulation has the advantage of being stable, but a large portion of the computational domain is lost. In the example cited by Baker *et al.* (1981) 40% of the computational domain is used for modeling the sponge layer to get "reasonably" close to the exact solution.

5.3 Present Formulation for Free Surface Waves

In the following, a radiation condition for two-dimensional nonlinear free surface motion is considered. Since a large portion of the computational domain is lost while using a sponge layer, this procedure is avoided here. We consider a radiation condition based on (5.8) or its modified form (5.9). The reason behind this is that (5.8) is exactly valid for at least a class of nonlinear waves, that of permanent form, up to the limiting height.

Most models using the Sommerfeld condition have used a finite difference formulation. A typical example is the scheme adopted by Orlanski (1976). Here, the finite difference form of (5.8) is expressed as

$$\frac{\psi(nf,t_0)-\psi(nf,t_0-2\Delta t)}{2\Delta t}=-\frac{C}{\Delta x}\left[\frac{\psi(nf,t_0)+\psi(nf,t_0-2\Delta t)}{2}-\psi(nf-1,t_0-\Delta t)\right] \tag{5.19}$$

where nf denotes the grid of the radiation boundary. $\psi(nf,t_0)$ is then obtained directly from (5.19). The accuracy of the scheme, given by (5.19), is of the order $O(\Delta x)$ and the time step Δt needs to be uniform throughout the duration of the computation. Yen and Hall (1981) have also used a similar finite difference scheme to determine $\phi(t_0)$ at the radiation boundary in their investigation of waves generated by a moving body using a finite element model. They faced instabilities even when generated waves were of small amplitude. They reported filtering and free surface damping in order to suppress the instabilities.

In a boundary integral model, Grilli *et al.* (1988) have considered a direct application of (5.8) at every time step. In this procedure, ϕ_x and ϕ_{tx} are specified as the Neumann conditions on a vertical radiation boundary for the two systems $\nabla^2\phi=0$ and $\nabla^2\phi_t=0$, respectively. It follows from (5.8) for constant C that

$$\frac{\partial^2\phi}{\partial x\partial t}=-C\frac{\partial^2\phi}{\partial x^2}. \tag{5.20}$$

From the continuity equation $\phi_{xx}=-\phi_{zz}$, ϕ_{zz} can be computed on the vertical boundary provided ϕ is known along it. The difficulty is that specification of ϕ_x requires the knowledge of ϕ_t and specification of ϕ_{tx} requires ϕ which are not known prior to the solution. Hence, an iterative procedure has been adopted in Grilli *et al.* (1988). This procedure,

at the very least, requires more computational time. Further, there are serious numerical difficulties implicit in the formulation. Computation of ϕ_{zz}, is particularly sensitive to small errors in ϕ and iterations based on this is rather dangerous. This scheme showed difficulties even for a solitary wave of height 0.2.

Notwithstanding the different procedures used by the previous authors, their experiences suggest that a good deal of care is necessary to achieve a satisfactory radiation boundary for free surface waves. Below we describe the procedure developed in the present work.

5.3.1 Computational Preliminaries

At each time step, two systems of Laplace Equation are solved, one in ϕ and the other in ϕ_t. For a complete formulation of the elliptic Laplace problem, boundary conditions for both the systems need to be specified on the radiation boundary. This boundary condition may be of the Dirichlet or the Neumann type. From the point of computational efficiency, it is desirable to formulate the problem so that the type of boundary conditions is the same for both the systems.

Another point worth noting is that in most problems involving a radiation condition the radiation boundary has been applied at a fixed location. This is not convenient in nonlinear free surface problems using Lagrangian updating. As a consequence of the Lagrangian updating, the nodes on the free surface move in both horizontal and vertical directions (see fig. 5.1). If the radiation boundary is to be at a fixed location, the free surface nodes have to be redistributed to stay within this boundary and the surface elevation η and potential ϕ at the new locations would have to be determined through interpolation. This is not numerically attractive and has been avoided here. On the other hand, we are free to choose how the radiation boundary moves since it is an arbitrary boundary any way as long as we are able to specify the appropriate boundary conditions at the chosen position. A suitable option, which is adopted here, is to set the the radiation boundary to be vertical and moving horizontally with the Lagrangian node at the intersection with the free surface at each time step. The boundary data either in the form of Dirichlet or Neumann type then need to be determined at this location. The moving radiation boundary

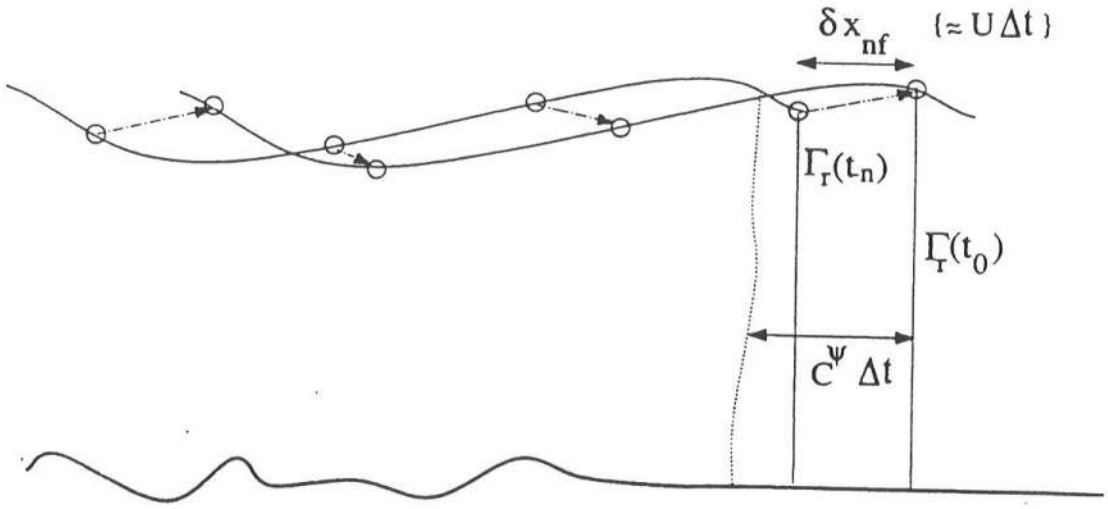

Figure 5.1: Sketch of the numerical scheme for the radiation boundary

adopted here has an analogy in the active wave absorber considered by Milgram (1970).

5.3.2 Numerical Implementation of the Radiation Condition

In analogy to Orlanski (1976), the radiation boundary is based on (5.9) where ψ now refers to a wave quantity η, ϕ or ϕ_t. The wave velocity C^ψ of ψ is permitted to be varying with space and time. An integral representation of the radiation condition is possible by writing (5.9) in a characteristic form as

$$\psi_t + C^\psi \psi_x = \frac{d}{dt}\psi(x,z,t) = 0 \tag{5.21}$$

along

$$\frac{d}{dt}x = C^\psi \tag{5.22}$$

An integration of (5.21) with respect to time yields

$$\psi(x,z,t) = \psi(x',z,t') \tag{5.23}$$

where

$$x = x' + \int_{t'}^{t} C^\psi \, dt \tag{5.24}$$

Equations (5.23) and (5.24) will be the key to the numerical implementation of the radiation condition instead of (5.9). Consider now that at time $t = t_0$, the radiation boundary Γ_r is located at $x = x_0$. For waves propagating to the right, C^ψ is positive and thus for $t' < t_0$ the point located at

$$x' = x_0 - \int_{t'}^{t_0} C^\psi \, dt \tag{5.25}$$

lies inside the computational domain $\Omega(t')$ (fig. 5.1) provided

$$\int_{t'}^{t_0} C^\psi \, dt > \delta x_{nf} \tag{5.26}$$

where δx_{nf} is the horizontal displacement of the free surface node at the intersection from its position at time t' to that at t_0. ϕ and ϕ_t at the boundary $\Gamma_r(t_0)$ can be obtained by using (5.23) under the condition that (5.26) is satisfied. In the numerical scheme, the boundary values are available at discrete time levels. A convenient choice for t' then is t_{-n}, where t_{-n} denotes the time n steps before t_0. Two factors influence the choice of the number of steps n in t_{-n}. If the waves are unsteady, $(t_0 - t_{-n})$ should be as small as possible (*i.e.*, $n = 1$) so that the assumption of locally steady propagation introduces minimum error. On the other hand, the difference between the phase speed and the particle velocity is small for steep waves and x' can be made to lie well within the boundary $\Gamma(t_{-n})$ by choosing a relatively higher value of n. Earlier in chapter 2, a procedure has been developed to compute field accurately at points close to the boundary. Hence, it is not a concern in the present numerical scheme if the point x' lies close to the boundary $\Gamma_r(t_{-n})$.

To complete the formulation of the radiation boundary we need to develop a procedure for evaluating C^ψ. For waves of permanent form C^ψ is constant over time and is the same for ψ being ϕ, ϕ_t or η. We defer the discussion on C^ψ for waves of nonpermanent form to a later section.

5.3.3 Assumptions in the Formulation

It is important at this time to explicitly state the assumptions behind the radiation formulation. For the radiation formulation (5.9) to be valid, C^ψ must be well-defined and positive. In addition, variation of C^ψ should be mild over space and time so that suitable numerical evaluation of the the integral $\int C^\psi \, dt$ is possible without much loss of accuracy.

These assumptions are clearly satisfied in case of waves of permanent form and need to be investigated for waves of arbitrary form.

5.3.4 Treatment of the Free Surface Node

Intersection of the free surface with the radiation boundary poses some additional problems. The free surface updating, described in chapter 2, giving the elevation η and potential ϕ at the intersection point has to use one-sided differencing to calculate the Lagrangian derivatives at the intersection node. When these values are used at the intersection point for high waves, instabilities appear near the radiation boundary. On the other hand, the radiation condition (5.9) can be explicitly enforced at the intersection point x_0 at time t_0 by stating

$$\eta(x_0, t_0) = \eta(x', t_{-n}) \tag{5.27}$$

$$\phi(x_0, \eta, t_0) = \phi(x', \eta, t_{-n}) \tag{5.28}$$

$$\phi_t(x_0, \eta, t_0) = \phi_t(x', \eta, t_{-n}) \tag{5.29}$$

It should be noted that x' obtained from (5.25) for $t' = t_{-n}$ may be different for each of the variables η, ϕ and ϕ_t in case of waves of nonpermanent form. The terms on the right hand side are calculated by interpolation between the discrete nodal values at the free surface at t_{-n}. It is found that enforcing the radiation condition explicitly at the intersection point improves the behavior of the free surface significantly.

5.4 Radiation of Waves of Permanent Form

An important step in developing the generalized formulation is the radiation of waves of permanent form. The phase velocity C in this case is well-defined and is the same constant parameter for essentially all variables including ϕ, ϕ_t and η. Due to the constancy of C, (5.23) is identical to

$$x_0 = x' + C(t - t_{-n}). \tag{5.30}$$

Taking n to be 1 in (5.30), (5.26) is satisfied if $C\Delta t \geq \delta x_{\mathrm{nf}}$ (see fig. 5.1). Since δx_{nf} is the particle displacement over Δt, this is satisfied except near the crest of the breaking

wave. Also as the radiation formulation is exact in this case, the stability and accuracy of the implemented numerical procedure can be verified by sample numerical examples.

5.4.1 Numerical Example 1: Radiation of a Solitary Wave

Fig. (5.2) shows the surface elevation η and ϕ_{tn} during the propagation of a solitary wave of height $H = 0.6$. The initial free surface and the potential distribution corresponding to this height are obtained from the method outlined in Tanaka (1986). The figure shows the permanent form is maintained as the wave propagates towards the radiation boundary and eventually leaves the computational domain. The variation of ϕ_{tn} is included since ϕ_{tn} is more sensitive to disturbances and reflects instabilities even when these are not visually observable on the surface profile. Thus, the smooth variation of ϕ_{tn} even near the radiation boundary for this steep wave is very encouraging.

A quantitative assessment of the error can be provided by comparing the computed free surface ϕ_n to ϕ_n on the surface of a permanent form. For a wave of velocity C, ϕ_n at a surface point is given by

$$\phi_n = -C \sin\beta \tag{5.31}$$

where β is the angle between the horizontal and the tangent to the free surface at that point. At any instant, $\sin\beta$ at a nodal location is obtained by computing the derivative η_s based on a 11-node polynomial (the procedure for computing the derivatives is same as described in chapter 2). A normalized index of the error, given by

$$\Delta\phi_n = \left| \frac{\phi_n + C \sin\beta}{C} \right| \tag{5.32}$$

is shown in fig. (5.3) at three different times of propagation as the crest goes through the radiation boundary. The maximum error is less than 0.001 or 0.1% in spite of the larger error at the end. The error is larger at the end partly because of the computation of $\sin\beta$ in (5.32) using the 11-node polynomial according to the procedure described in chapter 2 is likely to be less accurate at the end. Also, the free surface potential ϕ has higher error towards the end of the free surface during the temporal evolution irrespective of the accuracy of the lateral boundary conditions. This causes ϕ_n to be less accurate at the end.

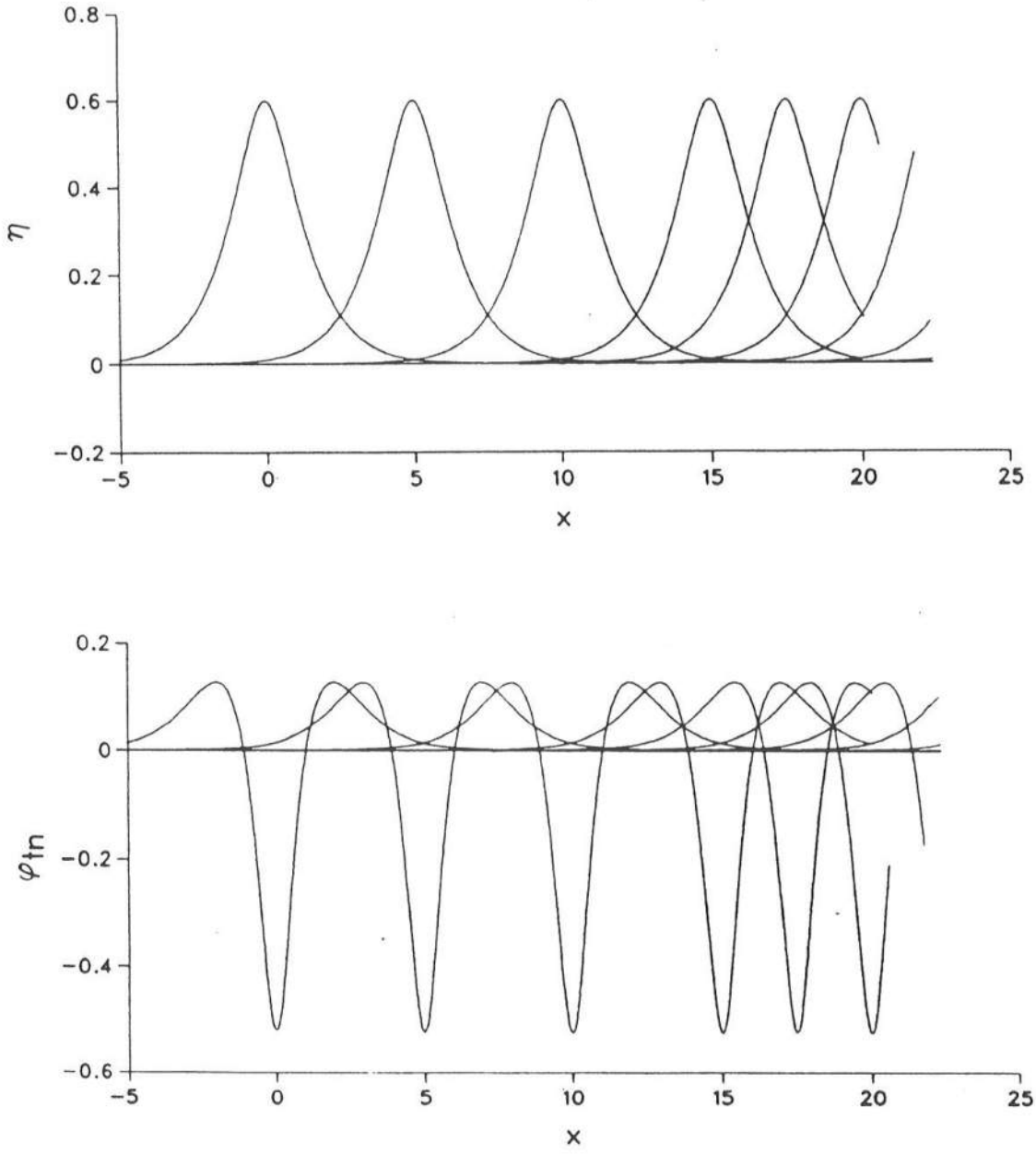

Figure 5.2: η and free surface ϕ_{tn} during the propagation and radiation of a solitary wave of $H = 0.6$. $\Delta x = 0.2$, $\Delta t = 0.05$. Cubic 'mid-interval approximation' method (chapter 2) is used for free surface discretization. The crest is at $x = 0$ and the radiation boundary is at $x = 20$ at the initial time. Profiles at time $t = 0.0$, 4.0, 8.0, 12.0, 14.0, 16.0, 18.0, 20.0, 22.0, 24.0, 26.0.

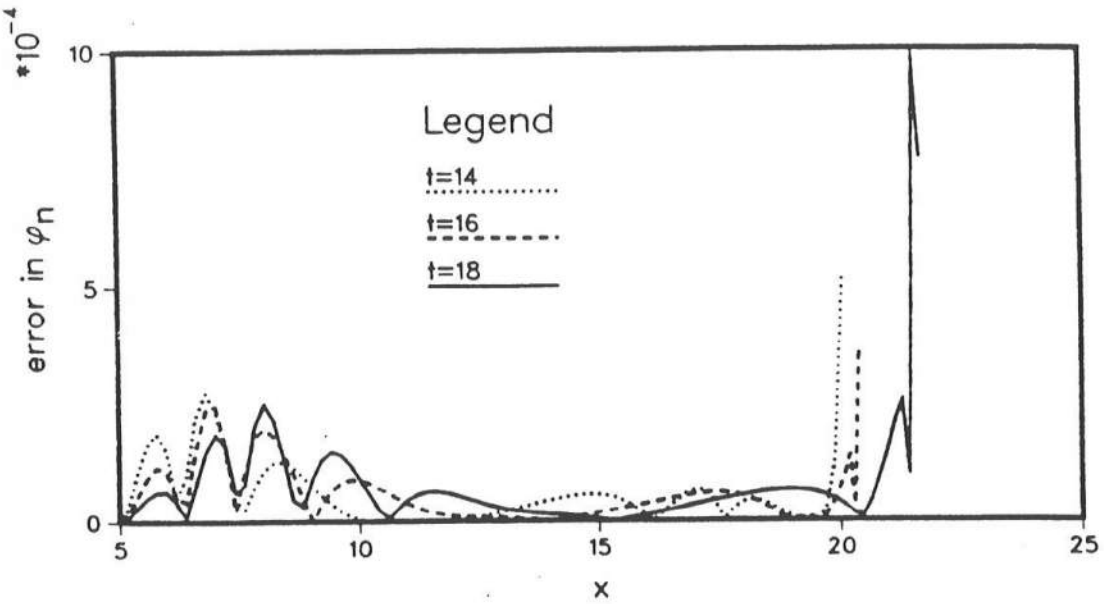

Figure 5.3: Error in free surface ϕ_n during radiation of a solitary wave of $H = 0.6$. Variation of η and ϕ_{tn} are shown in fig. 5.2.

5.4.2 Numerical Example 2: Transient Stream Function Waves

The motion due to a solitary wave is unidirectional. Hence, another application of the radiation formulation is considered where the flow is oscillatory. In chapter 4, generation of a stream function wave was considered and was studied (fig. 4.8 and table 4.1) using a radiation boundary to eliminate reflection. The radiation aspect of the problem is now discussed.

Since the generation begins from the still water condition, the wave field is initially transient over a duration of a few wave periods. However, a constant value, that of the phase velocity for the steady height and period of the generated wave obtained from the Stream Function theory, is used for C in (5.30) throughout the computation. The computation shows that the wave field becomes steady after about 6 wave periods and the results are analyzed during the $8th$ period. In this case, uniformity of the amplitude across the domain can be used as a check of the performance of the radiation boundary. If reflection from the radiation boundary occurs, the spatial variation of the amplitude will show modulation over a length of $L/2$, L being the wave length for the generated wave.

Table 5.1: Computed harmonics during the generation and radiation of a Stream Function wave of $H = 0.4$ and $T = 10$. Free surface discretization is based on quasi-spline elements, $\Delta x = 0.175$. Length of the domain is 11.2, and the wave length is 9.931.

j	Stream Function	computed results		
		$x/h = 4.2$	$x/h = 6$	$x/h = 8.4$
1	0.1728008990	0.1723554730	0.1711650490	0.1715103390
2	0.0686091185	0.0687872171	0.0680692196	0.0685715079
3	0.0247484073	0.0253041763	0.0257703178	0.0253391713
4	0.0093022734	0.0088652596	0.0102853999	0.0097292326
5	0.0037392378	0.0039088689	0.0041867122	0.0039189234
6	0.0015934634	0.0015381004	0.0019772022	0.0016338350
7	0.0007094676	0.0007612444	0.0008799590	0.0007010209
8	0.0003262556	0.0003306544	0.0004390327	0.0002578150
9	0.0001537243	0.0001545730	0.0002031644	0.0001799094

Besides, the uniformity can also be affected by the remnants of the transient modes. The amplitudes of different harmonics at several locations are presented in table 5.1. (Table 4.1 is reproduced here as table 5.1 for convenience.) The table shows a negligible variation of the amplitude over distance (being less than 1% for the 1st harmonic). The higher harmonics are less uniform than the lower harmonics. This could in part be caused by the low numerical resolution due to the discretization used.

5.5 On the Determination of C^ψ for Unsteady Waves

We now turn to the question of unsteady waves and the definition and determination of C^ψ in (5.24). C^ψ is likely to be different for ψ being η, ϕ or ϕ_t unlike in the case of waves of permanent form. If a radiation formulation based on (5.9) is to be valid the basic procedure, as suggested by Orlanski, is to assume the same condition to be valid at the immediate interior grid at the previous time step. Accordingly, C^ψ may be calculated from

$$C^\psi = -\frac{\psi_t}{\psi_x}\Big|_{(nf-1,t_0-\Delta t)} \tag{5.33}$$

Several methods have been discussed in the literature to calculate C^ψ. These methods differ by the finite difference formulations used to obtain ψ_t and ψ_x based on the values available at discrete nodes and time steps (see Hedley & Yau, 1988). However, a basic

problem reported in many studies is that the variation of the computed C^{ψ} is marked by large spikes and negative values. Such variations of C^{ψ} clearly violate the implicit assumptions behind the validity of the radiation formulation.

The different procedures adopted by different authors to circumvent the problem fall in to two categories. Orlanski (1976) and Yen & Hall (1981) use a modified value C^{ψ^*} in place of C^{ψ}. The modified value is defined according to the principles:

$$\begin{aligned} C^{\psi^*} &= 0, \text{ if } C^{\psi} \leq 0; \\ &= \frac{\Delta x}{\Delta t}, \text{ if } C^{\psi} \geq \frac{\Delta x}{\Delta t}; \\ &= C^{\psi}, \text{ if } 0 \leq C^{\psi} \leq \frac{\Delta x}{\Delta t}. \end{aligned} \tag{5.34}$$

Alternatively, recursive filter has been used to reduce the spikes from the variation of C^{ψ} (Kantha *et al.*, 1990).

The rationale behind these procedures are not clear. Intuitively, these procedures may work satisfactorily if the computed value of C^{ψ} from (5.33) violates the assumptions of the radiation formulation only over very short duration. However, this is not necessarily the case if waves of arbitrary form are considered.

In some instances, the spikes may be of numerical origin. For simplicity, consider a monochromatic sine wave propagating to the right, *i.e.*,

$$\psi(x,t) = A\sin(kx - \omega t). \tag{5.35}$$

Clearly, the phase velocity in this case is well defined and is a constant parameter, given by ω/k. At the time the crest or the trough is at the radiation boundary, both ψ_t and ψ_x go to zero simultaneously. However, the numerically determined ψ_t and ψ_x may not go to zero at the same rate due to small errors and the variation of C^{ψ} may exhibit spikes as the crest or the trough passes over the radiation boundary. This seems to be the case in the example considered by Kantha *et al.* (1990) (they study a linear system excited by a single sine wave). The phase velocity in such a case can be recovered by using the L'Hospital's rule, *i.e.* expressing the phase velocity as the ratio of the derivatives ψ_{tx} and ψ_{xx} if ψ_t and ψ_x get below a numerical tolerance.

The real problem, however, is more fundamental. Consider the propagation of two sine waves as the first simple model of an unsteady form. For propagation to the right, the combined potential due to the two waves of surface amplitude A_1 and A_2 is

$$\begin{aligned}\phi(x,z,t) &= (A_1 g/\omega_1)\frac{\cosh k_1(h+z)}{\cosh k_1 h}\sin(k_1 x-\omega_1 t)+ \\ &\quad (A_2 g/\omega_2)\frac{\cosh k_2(h+z)}{\cosh k_2 h}\sin(k_2 x-\omega_2 t+\theta) \qquad (5.36)\end{aligned}$$

where g is the acceleration due to gravity and θ is a constant number. This simple model can serve to illustrate the problems of defining C for unsteady waves even if our ultimate interest is in nonlinear waves. $C^\phi(0,0,t)$, the propagation speed of ϕ defined by (5.33), can be evaluated exactly in this case by calculating ϕ_t and ϕ_x from the expression (5.36). The temporal variation C^ϕ so obtained at $x = z = 0$ is shown in fig. 5.4. The figure shows the

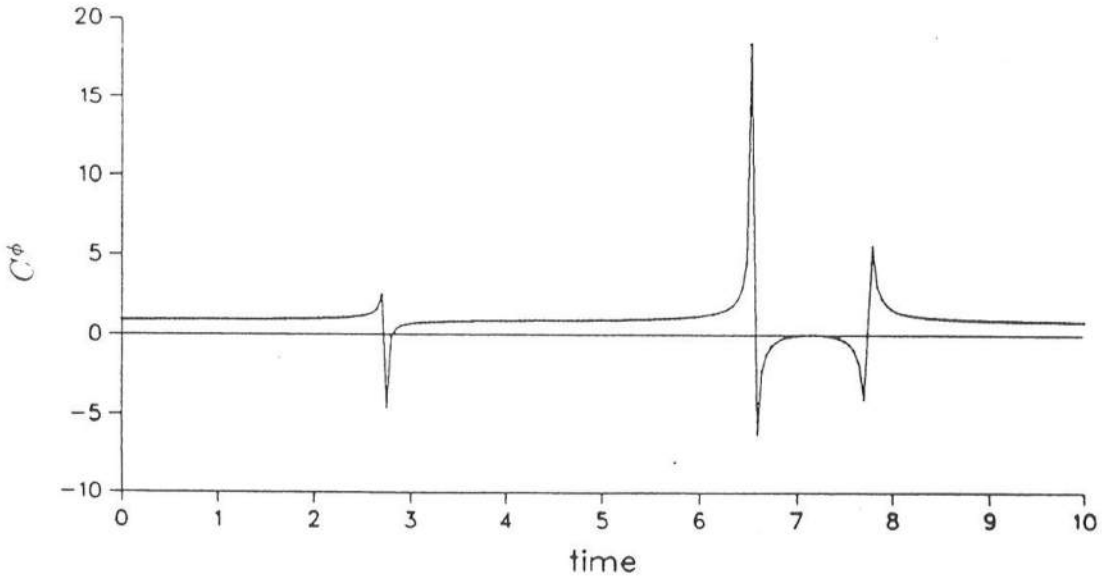

Figure 5.4: Variation of C^ϕ at $x = z = 0$ under a linear field containing two sine waves as given by (5.36). $A_1 = A_2 = 0.1$, $\omega_1 = 0.885$, $\omega_2 = 0.59$, $\theta = 1.0$. $C_1 = 0.908$, $C_2 = 0.941$.

presence of the spikes and the negative value of C^ϕ over a duration of time comparable to the periods of the individual components. If (5.34) is now used, the modified phase speed C^{ϕ^*} assumes the value of zero over a long duration. It is, however, evident from the linear

theory that the reflection of both the components can be minimized by choosing C^{ϕ^*} to lie between the phase speeds C_1 and C_2 of the two components. Thus, (5.34) is clearly not a desirable solution for the problem considered. Furthermore, fig. 5.5 shows negative value and spikes in the spatial variation of the computed C^{ϕ} to the left of $x = 0$ suggesting that modification of C^{ϕ} by averaging over space is not a suitable solution either.

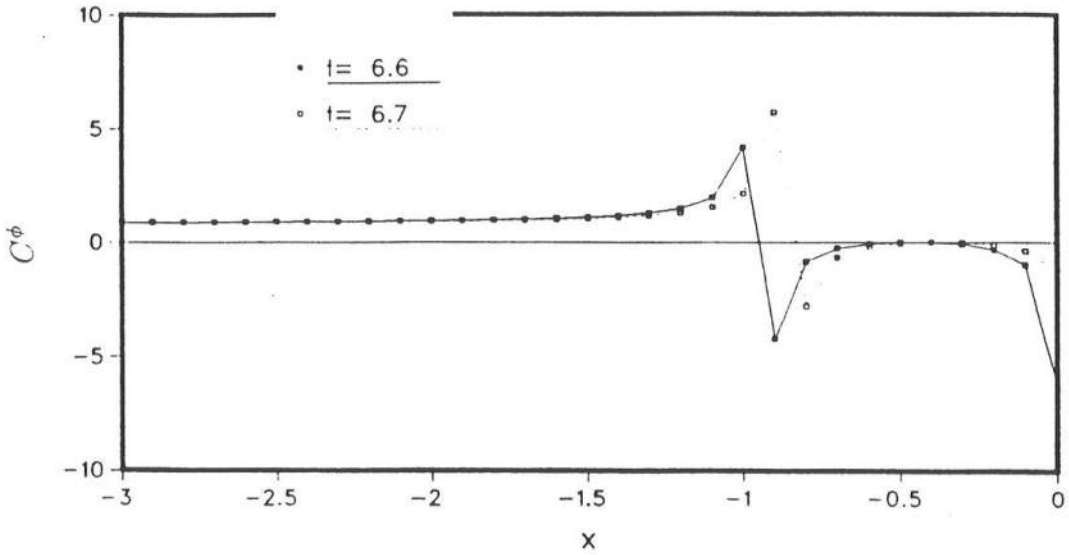

Figure 5.5: Variation of C^{ϕ} over at $t = 6.6, 6.7$ under a linear field containing two sine waves. $A_1 = A_2 = 0.1$, $\omega_1 = 0.885$, $\omega_2 = 0.59$, $\theta = 1.0$. $C_1 = 0.908$, $C_2 = 0.941$.

5.6 Concluding Remarks

The phase speed C^{ψ} is in principle allowed to be varying in the present formulation. However, a well-defined phase speed does not exist for unsteady dispersive waves as it does for waves of permanent form. As shown in the example above, the common methods used in the literature to define a phase speed are not suitable if the wave field comprises of components having different phase speeds. Therefore, using a phase speed calculated from the interior point as proposed by Orlanski (1976) is not advocated here. Performance of the present radiation formulation has been shown to be very good in case of propagation of permanent form. In addition, results of the computation using a properly selected constant

value of C have been found to be satisfactory in several cases of unsteady propagation. An example of a transient front is shown in fig. 5.6. Furthermore, the radiation formulation

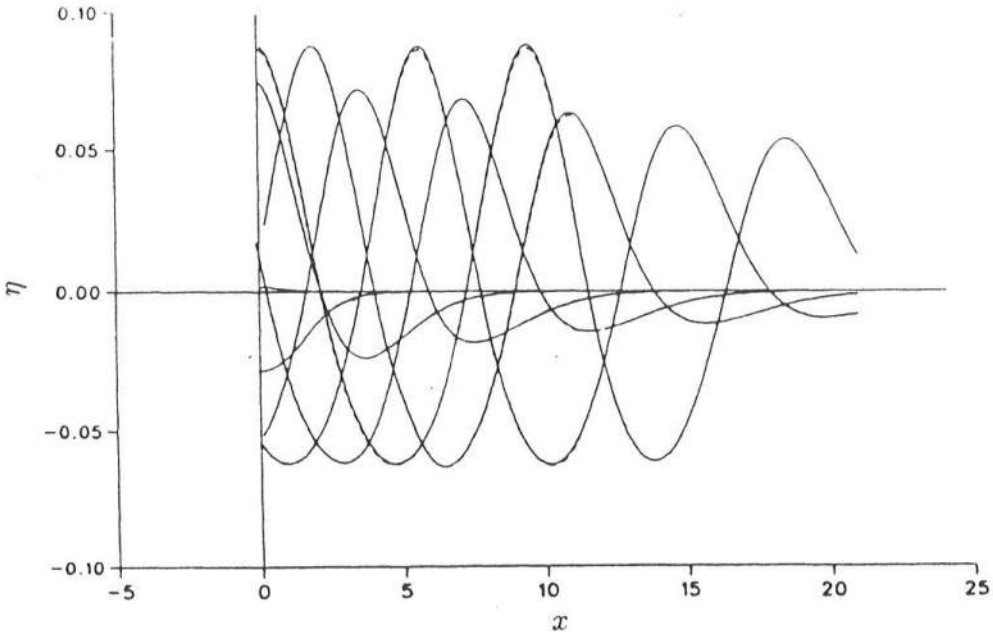

Figure 5.6: Solid line: surface elevations from the computation over a larger domain with the radiation boundary at $x = 22$, dotted line: surface elevations from the computation over a smaller domain with the radiation boundary at $x = 11$. Waves are generated from rest through the lateral boundary initially at $x = 0$. $H = 0.15$ and $T = 10$ of the corresponding steady form. The value used for C is 0.943 corresponding to the steady form from the stream function theory.

has been found to be reasonable in application to waves which are time-periodic though spatially modulated as in the case of finite amplitude waves generated by a rigid wave maker. A constant value of C, corresponding to that of a steady form of the same period T and an identical height, is also used in this case during the entire duration of the computation.

The numerical formulation used here is new and has been found to be effective and stable even for very high waves. Numerical radiation combining the concept of a sponge layer and the Sommerfeld condition has been suggested by Israeli & Orszag (1981). This approach may be pursued for the unsteady free surface motion to achieve a procedure for general applicability. The basis of a such a procedure is conceptually simple: tune the

Sommerfeld condition to allow the longer waves to transmit through while the shorter waves should be damped over a small portion of the computational domain. However, the complete formulation and successive modifications require several important numerical and theoretical analyses.

Chapter 6

STEEP SOLITARY WAVES AND BREAKING ON SLOPES

6.1 Introduction

Solitary waves have been a source of great interest, both from practical and theoretical aspects, since the time of their discovery by Russell in 1834. In recent years, a lot of ground has been gained regarding steep solitary waves. Numerical methods (*e.g.*, Hunter & Vanden-Broeck, 1983 and Tanaka, 1986) are now available to obtain accurate numerical solutions to steep solitary waves of permanent form up to the limiting height. Nonmonotonic behavior of phase speed, energy and impulse with wave height, shown earlier by Schwartz (1974) in case of periodic gravity waves, has also been found for solitary waves by Longuet-Higgins (1974). Recent expositions by Tanaka (1986) and Zufiria and Saffman (1986) establish that the highest stable wave corresponds to the wave of maximum energy and is 0.78. These analyzes and findings on waves of permanent form have provided a basis for further work on unsteady problems.

Unsteady propagation, spurred by bottom variation, is of primary importance to coastal engineers and will be dealt with in this chapter. The interest in solitary waves stems from the resemblance of the leading waves caused by seismic vibration or landslides to the solitary form. Besides, being one of the most tractable phenomena for theoretical analysis, studies of solitary waves have been undertaken with a view to providing answers to the behavior of oscillatory or periodic waves. Whereas some promise can be seen in that direction, significant differences between the behavior of oscillatory waves and solitary waves may invalidate extending the results of solitary wave analysis to periodic waves.

6.2 Propagation of Very High Solitary Waves

Before proceeding further, it is considered important to analyze the propagation of steep solitary waves using the present numerical scheme. Barring surprises, the permanent form is expected to be maintained. But, the utility of such an exercise is to obtain estimates of the numerical error during a strongly nonlinear propagation and establish some degree of reliability for the more complicated unsteady processes to be undertaken later.

6.2.1 Initial Free Surface Condition and Permanent Form Solitary Wave

Starting from the still water condition, a solitary wave may be generated in a computational domain by a wave maker as described in chapter 4. This procedure has two drawbacks. First, considerable computational time is lost before a fully developed solitary wave is obtained. More importantly however, steep waves generated by the wave maker are not accurate in form and generate a a dispersive tail.

Alternatively, the computation may start with the free surface conditions corresponding to a solitary wave of permanent form. Such an initial surface elevation and the potential distribution can be obtained from an appropriate formulation satisfying the exact free surface conditions. Solutions based on series expansion like that of the $17th$ order by Pennell and Su (1984) or the $9th$ order by Fenton (1972) seem attractive since the profile for any height can be expressed as an analytical series with a set of coefficients already known from their calculations. However, Pennell (1987) has shown that seeming convergence of the coefficients of a $17th$ order series expansion can be misleading since the coefficients begin to diverge when an expansion of higher order such as $27th$ is considered. Thus, the free surface elevation and potential based on series expansion may be inaccurate. In consequence, use of the series expansion for very steep waves has been avoided here.

An integral formulation, due to Tanaka (1986)[4] is known to yield an accurate solution to solitary waves of height close to the limiting height. Since the interest in this chapter includes waves of height close to the highest stable solitary wave, the surface

---

[4] The author gratefully acknowledges the help of Mark Cooker and Dr. Peregrine in providing Tanaka's algorithm for the solution of the wave of the permanent form.

profile and velocity potential at the initial time will be obtained from Tanaka's procedure. These profiles for two different heights are shown in figs. (6.1).

6.2.2 Some Computational Aspects of Modeling Steep Solitary Wave

Numerical difficulties associated with the modeling of solitary waves increase considerably with increasing steepness. Consider the variation of β and ϕ_{tn} for the two waves of height 0.7 and 0.775 shown in fig. 6.1. Measured positive counterclockwise from the horizontal, β is the angle made by the tangent to the free surface. The variation of β shows the inflection point of the surface profile and the sharp rate at which the surface curvature changes around this point. The change from the maximum negative value of β to its maximum positive value takes place over a fraction of the depth. On the other hand, the variation of ϕ_{tn} becomes steep very rapidly at the crest with increasing wave height. Thus, two regions of extremely steep variation exist and a high resolution description of both the geometry and the flow quantities is necessary near the crest.

Noting that the high resolution is required around the crest over a length of only one or two water depths it is efficient to use Δx smaller near the crest increasing with distance away from it. Accuracy of Tanaka's algorithm for steady solitary wave of permanent form comes partly from a very fine distribution of nodes near the crest (though rapidly getting sparse away from the crest). Using the same distribution of nodes to describe the initial surface elevation η and free surface potential ϕ for the purpose of studying propagation turns out to be unsatisfactory for two reasons. First, the time step Δt has to be proportionately small corresponding to a small separation between the nodes to maintain a *Courant* number necessary for the stability of the computation. Thus, a very high density distribution of nodes near the crest ends up in an impractical number of time steps to analyze propagation over considerable distance.

The second reason comes from the difference in the phase speed with which the crest moves and the speed of an individual fluid particle on the surface. A novice fine distribution of nodes near the crest of the initial profile may result in the crest being in a region of sparse grids during the propagation. For steadily propagating waves, the wave form is stationary from a reference frame moving with the phase velocity. It has been

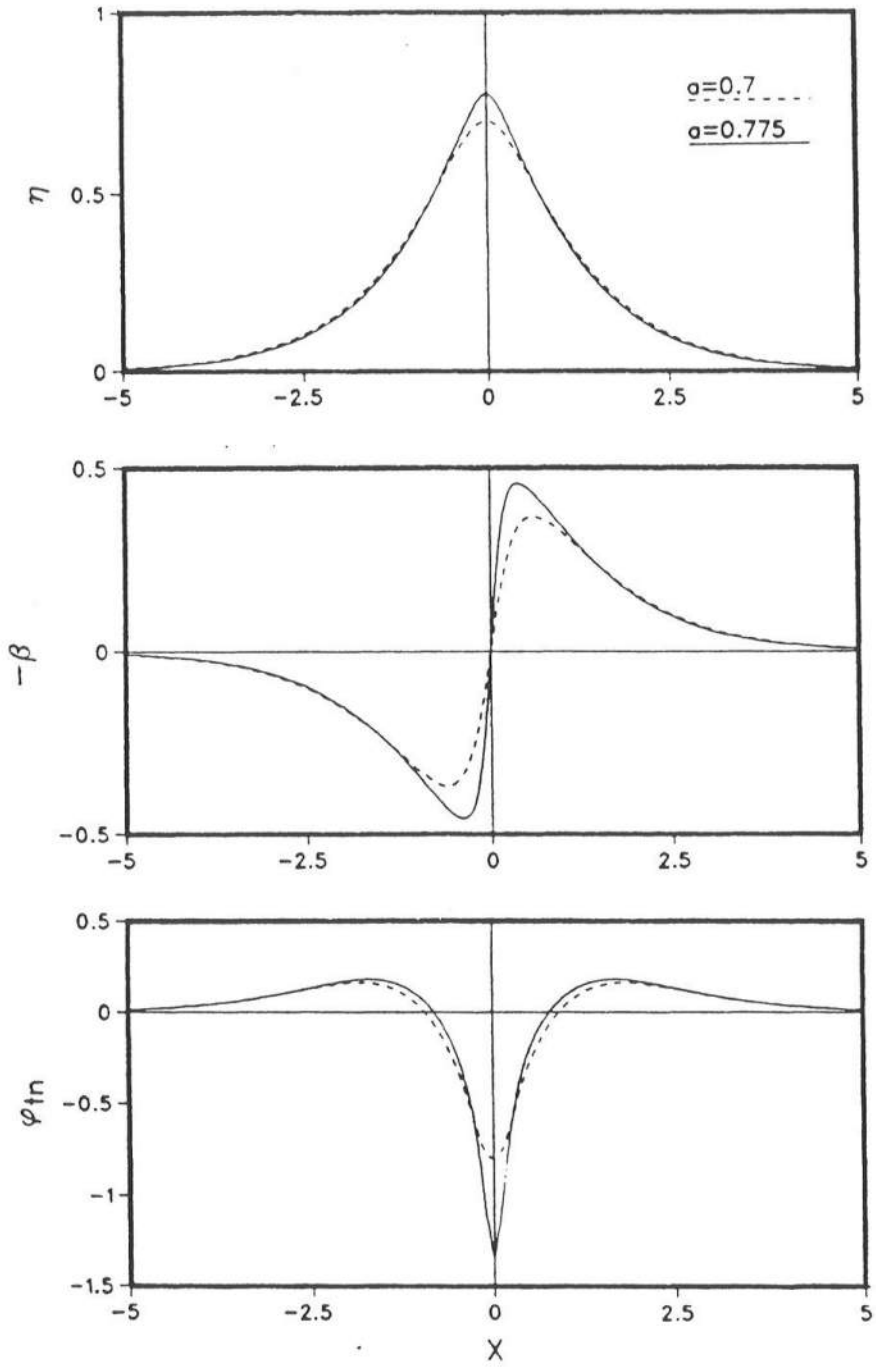

Figure 6.1: Surface elevation η, β and ϕ_{tn} on the free surface for two solitary waves of permanent form. β is the angle measured from the horizontal to the tangent to the free surface.

pointed out in Cooker *et al.* (1990) that the distribution of nodes will be maintained constant if the separation between nodes is proportional to the local fluid speed along the free surface as seen from this reference frame. This can be used as a guideline to achieve an efficient distribution of the free surface nodes at the initial time. For solitary wave motion, an expression for distribution of nodes satisfying this principle is given by

$$\Delta x(x) = \Delta x_2 + (\Delta x_1 - \Delta x_2) \exp^{-|x-x_0|} \tag{6.1}$$

where, x_0 is the position of the crest and Δx_1 and Δx_2 are the smallest and the largest spacing as specified over the free surface. The ratio of $\Delta x_1/\Delta x_2$ is about 1 (uniform spacing) for small waves and about 1/3 for very steep waves ($H = 0.78$). In the following section, both uniform spacing and variable spacing according to (6.1) have been adopted to describe the initial η and ϕ and the computed results have been discussed.

6.2.3 Computational Scheme for Propagation

The computational domain (fig. 6.2) is bounded by the free surface (initially specified according to Tanaka's profile), two vertical lateral boundaries on either side and a bottom boundary. The initial domain is chosen large enough so that the surface elevation at the end is of the order of 10^{-08}.

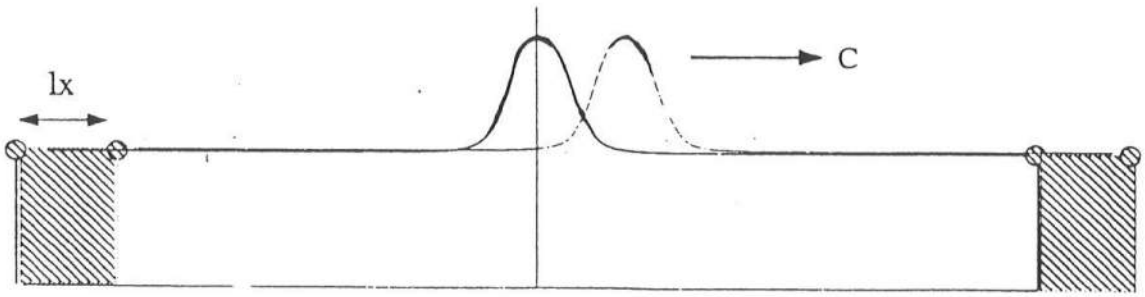

Figure 6.2: Schematic diagram for the propagation of a solitary wave.

Corresponding to a very small η at the ends, zero flux may be specified as the lateral boundary conditions. However, it is found that small disturbances near the right

end may grow at a fast rate using this condition. This situation is improved by using an approximate radiative condition. On the assumption of uniform variation over depth, ϕ_x under a permanent form wave can be expressed as

$$\phi_x = C\frac{\eta}{1+\eta} \tag{6.2}$$

with C as the phase velocity. This equation has earlier been used in chapter 4 in connection with depth averaged horizontal velocity. By taking a time derivative of ϕ_x, ϕ_{tx} is obtained as

$$\phi_{tx} = C\frac{\eta_t}{1+\eta} - C\frac{\eta\eta_t}{(1+\eta)^2} \tag{6.3}$$

Neglecting the second term for small η and using $\partial/\partial t = -C\partial/\partial x$, (6.3) is formulated in terms of spatial derivatives of η as

$$\phi_{tx} = -C^2\frac{\eta_x}{1+\eta} \tag{6.4}$$

(6.2) and (6.4) are used to define the radiative boundary conditions in terms of the free surface η at the right boundary.

If the lateral boundaries stay fixed or move horizontally with end node on the free surface, the solitary hump will leave the computational domain in a short time. Moreover, the approximate boundary condition on the right lateral boundary will be inappropriate as the crest propagates closer to the lateral boundary. This problem is circumvented by using a numerical scheme which lets the computational domain move with the wave allowing propagation over a long time with a finite length of the domain. As the crest propagates to the right, a region on the left is dropped and a region is added on the right (shown schematically in fig. (6.2). It is numerically convenient to work with the same number of nodes as started with. As the crest moves approximately a distance of lx, the distance between the two last nodes, the left box is dropped from the domain and a similar region is added on the right. This keeps the solitary hump in the middle of the computational domain so that propagation can be studied over a long distance. This idea of moving the computational domain has also been implemented in a different computational scheme in the recent work of Cooker *et al.* (1990).

The new node on the right is located at the horizontal coordinate given by

$$X(nf) = 2X(nf-1) - X(nf-1) \tag{6.5}$$

where nf denotes the node number of the new node. η and ϕ at this location are apriori unknown. A second order extrapolation based on the discrete nodal values of η and ϕ of the three preceding nodes is used to obtain η and ϕ at the node. η and ϕ at the nodes $(nf-1)$ and $(nf-2)$ are smoothed before each extrapolation. The smoothing was found necessary to control the errors during extrapolation. ϕ_x and ϕ_{tx} at the lateral boundary at the new location are calculated according to (6.2) and (6.4).

At the left end the first free surface node of the altered domain is located at the position of the second node of the previous domain. Free surface η and ϕ at this position are already known and no extrapolation is necessary as on the right end.

6.2.4 Accuracy of Propagation of the Solitary Wave

In many instances, global quantities like total energy and volume of the computational domain are presented as means of checking the numerical accuracy. These checks can be used as guidelines in the solution of many diverse problems, though they do not reflect concentrated local errors. For propagation of permanent form, criteria for local accuracy can be established based on the time invariance of wave characteristics. In the following, three different measures of local accuracy are discussed.

1. Accuracy of ϕ_n at any instant

2. Variation of wave amplitude with time

3. Variation of ϕ_{tn} at the crest with time

At any given instant, the normal flux at a point (x, z) on the free surface of a wave propagating steadily to the right is given by

$$\phi_n = -C \sin\beta \tag{6.6}$$

where, β is the angle between the horizontal and the tangent to the surface at (x, z) and C is the wave velocity. Thus, a normalized measure of the error in the computed ϕ_n can be expressed as

$$\Delta\phi_n = \left| \frac{\phi_n + C \sin\beta}{C} \right| \tag{6.7}$$

The value of C to be used in (6.7) is obtained from Tanaka's solution for the corresponding wave height. During propagation, the maximum value $\Delta\phi_n$ over all the free surface nodes, denoted by $\Delta\phi_{n_{max}}$, will be used as the index of error. Thus, a very strict test of accuracy is adopted.

In the following, errors and accuracy in the numerical propagation of two solitary waves of height 0.7 and 0.775 are discussed.

Error at the Initial Time

The initial surface elevation η and potential ϕ obtained from Tanaka's algorithm are available at nodes with highly nonuniform spacing. For the present computation regridding of the original data is done to express the initial η and ϕ at nodes spaced uniformly or according to (6.1). The regridding is based on a $10th$ order polynomial in the neighborhood of the new node and is highly accurate.

Fig. 6.3 shows the distribution of $\Delta\phi_n$, as given by (6.7), in the solution of the Laplace equation at the initial time for two different wave heights of $H = 0.7$ and $H = 0.775$. Using quasi-spline elements on the free surface with $\Delta x = 0.15$, the maximum error $\delta\phi_{n\max}$ for $H = 0.7$ is around 0.01 in the present computation. This error is partly due to the difference in the present scheme and Tanaka's algorithm and partly due to the low resolution of the discretization used. Using the same discretization for a higher wave of $H = 0.775$, the maximum error increases to about 0.5. Error near the crest (and the maximum error) decrease by spacing the nodes a bit closer near the crest. However, a substantial reduction in the error is achieved by using the discretization based on the cubic mid-interval elements (described in chapter 2). This is due to the fact that while the quasi-spline elements make a local third order approximation to the variation of the geometry and a linear approximation to the variation of ϕ and ϕ_n (in the solution of

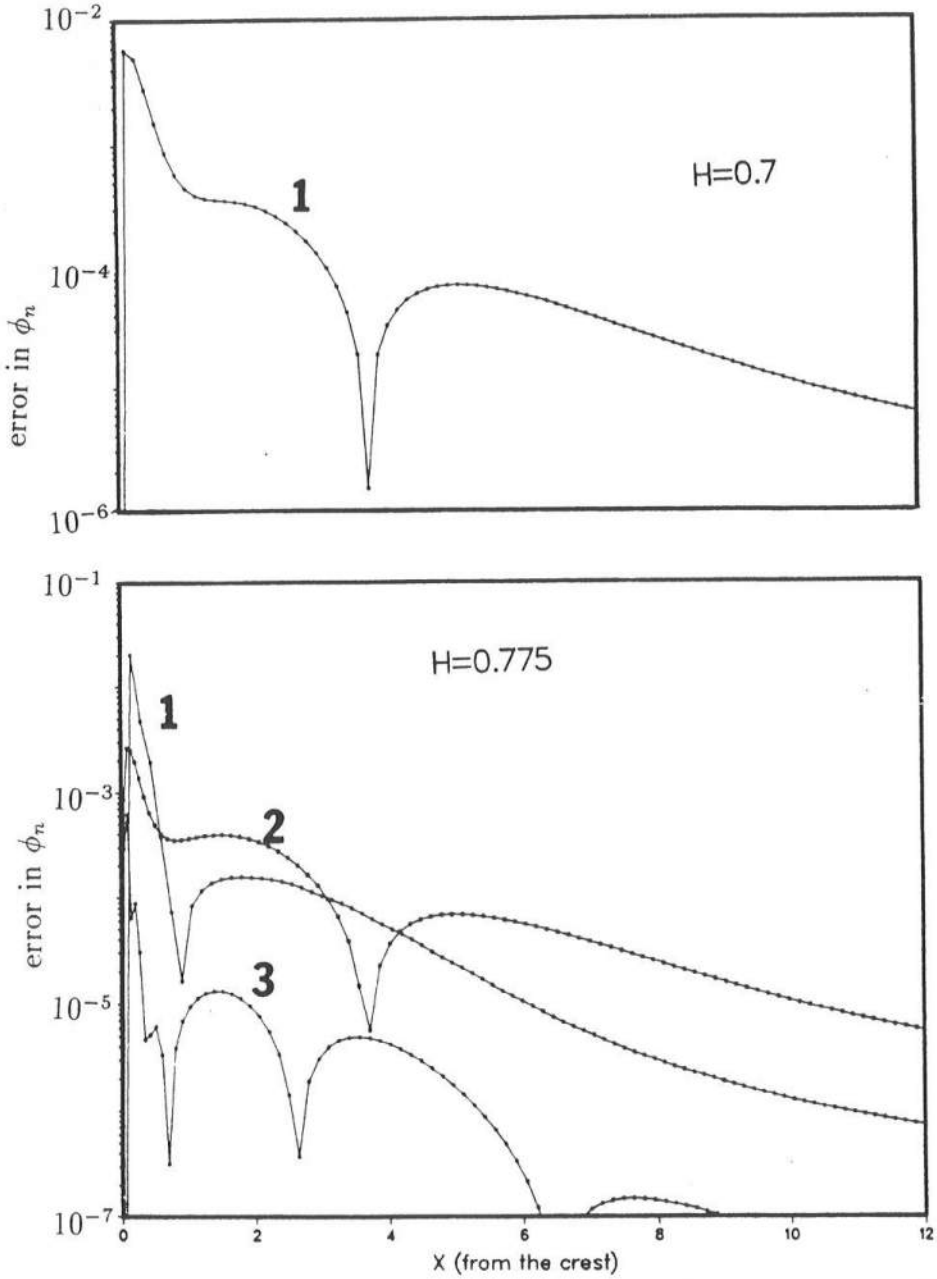

Figure 6.3: Distribution of $\Delta\phi_n$ at the initial time; top: $H = 0.7$, bottom: $H = 0.775$. 1: quasi-spline elements, uniform $\Delta x = 0.15$; 2: quasi-spline elements, variable Δx, $\Delta x_1 = 0.045$ & $\Delta x_2 = 0.18$; 3: Cubic mid-interval elements, variable Δx, $\Delta x_1 = 0.045$ & $\Delta x_2 = 0.18$. The crest is at $x = 0$. The error is zero at the crest due to the antisymmetric behavior of ϕ_n about the crest.

the integral equation), the cubic mid-interval elements make the same third order local approximation to both the geometry and the flow quantities ϕ and ϕ_n.

6.2.5 Error During the Propagation

In addition to an accurate solution of the Laplace equation at each time step, numerical updating of the free surface becomes a critical factor influencing the computed results during the propagation of steep waves. We first study the propagation of a wave of $H = 0.7$ using quasi-spline elements (for the solution of the Laplace equation) with nodes at an uniform spacing of $\Delta x = 0.15$. The tangential derivatives ϕ_s, ϕ_{ss}, ϕ_{ns}, ϕ_{ts} and β_s used in the free surface updating are computed using a 5-node rule (described in chapter 2). Resulting maximum error in ϕ_n is shown by the upper curve in plot A of fig. 6.4. As shown by the lower curve in the same plot, significant reduction in error is achieved by using 11-node rule to compute the tangential derivatives while keeping the same discretization for the solution of the Laplace equation. The improved computational results based on the 11-node derivatives are related to the fact that the steep variation of surface curvature and ϕ_n and ϕ_{tn} are poorly evaluated by the 5-node formula. Indeed, the computation based on 11-node rule to compute the derivatives derivatives showed no irregular behavior till the termination of the computation after a propagation distance of about 100 water depths while the computation based on the 5-node rule had to be terminated due to instabilities near the crest shortly after propagating a distance of about 30 water depths.

Another important observation is the initial decrease of $\Delta\phi_{n\max}$ with time as shown by the lower curve in plot A of fig. 6.4. This corresponds to an improved resolution as a new configuration of the free surface nodes is reached with relatively higher density near the crest during the propagation.

Since using the 5-node rule to compute the free surface derivatives was found insufficient to study the propagation of a wave of $H = 0.7$, this procedure was discarded while extending the analysis to a higher wave of $H = 0.775$. Thus, only 11-node rule has been used to compute the tangential derivatives on the free surface. The results are shown in fig. 6.5. The higher accuracy that can be achieved by using the mid-interval elements,

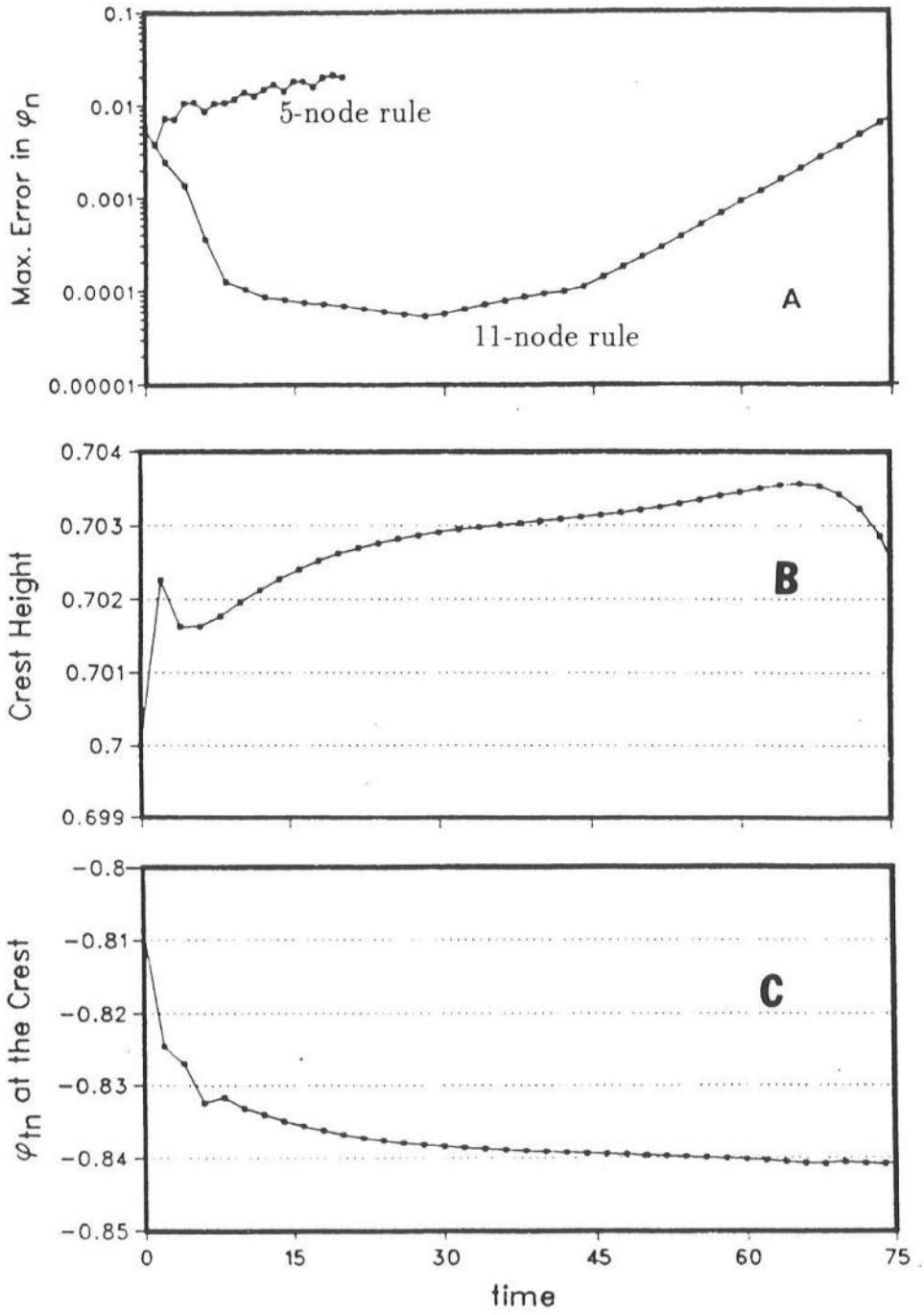

Figure 6.4: Variation of $\Delta\phi_{n\max}$ (plot A), crest height (plot B) and ϕ_{tn} at the crest (plot C) with time for a wave of $H = 0.7$. $\Delta t = 0.01$. Quasi-spline elements on the free surface with *initial* uniform spacing of $\Delta x = 0.15$. Plot A, upper curve: free surface tangential derivatives according to 5-node rule; plot A, lower curve: 11-node rule. Plot B and C show results based on 11-node rule.

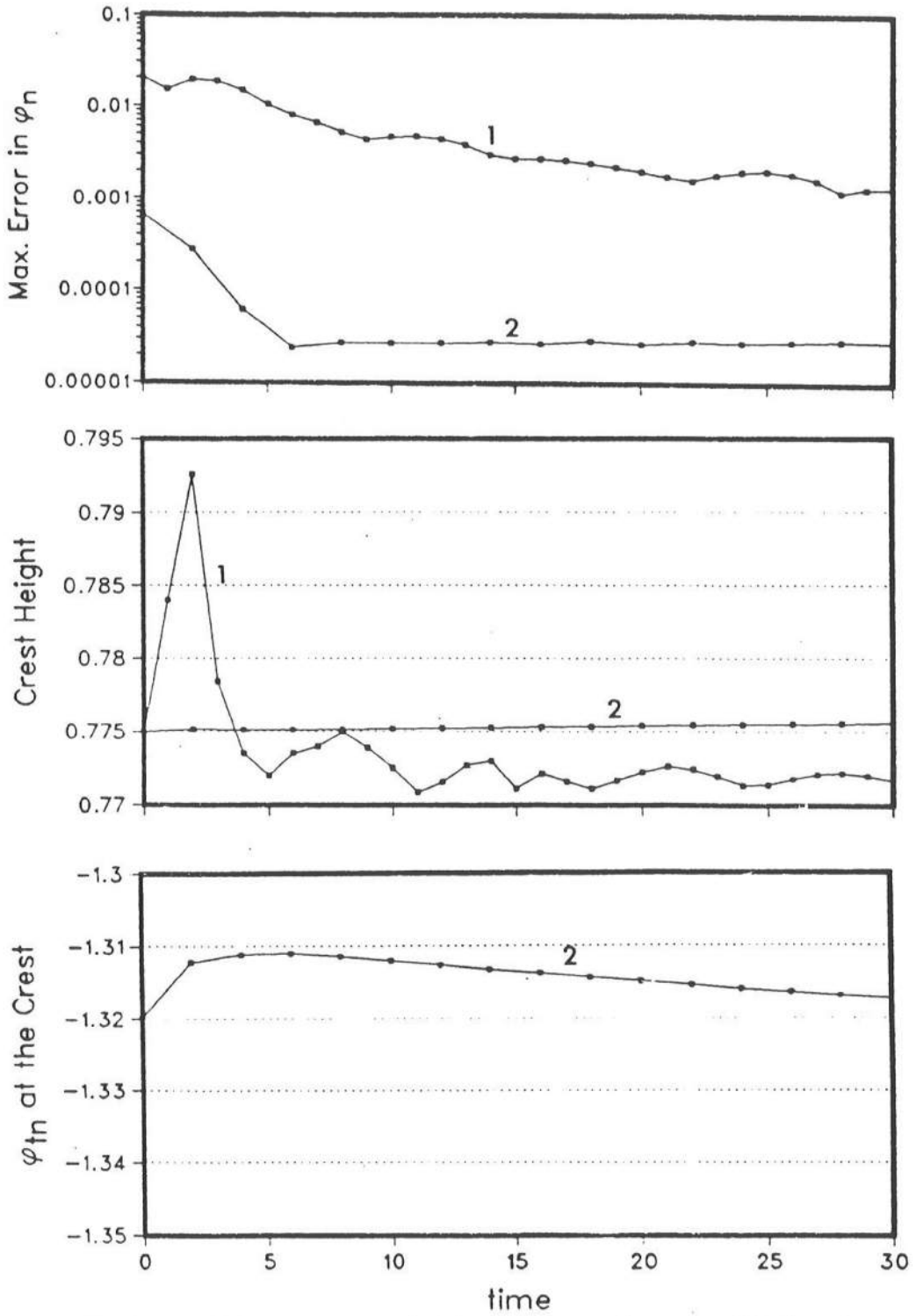

Figure 6.5: Variation of $\Delta\phi_{n\max}$, crest height and ϕ_{tn} at the crest with time for a wave of $H = 0.775$. $\Delta t = 0.01$. 1: quasi-spline elements on the free surface with initially uniform spacing of $\Delta x = 0.15$. 2: cubic mid-interval elements with initially variable Δx according to (6.1); $\Delta x_1 = 0.045$ & $\Delta x_2 = 0.18$. Free surface tangential derivatives are according to the 11-node rule.

indicated earlier in fig. fglap, is also shown clearly during the propagation.

What is more significant is that the amplitude can be preserved to within 0.00015 and $\Delta\phi_{n\max}$ can be maintained at less than 0.00005 over a propagation duration of 30 for a wave which is at the threshold of instability.

Size of Δx and the time step Δt needed to achieve a desired accuracy depends on the discretization used. The same computations as reported in figs. 6.4 and 6.5 showed little improvement by reducing the time step Δt further. No further computation was done with different spacing between nodes. Based on the initial uniform spacing of $\Delta x = 0.15$, the Courant number for the computations is around 0.1. However, this estimate of the Courant number is misleading since the spacing between the nodes decreases near the crest during propagation as a result of the crowding-up. The Courant number in the equilibrium distribution of the nodes on the free surface is about 0.3 for the present computations.

6.3 Particle Drifts

Particles in a quiescent fluid will start drifting due to an approaching solitary wave and finally settle down to a different still position as the solitary hump passes by. The net horizontal displacement between the final and the initial position of the particle is defined as the 'drift'. Earlier analysis by Longuet-Higgins (1981) showed that calculations based on KdV theory significantly underpredict particle drift compared to those given by the $9th$ order solution (Fenton, 1972). Experiments were conducted by the same author to verify the results. Notwithstanding the presence of a large secondary hump in the generated solitary wave, the experimental results supported the higher particle drifts as predicted by the $9th$ order solution. Due to the nonconvergence of the series, the $9th$ order theory is not accurate for waves higher than about 0.7.

Particle drifts in the present computations are calculated by tracking the Lagrangian position of the particle during the propagation of a solitary wave over a uniform depth. Fig. 6.6 shows the comparison of these results. As a reference to the trend of the variation, an isolated point denoting the drift due to a wave of the limiting height is also shown in the plot. This value was obtained by Longuet-Higgins (1979) using the Stokes' corner flow for the limiting height. In the light of the discussion in Pennell (1987),

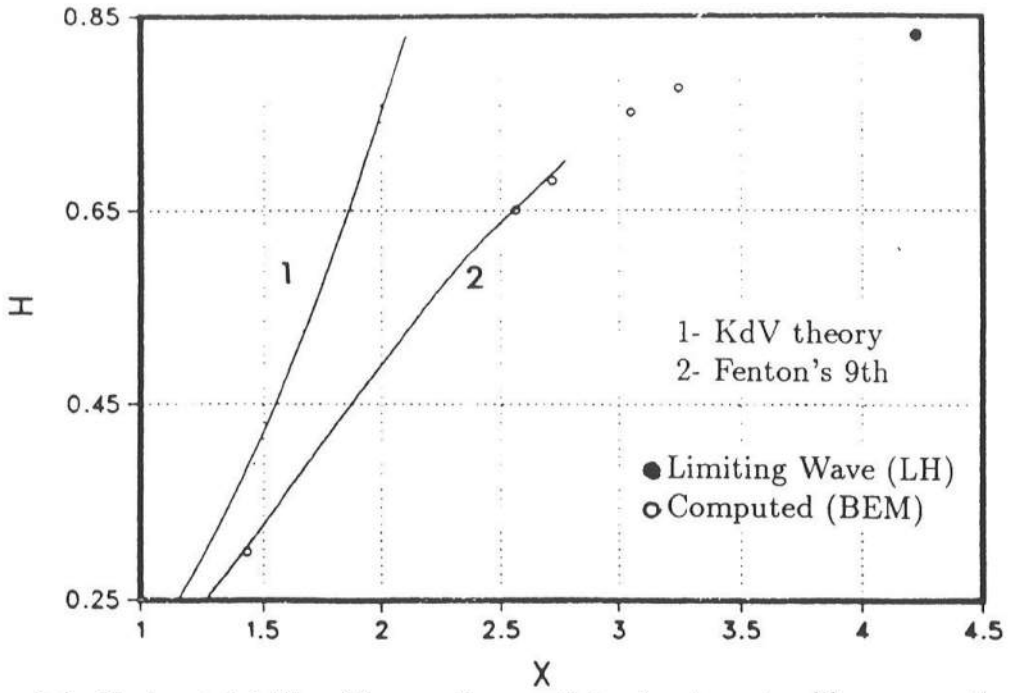

Figure 6.6: Horizontal drifts of free surface particles due to a steadily propagating solitary wave of permanent form on uniform depth. 1: KdV theory, 2: Fenton's $9th$ order theory, rings: present computation. The solid dot denotes the drift due to the limiting wave according to Longuet-Higgins (1979).

it is interesting to note that the $9th$ order solution agrees well with the computed results for waves of height lower than 0.7. Further, the computed results for the higher waves ($H = 0.75$ and $H = 0.775$) follow the trend of the experimental results and the drift at the limiting height. Reliable prediction of drift is important from the point of surface pollutant dispersal, mixing and remote sensing. The drift, obtained from the KdV theory, differs remarkably from the exact nonlinear computation for steep waves. At a height of 0.5, particle drift based on KdV-theory has a difference of about 25% though the difference in the phase velocity at the same height is only 0.7% ! Thus, the particle drift provides an interesting example of emphasizing the utility of an exact nonlinear model even if approximate theories of lower order, like the KdV theory, can represent surface profile and phase velocity within a small percentage of error. This fact has also been pointed out by Longuet-Higgins (1981).

The computational scheme can of course be used to compute particle drifts and

trajectories during unsteady flow. Deformation and steepening of solitary waves can be caused by bottom variation which will be presented in the next section. However, as an example of the particle trajectories due to motion of a solitary wave interacting with a sloping bed, the traces of some selected particles are shown in fig. 6.7. The trajectories

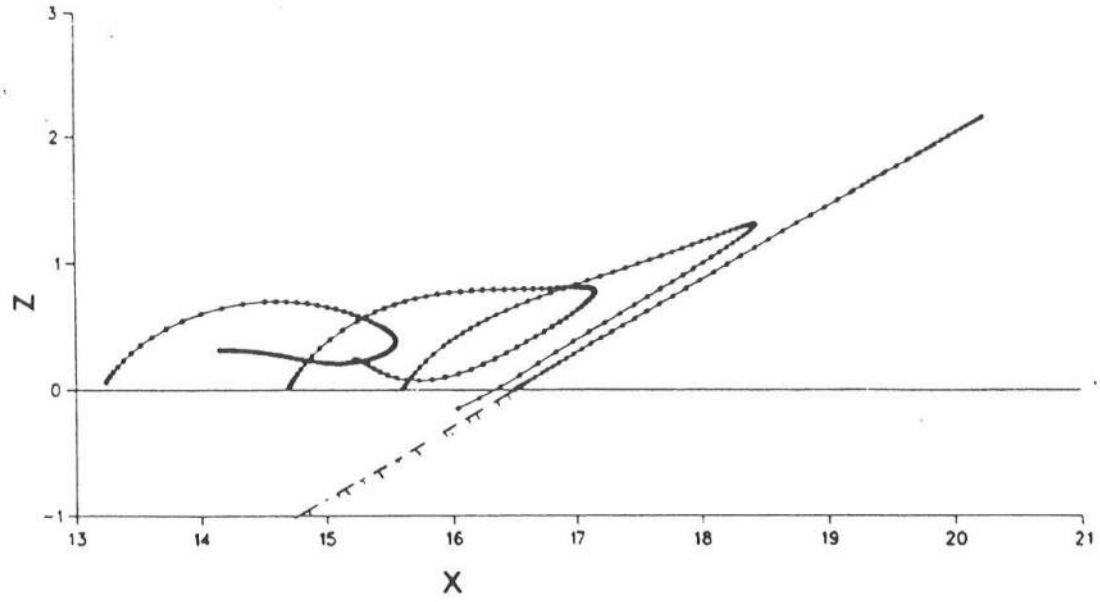

Figure 6.7: Particle trajectories due to the motion of a solitary wave of H=0.65 on a slope of 1:1.732. Trajectories are computable until the initiation of breaking during down-rush.

show the particle positions until breaking occurs on the slope during back-rush. It is observed that the excursion of a particle on the free surface is higher when the solitary wave propagates onto a slope than on a uniform depth though the net drift may be much less since the particle traverses back due to the return flow from the slope.

6.4 Interaction of Steep Solitary Waves With Slopes

Interaction of waves on slopes has been modeled by nonlinear shallow water theory, KdV theory and recently by the Boundary Integral Method. While considering high waves, significant differences are likely to exist between the approximate theories and the Boundary Integral modeling which satisfies the exact free surface conditions. In an earlier

work using boundary integral technique, Kim *et al.* (1983) studied runup of solitary waves. One of the serious handicaps in their model was the Eulerian description of the free surface which restricted its use only to moderate waves over relatively steep slopes. Recently, Grilli & Svendsen (1990) and Svendsen & Grilli (1990) have used BEM for studying interaction of solitary waves with slopes. They have carried out a detailed comparison of the surface profile with experimental results and the excellent agreement even to minor details has established high credibility for the method and the numerical scheme. In addition, runup predicted by their computation is found to be in good agreement. These computations have been mostly confined to moderate waves of height up to 0.5.

In the following, computations of very steep waves are considered on various slopes. Through the analysis in the previous section, the computational difficulties and the capabilities for modeling extremely high waves have been brought forth. It was shown that numerical error could be contained within a negligible level even for a wave of height 0.775 during propagation over a time length of 30. The phenomena studied here will be of considerably shorter duration. Of course, there are additional complexities while considering interaction with slope, one being the thin wedge of fluid formed between the free surface and the bottom. It is believed that the numerical treatment of the corner as described in chapter 3 significantly reduces the errors near the wedge. Thus, a basic framework for reliable computation is laid for the following investigations.

6.4.1 Computational Procedure

The computational domain is sketched in fig. 6.8. Though only plane slopes are considered in this work, the numerical scheme is not restricted to this. Free surface position and potential distribution at the initial time is once again specified from Tanaka's algorithm. The length of the uniform depth region and the position of the crest of the solitary wave are chosen such that the surface elevation at the shoreline is extremely small (typically of the order of 10^{-7} for high waves) at the initial time. This is done to keep the bottom "practically far away" so that the form corresponding to the steady solitary wave may be assumed unaltered by the bottom at the initial time. On the seaward side the domain is terminated several depths (typically $12 \sim 14$) away, where approximate normal

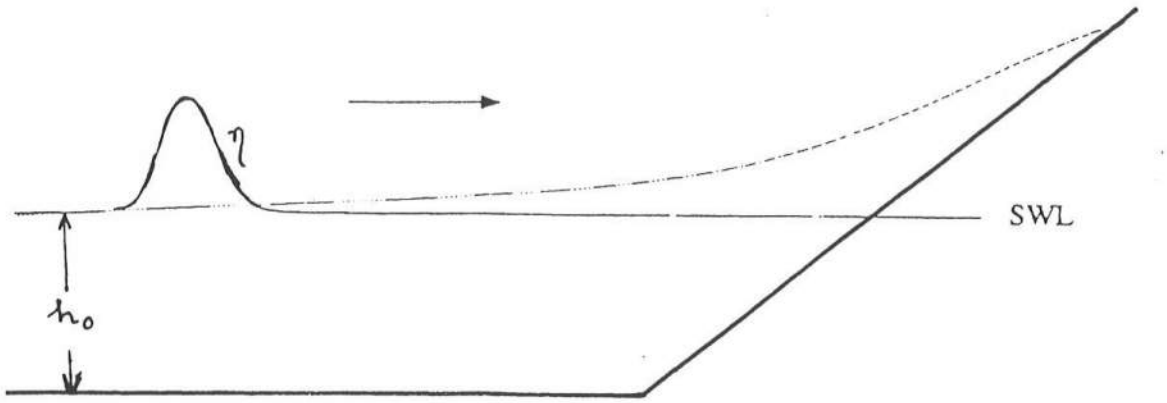

Figure 6.8: Sketch of the computational domain for the propagation of a solitary wave on to a slope.

flux can be formulated by KdV theory in terms of the surface profile η and η_{xx}. At a distance of $12 \sim 14\ h_0$, where h_0 is the uniform depth, from the crest the normal velocity on the lateral boundary is indeed very small and specifying zero flux may not cause much problem. However, the formulation used here reduces these undesirable oscillations significantly compared to specifying zero flux. With the horizontal velocity specified on this boundary, this boundary may be thought of as a wave generation boundary. New position of the shoreline is determined by the movement of the the free surface node at the intersection of the slope. This node has a velocity parallel to the slope and should be updated to a new position on the slope at each time step according to the free surface updating. Due to numerical errors, however, the updated position of this free surface particle may not lie exactly on the slope. The kinematic condition is therefore explicitly enforced by relocating the position of the particle to its projection on the slope. It is observed during computations of high waves that the magnitude of the displacement between the updated position and its projection is less than $10^{-2}\Delta s$, where Δs is the distance between two consecutive free surface nodes nearby. This difference is reduced along with an improved behavior of other quantities by using a smaller time step during runup.

6.4.2 Breaking of Solitary Waves on Slopes

A breaking criterion in terms of the local wave height to local water depth has often been sought based on the limiting wave on uniform depth. For the solitary wave the limiting height is 0.83. Another limit is given by 0.78. This corresponds to the wave of maximum energy and recent results by Tanaka (1986) have shown that growing normal modes which may give rise to instabilities exist for waves of height $H \geq 0.78$. Also, lab data show that the ratio of local breaking height and breaking depth of periodic waves on mild slopes falls around this value. On steeper slopes this value changes and in addition, depends substantially on both wave height and the slope. A compilation of the lab results on breaking height of periodic waves can be found in Dean and Dalrymple (1984).

In another approach, analytical solutions to runup of solitary waves on plane slopes have been presented by Gjevik & Pedersen (1981) and Synolakis (1987). These solutions are based on the approximate formulations of nonlinear shallow water theory. It has been clarified by Synolakis that there are two different criteria for breaking of solitary waves on slopes, one during uprush and another during during down-rush. The criterion for breaking during down-rush is due to Gjevik and that during uprush is due to Synolakis. These criteria are forwarded as

$$H_0^b = 0.8183(\cot\beta)^{-\frac{10}{9}} \qquad \text{during runup} \tag{6.8}$$

$$H_0^b = 0.479(\cot\beta)^{-\frac{10}{9}} \qquad \text{during rundown} \tag{6.9}$$

where H_0^b denotes the minimum wave height on the uniform depth that will break on the slope β. An important conclusion from (6.8) and (6.9) is that a solitary wave which rides up the slope without breaking may break during down-rush. An analytical index for breaking is helpful. However, the validity of such a formulation for even slightly steep slopes and steep waves may be in serious doubt since it is well-known that the nonlinear shallow water equation predicts early steepening and breaking of waves.

The present study presents results of computations of steep solitary waves on slopes satisfying the exact nonlinear free surface conditions. A sequence of figures showing the behavior of a solitary wave of height 0.75 during runup on different slopes is shown in fig. (6.9). The wave of this height breaks at the shore on a slope of 1 : 8 and the breaking

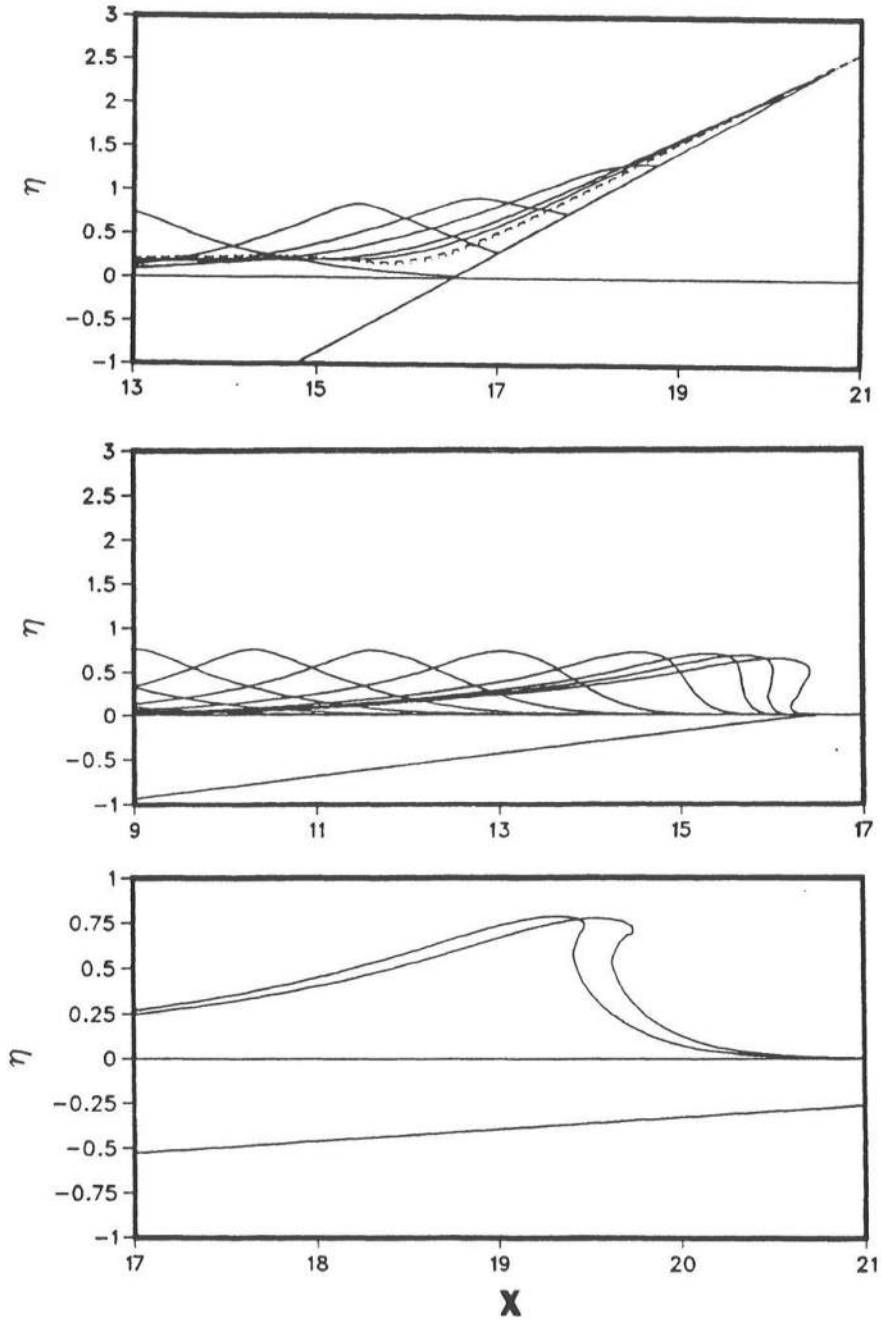

Figure 6.9: Propagation of a solitary wave of height 0.75 on slopes of $1:1.732$, $1:8$ and $1:15$ from top to bottom. Initial shoreline for the $1:15$ slope is at $x = 24$.

point moves seaward on a milder slope 1 : 15. On slopes 1 : 4 and 1 : 1.732, breaking does not occur during runup. Thus, if these results are accepted as valid (some experimental verification of the computed results are undertaken later), the breaking criterion (6.8) severely underpredicts the height of the solitary wave breaking on slopes during runup. A comprehensive comparison of breaking with (6.8) is not done, but an intuitive trend as predicted by the scattered computed data is shown in fig. (6.10). The computations thus

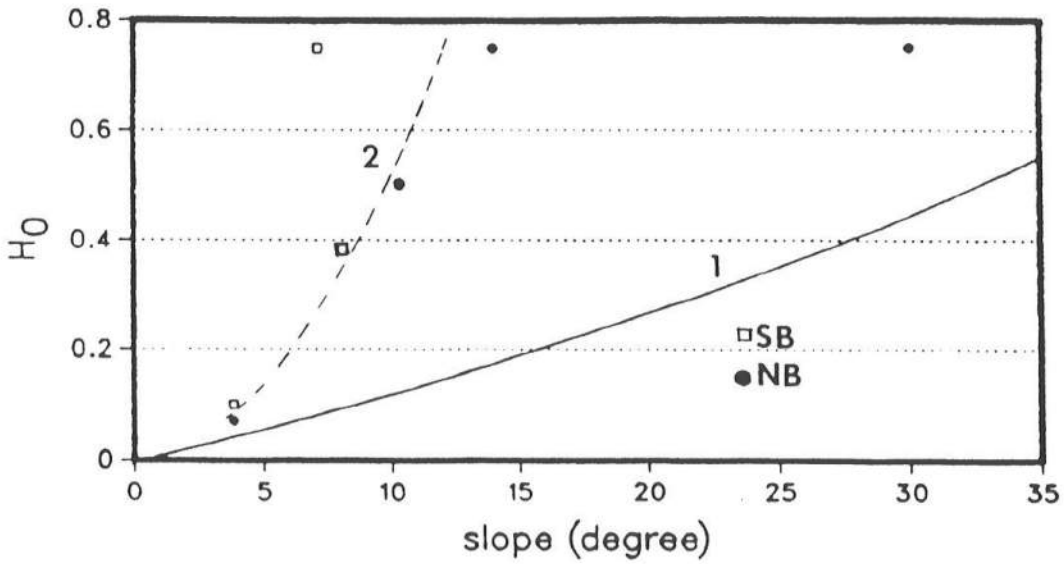

Figure 6.10: Breaking limit for solitary waves on slopes (during runup). Solid line [1] represents breaking by shallow water theory. NB denotes nonbreaking according to present computation and SB denotes breaking at the shore. Dotted line [2] approximately represents the limit obtained from the present computations.

indicate that no stable (on uniform depth) solitary wave will break on a slope steeper than about 12^0. This is in stark contrast to periodic waves which break on steeper slopes even at small height. A possible explanation for this may be found by looking at the behavior of solitary wave during rundown. Fig. (6.11) shows the rundown pattern of three different heights on a slope of 30^0. The wave of height 0.75 is seen earlier to runup this slope without breaking. In contrast, even a wave of height 0.6 is found to be breaking during rundown on this slope. This shows that solitary waves which runup the slope without

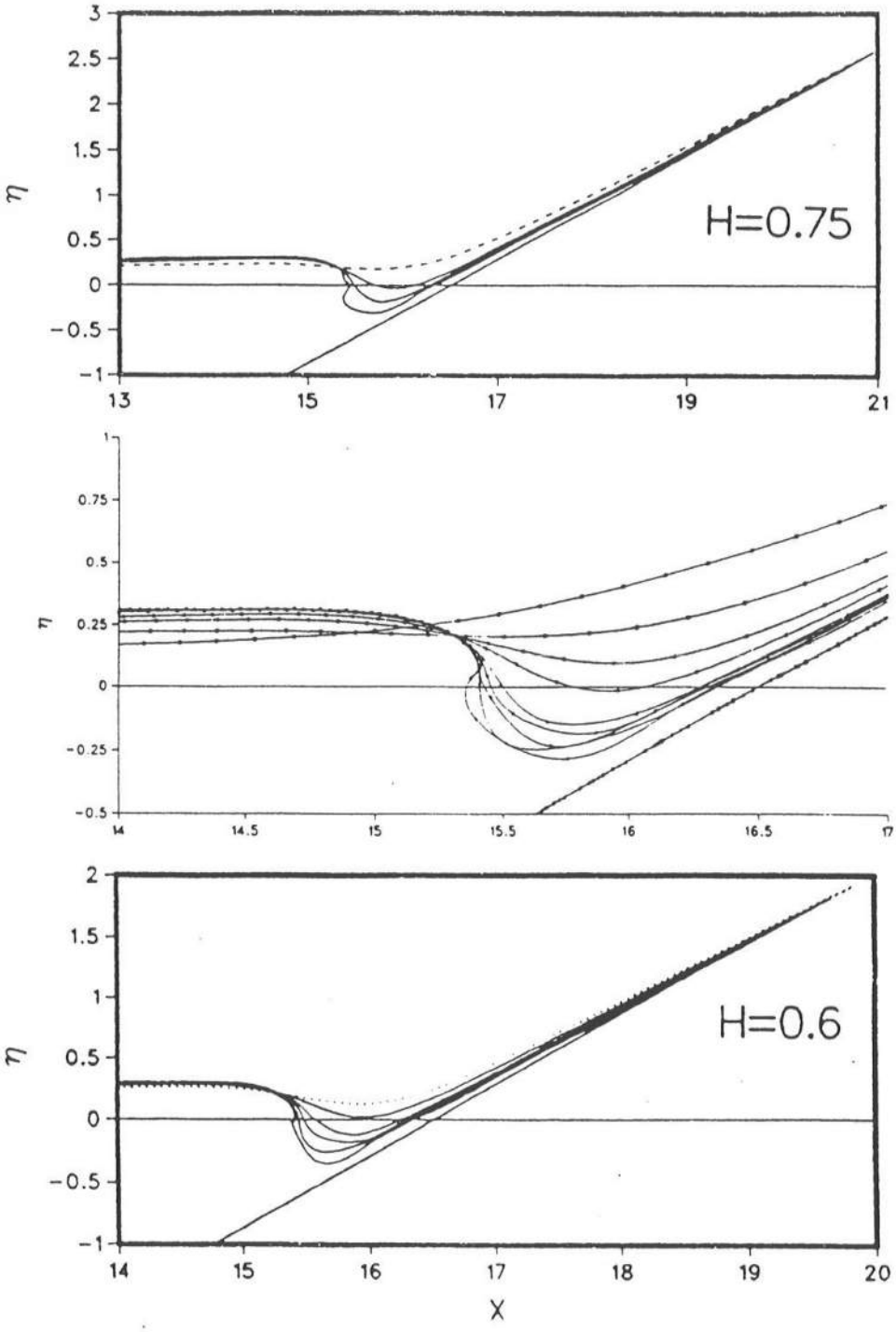

Figure 6.11: Breaking of solitary waves during rundown on a slope of 30^0. Top: $H = 0.75$, middle: $H = 0.65$, bottom: $H = 0.6$. Profiles are plotted after the maximum runup. The middle figure shows a magnified plot of the breaking region.

breaking may break during down-rush, confirming qualitatively the trend predicted by the equations (6.8) and (6.9). The breaking here is caused due to a faster stream meeting a slower mass of water down the slope and is a different mechanism than the overturning of the crest during forward motion of the wave. Study of a solitary wave on the slope thus shows the existence of two types of breaking, one marked by an overturning crest and the other by a faster downward stream.

In case of periodic waves both mechanisms of breaking are likely to exist and in fact, observed breaking may be caused due to an interaction of both. Thus, extrapolation of solitary wave results to periodic waves is difficult and can be in serious doubt.

6.4.3 Comparison With Experimental Data

Experimental guidance as to the validity of the computational results is sought from the results of Ippen and Kulin (1954) which includes waves up to a height of 0.7. Previous experiments by Beach Erosion Board (henceforth referred to as B. E. B.), as quoted by Ippen and Kulin, have indicated smooth ride-up for all heights tested on a slope of 1 : 9.5. Since, no information is available to the present author as to the highest wave tested in the B. E. B. experiments, a direct link between the computations and these experiments is not possible at this moment. The slopes in the experiments of Ippen and Kulin (henceforth referred to as "I & K") were chosen mild enough so that breaking during forward motion can be observed. The results include h_b/h_0, H_b/h_b and H_b/H_0 for waves of different height H_0 on the uniform depth. Comparisons will be provided for these parameters on a slope of 1 : 15. Identification of the breaking location is likely to be subjective. This may be one reason for the large scatter present in the experimental data besides the practical difficulties associated with the measurement of the surface elevation at the time of the breaking. "I & K" present a regression fit which can be given by the linear relation

$$\frac{h_b}{h_0} = 0.64 H_0 - 0.033 \qquad \text{for } 0.2 \geq H_0 \leq 0.7 \tag{6.10}$$

In order to reduce some uncertainties of comparison, the numerical profile for a specific initial wave height is considered breaking, at the instant the crest roughly reaches the

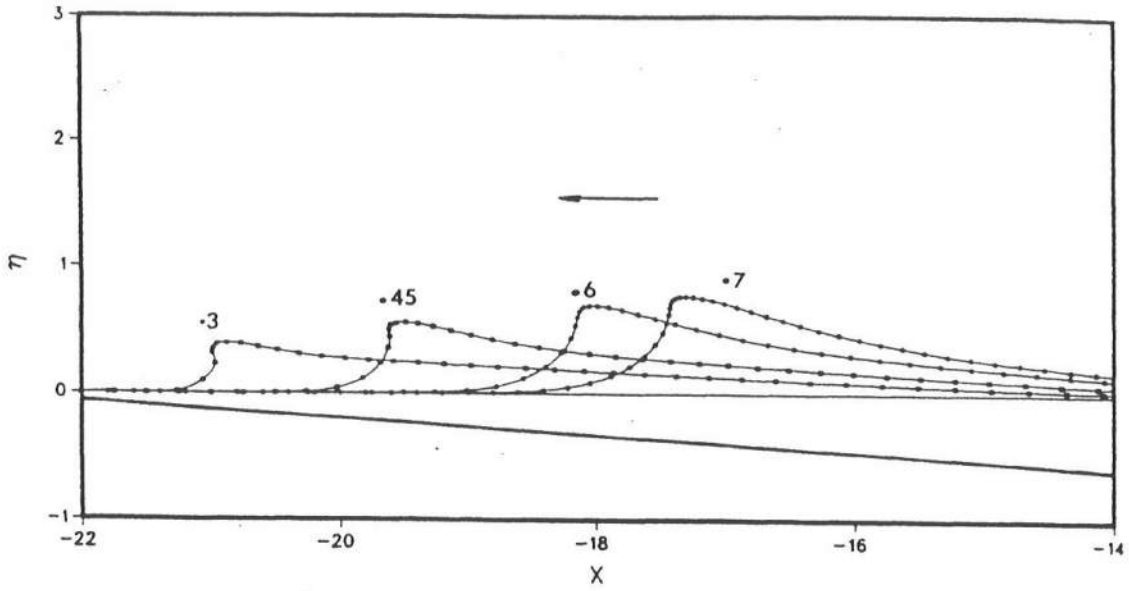

Figure 6.12: Breaking profiles on slope 1 : 15 for $H_0 = 0.3, 0.45, 0.6, 0.7$.

breaking depth, given by (6.10). Fig. 6.12 shows the numerical profile at this instant for each different height. In all cases of computation, the crest occurred at this location sometime before the computation was stopped due to unacceptable numerical oscillations. The crest height corresponding to this profile will now be fixed as the numerical H_b. The comparisons of H_b/h_b and H_b/H_0 between the numerical and the experimental values are shown in fig. (6.13). The numerical H_b/H_0 is about 4% higher than the experimental regression value. The agreement with the experiment may consequently be assumed satisfactory.

6.4.4 Particle Kinematics at Initiation of Breaking

As the wave runs up on the slope, the surface steepens and the velocity profile changes considerably from that under the permanent form. An accurate determination of correlations of the horizontal and vertical component of the wave velocity under an asymmetric profile is of critical significance in surf-zone modeling (Svendsen and Putrevu, 1990). In addition, knowledge of velocities and acceleration on the bottom under breaking

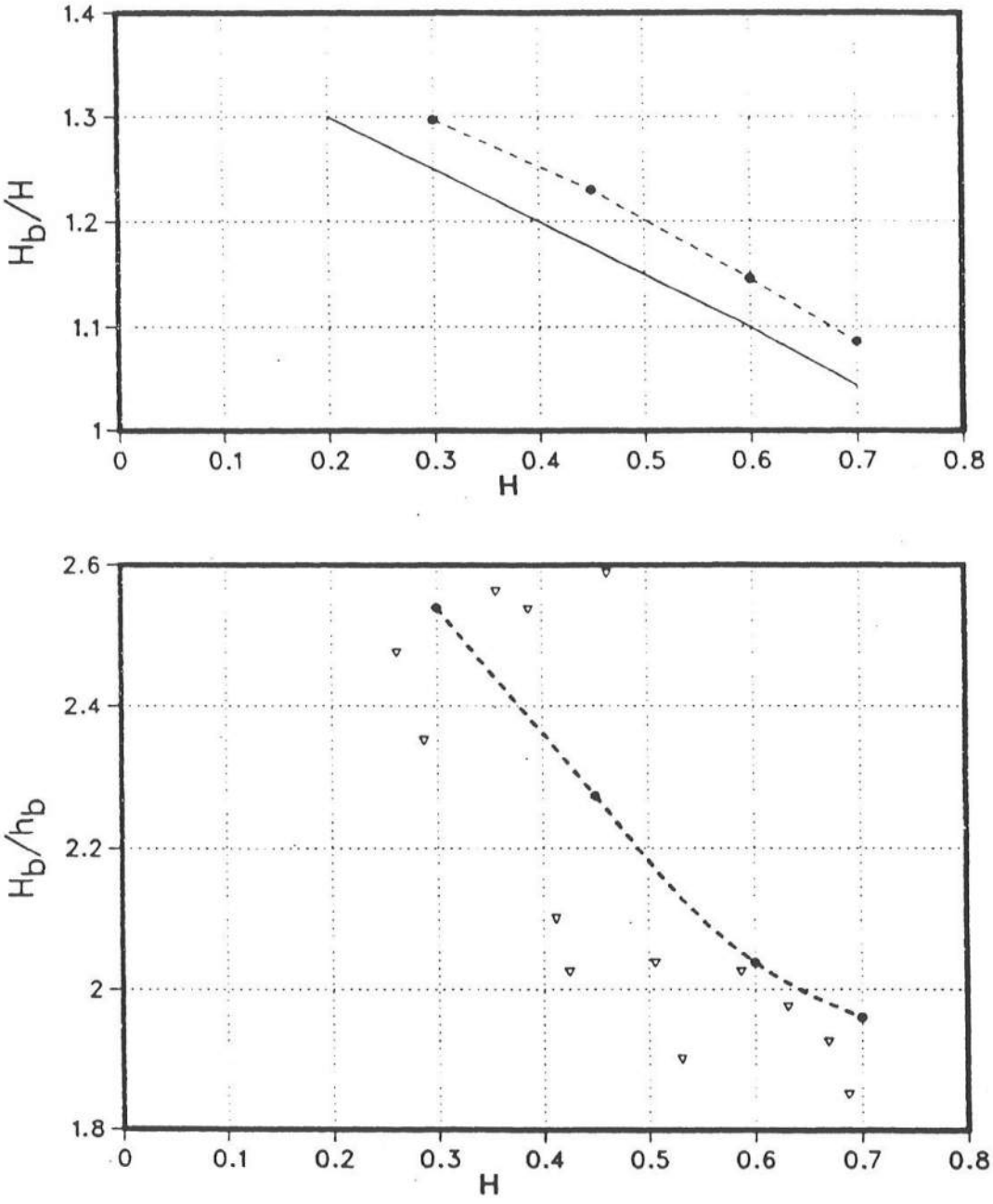

Figure 6.13: Comparison of the numerical and experimental breaking heights on slope 1 : 15. Top: the experimental line for H_b/H_0 (solid line) is obtained from regression of the scattered data points not shown in the plot. Bottom: scattered rings show the experimental data. The dashed lines show the computed results.

is important in the analysis of stability of armor units and sediment dislodgement. These are some of the motivations for the present work. The results are, however, not applicable to periodic waves since the analysis is confined only to solitary waves and only valid until the initiation of breaking, Peregrine *et al.* (1980) and New *et al.* (1985) have discussed particle velocities during overturning of waves. A summary of these works may also be found in Peregrine (1983). In their analysis, the computations are performed over a uniform bottom and breaking is caused by one of the following three mechanisms:

1. Energy fed in through pressure forcing to an initially small sine wave as in Longuet-Higgins (1976).

2. Evolution of an initially specified large sine wave as in Longuet-Higgins (1976).

3. Perturbation of depth of a uniform bottom during computation (New *et al.*, 1985)

Of these three, the last one has direct relevance only to very mild slopes where the bottom can be assumed to be locally uniform. They have remarked that large similarity exists in the kinematics of breaking independent of the mechanism creating it.

As noted earlier, breaking of a solitary wave on the beach can be caused by two different mechanisms, one during runup and the other during rundown. A direct comparison of the magnitude of the velocities in these two cases is out of question since the two events cannot be observed for the same wave height on the same slope. However, the velocity structure at the initiation of breaking due to the two different mechanisms can be compared.

In the numerical scheme, accurate determination of the flow field at points close to the boundary has been possible through the use of adaptive integration, which has been described in chapter 2. First, consider overturning of the surface during the forward motion of a wave of height 0.75 on a slope of 1 : 15. Fig. (6.14) shows the surface profile and horizontal velocity profile for this situation. The computation proceeds for a longer time than shown in the figure. Based on the variations of the flow quantities, computation of velocity and acceleration can be considered reliable at least up to this time. Two significant features of the velocity profile are the extremely high velocity near

the overturning tip and the sharp vertical variation of the horizontal velocity at sections near the front face. The maximum horizontal velocity shown in the figure is 1.74. In contrast, the phase velocity of a wave of height 0.775 (which is approximately the height of the plunging tip in the figure shown) is 1.2931. At 'section C', the horizontal velocity is almost uniform below the sea water level, rising sharply to two and half times this value at the free surface. The variation of vertical velocity at three sections is shown in fig. 6.15. The backward face is marked by large negative temporal acceleration (u_t, w_t), shown in fig. (6.16), which tends to cancel the large convective acceleration of a particle in this region. As a result of this the Lagrangian acceleration near the backward face is small. On the contrary, a small region under the jet on the forward face is seen to have large particle acceleration. These features are similar to those described in earlier works, even though the breaking here is caused by the slope.

However, the situation is remarkably different during breaking due to down-rush (fig. 6.17). During computation of rundown, the free surface nodes on the downward stream get far apart. This causes a fast degradation of the resolution making it difficult to follow the the overturning of the surface to a more advanced stage. However, some basic differences in the fluid kinematics from that of breaking during forward motion can be illustrated. This breaking is marked by the intrusion of the toe of the breaking face rather than the overturning of the crest tip and the maximum velocity occurs near the toe of the breaking face instead of the highest point. The velocity under the higher elevation is much weaker, compared to the wave velocity, being about 0.85 at 'section D' and 0.45 at 'section B'.

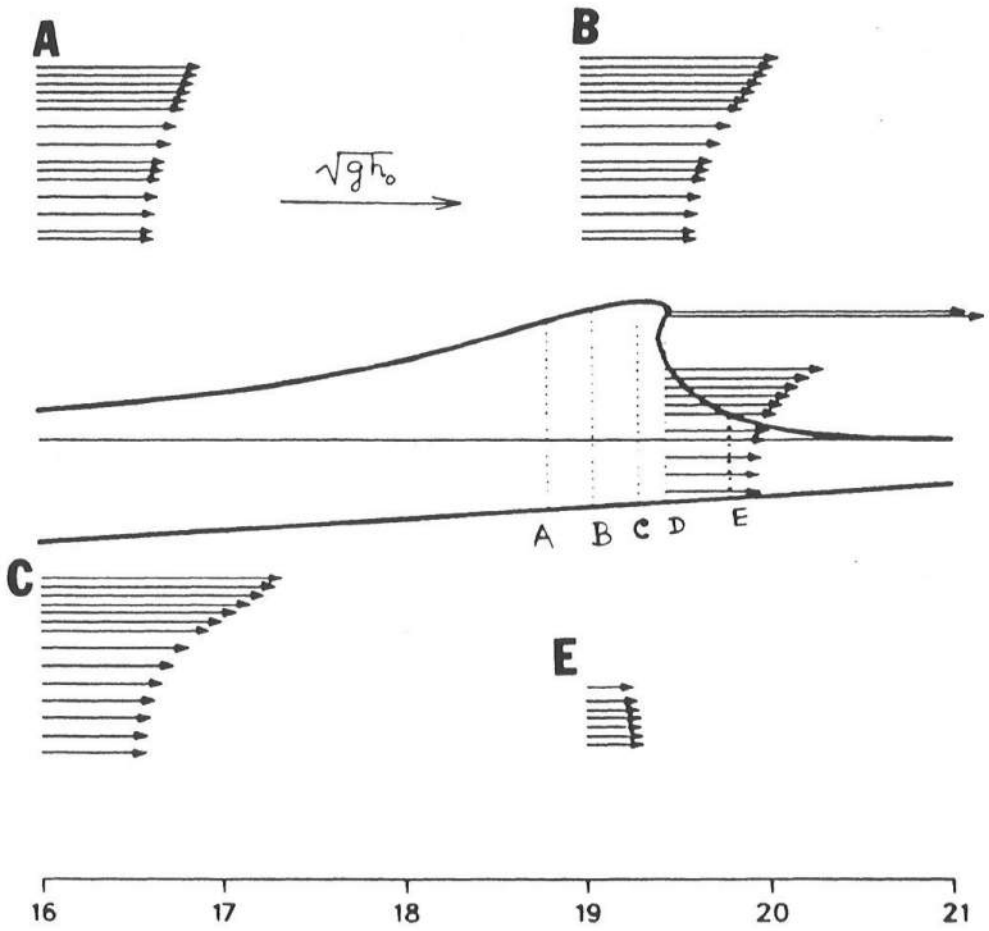

Figure 6.14: Vertical profile of horizontal velocity at the initiation of breaking during forward motion. $H_0 = 0.75$, slope=1:15. Sections A, B, C, D and E are at $x = 18.8$, 19.05, 19.3, 19.45, 19.8. Profiles at A, B, C and E are displaced. The arrows showing the velocity vectors originate from the points of calculation.

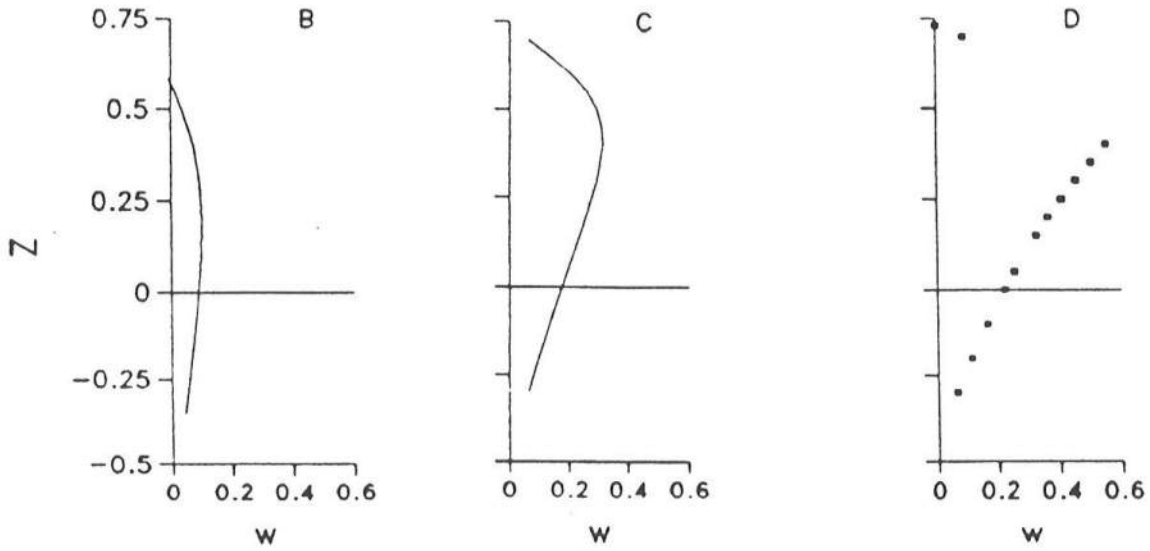

Figure 6.15: Vertical variation of vertical velocity at sections B, C and D under the overturning surface of a wave of $H = 0.75$ on slope 1:15 as shown in fig. 6.14. Due to the overturning surface, the entire vertical length from the bottom till the surface is not inside water at section D.

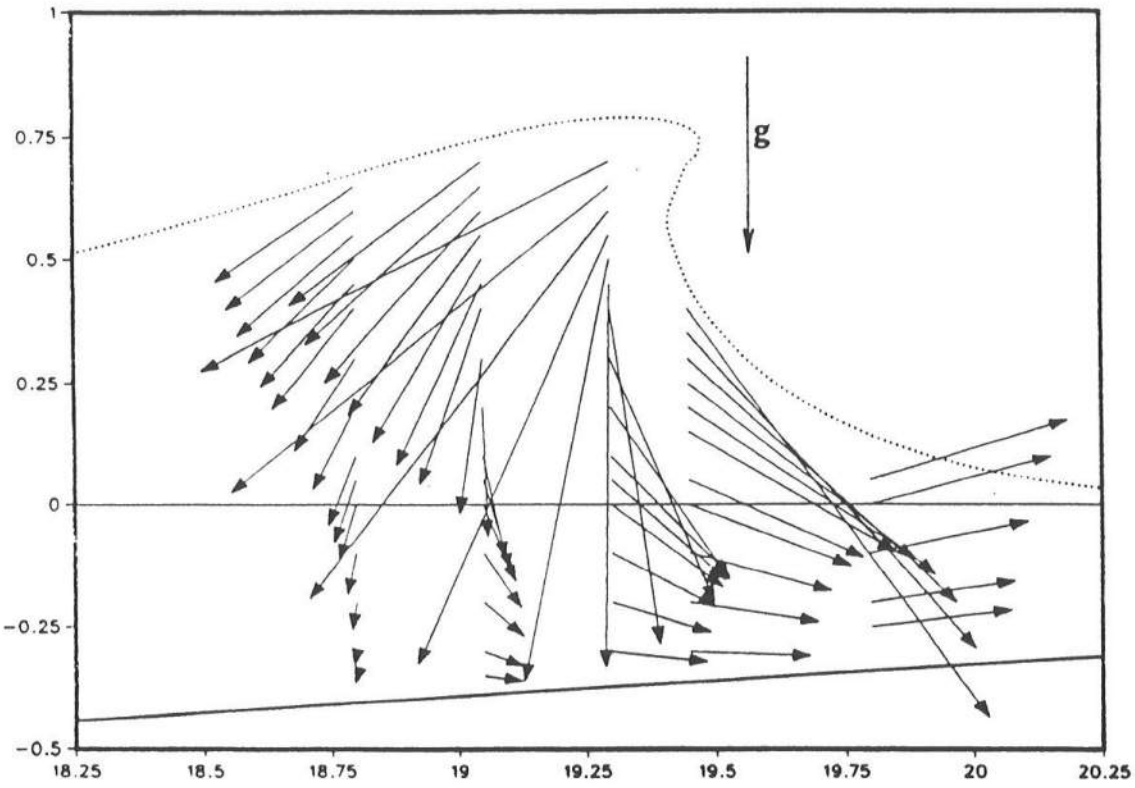

Figure 6.16: Eulerian acceleration vectors ($\partial u/\partial t$, $\partial w/\partial t$) at the initiation of breaking of a wave of $H = 0.75$ on slope $1 : 15$.

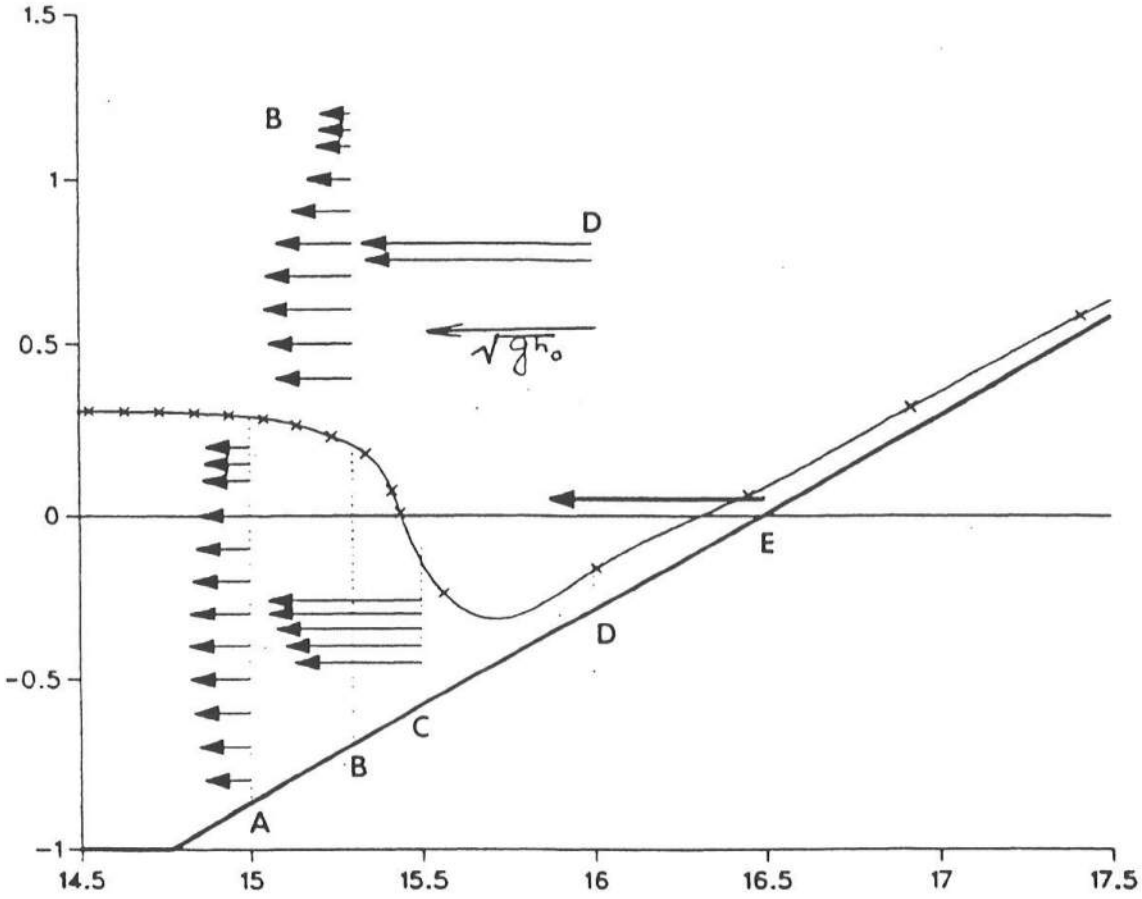

Figure 6.17: Vertical profile of horizontal velocity at the initiation of breaking during down-rush. $H = 0.6$, slope=1 : 1.732. Sections A, B, C, D and E are at $x = 15.0, 15.3, 15.5, 16.0, 16.5$. Profiles at B and D are displaced.

Chapter 7

SUMMARY AND CONCLUSIONS

In the present work we have considered several aspects of exact modeling of the free surface waves based on the potential theory through a boundary integral model formulated in the two-dimensional physical space. The three main parts of the work are

- new computational measures to achieve higher accuracy in a feasible and effective way in applications of the model to problems of highly nonlinear waves,
- physical and numerical aspects of modeling the lateral boundary conditions,
- application of the scheme to explain and quantify the relevant mechanisms in complex problems.

It is imperative to provide critical verifications of the scheme in order to establish the reliability of the approach for complicated unsteady processes. Direct validation of the computation of an unsteady process can be undertaken using well-documented experimental data if they are available. An alternative is to select problems carefully by which different features of the model can be critically judged against other well-established theories. In most of the verification studies presented here, estimation of the local accuracy has been presented instead of the global accuracy of the computations in terms of conservation of energy and volume. The former is a stringer test. Some of the test cases which have been undertaken in the previous chapters are

- propagation of a solitary wave of normalized height 0.775 providing verification of the steady propagation of an almost highest wave of permanent form,
- generation of irregular waves through the code, adapted to the linear theory in the time domain, compared to the prediction by a linear analytical wave maker theory,

- transient generation, propagation and radiation of steep, nonlinear periodic waves compared to the the stream function theory after the temporal evolution reaches the state of steady propagation,

- solution of a corner flow through the present boundary integral method.

These studies have identified specific needs for improvements. Some of the significant improvements are as follows.

Higher order discretization of the integral equation becomes critical to study steep waves in a large domain. However, higher order discretization based on the 'finite element' approach was found to give rise to instabilities for free surface motion. An alternative higher order element method, named 'mid-interval approximation' method, has been presented in chapter 2. This method has been found to be stable even for very steep waves. Though, only 4-node elements (cubic approximation) have been used in the present work extension to higher order requires only defining the shape functions of higher order polynomials.

Errors near a corner have been analyzed. This has been necessary for having selected to do the computation over the physical domain. An adaptive integration procedure has been introduced to reduce the errors and remove nonconvergence of the solution near a corner. This technique has also been used for accurate computation of the velocity and acceleration at interior points close to the boundary. A new treatment of the intersection involving a moving boundary or boundaries (*e.g.*, the free surface and a generation boundary) has been discussed. More important than the treatment, which may be improved further, is the identification of the problem and the demonstration of the sensitive nature of the intersection.

Applicability of the method to diverse problems depend to a large extent on the modeling of the lateral boundary conditions. The lateral conditions are sometimes clear; for example, if one has a reflecting wall or a sloping bottom. Otherwise, they are required to simulate the left-out region to a finite computational domain. The lateral boundaries intersect with the free surface. From the physical point, one has to ensure that the formulation of the lateral condition is appropriate with the initial condition on the free

surface and it produces the desired effect. By a proper treatment of the causes of the instabilities associated with the generation of waves in a boundary integral model, it has been possible to generate steep periodic waves with no smoothing over extended duration (propagation up to 10 wave periods has been studied). Numerical examples have been presented to show the utility of the model to analyze spatial modulation of the wave field in a physical wave tank under the fully nonlinear free surface conditions corresponding to the exact motion of the wave maker. Generation of an unmodulated field has been considered through two different procedures: specification of the velocity on a lateral boundary and a prescribed non-harmonic motion of a rigid wave maker.

An important aspect not discussed in the present work is the construction of a generation boundary which allows the reflected waves from a beach or a structure to be absorbed. This can be approached in two ways in a computational model. One path is to investigate the idea in Brorsen & Larsen (1987) of wave generation by sources coupled with a radiation boundary. The other is to modify the velocity of the wave maker or the specified velocity on the lateral boundary according to the approaching reflected wave. This problem is far more complex than it may seem. The idea presented by Brorsen and Larsen (1987) reduces the problem of finding an appropriate radiation condition only if the reflected waves do not interact or reflect back from the sources. In the second approach, the immediate problem is to identify the reflected waves in an arbitrary train of nonlinear signals.

A radiation boundary for the boundary integral model has been discussed in chapter 5. Though strictly exact only for waves of permanent form, the radiation formulation is seen to work satisfactorily for nearly regular and transient waves. The radiation boundary has been found to be stable in all cases tried. The intrinsic advantage of a radiation condition of the Sommerfeld type is that the phase velocity of an individual monochromatic train of waves varies only slightly with its time period in intermediate and shallow water. Thus the Sommerfeld condition may be treated as a valid first order approximation to the radiation of irregular waves over intermediate and shallow water. For a wave field comprising of long and relatively short waves, applicability of the radiation condition

can be improved by considering a sponge layer in combination with the Sommerfeld type of radiation condition. The problem of finding a radiation condition valid for irregular, nonlinear waves is difficult. It is, however, important to realize that a stable radiation condition, even if approximate, enhances the applicability of the model in an efficient way.

Finally, runup and breaking of solitary waves on slopes are studied in chapter 7. By using the model to study very steep waves, new results are obtained on the breaking of solitary waves. The available experimental data of Ippen & Kulin (1954) for waves of smaller height confirms the reliability of the computed results. It is found that the nonlinear shallow water theory grossly overpredicts the breaking of solitary waves on slightly steep slopes. Computed velocity and acceleration under the breaking surface have also been shown to aid further understanding of the breaking processes.

Due to the versatility and high accuracy of the scheme, application to different problems can be achieved with minor modifications. It is believed that the resolution necessary for studying irregular waves can be achieved by using higher order discretization and the interaction between different modes can be reliably modeled according to the exact free surface condition. Another important area of application is the wave-structure interaction. A submerged body of arbitrary shape can be included in the computational domain with no change. In principle, there are no restrictions for including a floating body though the computational procedure needs to be adapted for this purpose (the free surface is assumed to be uninterrupted in the present scheme). The intersection of the free surface and a floating body is similar to that of a rigid wave maker and the free surface. Thus, the process of wave generation studied in chapter 4 provides a preliminary step in the analysis of floating bodies.

A boundary integral model valid for a three-dimensional space has to be based on the Green's theorem or the generalized vortex method indicated by Baker *et al.* (1982). The complexity of the vortex method increases if the model is to be applicable to diverse problems. One may thus prefer the formulation based on the Green's theorem. The success of the present two-dimensional model is therefore a first step in the realization of a three-dimensional model. Higher order discretization based on the 'mid-interval approximation'

method, numerical treatment of the intersections and the radiation formulation developed here can be easily extended to the three-dimensional model.

BIBLIOGRAPHY

Abramowitz, M. and I. A. Stegun (1972). *Handbook of Mathematical Functions*, Dover Publications, New York.

Atkinson, K. A. (1976). *An Introduction to Numerical Analysis*, John Wiley and Sons, New York.

Baker, G. R., D. Meiron and S. A. Orszag (1981). Application of a generalized vortex method to nonlinear free-surface flows. *Proc. 3rd Intl. Conf. on Numerical Ship Hydrodynamics, Paris.* 163-176.

Baker, G. R., D. Meiron and S. A. Orszag (1982). Generalized vortex methods for free-surface flow problems. *J. Fluid Mech.*, 123: 477-501.

Banerjee, P. K. and R. Butterfield (1981). *Bundary Element Methods in Engineering Science*, McGraw-Hill Book Company, England.

Batchelor, G. K. (1967). *An Introduction to Fluid Dynamics*, Cambridge University Press, London, UK.

Behrendt, L. (1985). *A Finite Element for Water Wave Diffraction Including Boundary Absorption and Bottom Friction*, Inst. of Hydrodynamics and Hydraulic Eng., Technical University of Denmark, Denmark.

Boczar-Karakiewicz, B. (1972). Transformation of wave profiles in shallow water, Fourier analysis. *Archiwum Hydrotechniki*, 19(2): 197-209.

Brebbia, C. A. (1984). *The Boundary Element Method for Engineers*, Pentech Press, U. K.

Brebbia, C. A. and R. Butterfield (1978). Formal equivalence of direct and indirect boundary element methods. *Appl. Math. Modelling*, 2: 132-134.

Brorsen, M. and J. Larsen (1987). Source generation of nonlinear gravity waves with the boundary integral equation method. *Coastal Engineering*, 11: 93-113.

Chapman, D. (1985). Numerical treatment of cross-shelf open boundaries in a barotropic coastal ocean model. *J. Physical Oceanography*, 15 (8): 1060-1075.

Chwang, A. T. (1982). Nonlinear hydrodynamic pressure on an accelerating plate. *Phys. Fluids*, 26: 383-387.

Cointe, R. (1988). Remarks on the numerical treatment of the intersection point between a rigid body and free surface. *Proc. 3rd Intl. Workshop on Water Waves and Floating Bodies.*

Cointe, R. (1989). Quelques aspects de la simulation numérique d'un canal à houle. Thèse de Docteur de l'Ecole Nationale des Pontes et Chaussées.

Cointe, R. (1990). Numerical simulation of a wave channel. *Engineering Analysis with Boundary Elements.* 7(4): 167-177.

Cooker, M. J. (1990). A boundary integral method for water wave motion over irregular beds. *Engineering Analysis with Boundary Elements.* 7(4): 178-195.

Cooker, M., D. H. Peregrine, C. Vidal and J. W. Dold (1990). The interaction between a solitary wave and a submerged semi-circular cylinder. *J. Fluid Mech.*, 215: 1-22.

Dean, R. G. and R. A. Dalrymple (1984). *Water Wave Mechanics for Engineers and Scientists*, Prentice-Hall, New Jersey.

Dold, J. W. and D. H. Peregrine (1986). An efficient boundary-integral method for steep unsteady water waves, in *Numerical Methods for Fluid Dynamics II*, eds. K. W. Morton and M. J. Baines. 671-679. Clarendon Press, Oxford.

Dommermuth, D. G., D. K. Yue, W. M. Lin, R. J. Rapp, E. S. Chan and W. K. Melville (1988). Deep-water plunging breakers: a comparison between potential theory and experiments. *J. Fluid Mech.*, 189: 423-442.

Engquist, B. and A. Majda (1977). Absorbing boundary conditions for the numerical simulation of waves. *Mathematics of Computation*, 31: 629-651.

Fenton, J. (1972). A ninth-order solution for the solitary waves. *J. Fluid Mech.*, 53: 257-271.

Flick, R. E. and R. T. Guza (1980). Paddle generated waves in laboratoty channels. *J. Waterway, Port, Coastal and Ocean Div.*, 106: 79-97.

Giles, M. (1988). *Non-Reflecting Boundary Conditions for the Euler Equations.* CFDL-TR-88-1, Computational Fluid Dynamics Laboratory, MIT, Cambridge.

Gjevik, B. and G. Pedersen (1981). Runup of long waves on an inclined plane. *Technical Report*, Univ. of Oslo, Norway.

Goring, D. G. (1978). Tsunamis- the propagation of long waves onto a shelf. *Technical Report, KH-R-38*, Caltech, Pasadena.

Gradshteyn, I. S. and I. M. Ryzhik (1980). *Table of Integrals, Series and Products*, Academic Press, London.

Greenberg, M. D. (1978). *Foundations of Applied Mathematics*, Prentice-Hall, New Jersey.

Greenhow, M. and W. Lin (1983). Nonlinear free surface effects: Experiment and theory. Report No. 83-19, Massachusetts Institute of Technology.

Grilli, S. G., J. S. Skourup and I. A. Svendsen (1988). The modelling of highly nonlinear waves: A step toward the numerical wave tank. *Proc. 10th Intl. Conf. on Boundary Elements, Southampton, England.* 1: 549-564.

Grilli, S. G., J. S. Skourup and I. A. Svendsen (1989). An efficient boundary element method for nonlinear water waves. *Engineering Analysis with Boundary Elements.* 6(2): 97-107.

Grilli, S. G. and I. A. Svendsen (1989). Computation of nonlinear wave kinematics during propagation and runup on a slope. *Water Wave Kinematics.* Kluwer Academic Publisher, Dordrecht, The Netherlands.

Grilli, S. G., I. A. Svendsen and A. K. Otta (1990). Corner effects using BEM for nonlinear waves. *Proc. 5th Intl. Conf. on Boundary Element Technology*, Univ. of Delaware, Newark, USA.

Grilli, S. G. and I. A. Svendsen (1990). Corner problems and global accuracy in the boundary element solution of nonlinear wave flows. *Engineering Analysis with Boundary Elements.* 7(4): 178-195.

Hansen, J. B. and I. A. Svendsen (1974). Laboratory generation of waves of constant form. In *Proc. 14th Intl. Conf. on Coastal Engineering*, ASCE, 321-339.

Havelock, T. H. (1929). Forced surface waves on water. *Phil. Magazine*, Series 7: 569-576.

Hedley, M. and M. K. Yau (1988). Radiation boundary conditions in numerical modeling. *Monthly Weather Review*, 116: 1721-1736.

Hunter, J. K. and J. M. Vanden-Broeck (1983). Accurate computations for steep solitary waves. *J. Fluid Mech.*, 136: 63-71.

Ippen, A. T. and G. Kulin (1954). The shoaling and breaking of the solitary wave. In *Proc. 5th Conf. Coastal Engineering*, 27-54.

Isaacson, M. (1982). Nonlinear wave effects on fixed and floating bodies. *J. Fluid Mech.*, 120: 267-281.

Israeli, M. and S. A. Orszag (1981). Approximation of radiation boundary conditions. *J. Comp. Physics*, 41: 115-135.

Kantha, L. H., A. F. Blumberg and G. L. Mellor (1990). Computing phase speeds at open boundary. *J. Hydraulic Engineering*, 116: 592-597.

Kennard, E. H. (1949). Generation of surface waves by a moving partition. *Quart. Appl. Math.*, 7(3): 303-312.

Kim, S. K., P. L-F. Liu and J. A. Liggett (1983). Boundary integral equation solutions for solitary wave generation, propagation and runup. *Coastal Engineering*, 7: 299-317.

Kirby, J. (1989). A note on parabolic radiation boundary conditions. *Coastal Engineering*, 13: 211-218.

Klopman, G. (1987). Numerical simulation of breaking waves on steep slopes. In *Coastal Hydrodynamics*, ed. R. A. Dalrymple, ASCE, 317-327.

Lee, J-F., J-R. Kuo and C-P Lee (1990). Transient wavemaker theory. *J. Hydraulic Research*, 27: 651-663.

Lin, W. M., J. N. Newman and D. K. Yue (1984). Nonlinear forced motions of floating bodies. *Proc. 15th Symp. Naval Hydrodynamics.*

Longuet-Higgins, M. S. (1979). The trajectories of particles in steep, symmetric gravity waves. *J. Fluid Mech.*, 94: 497-517.

Longuet-Higgins, M. S. (1981). Trajectories of particles at the surface of steep waves. *J. Fluid Mech.*, 110: 239-247.

Longuet-Higgins, M. S. and E. D. Cokelet (1976). The deformation of steep surface waves on water. *Proc. R. Soc. Lond. A.*, 350: 1-26.

Longuet-Higgins, M. S. and J. D. Fenton (1974). On the mass, momentum, energy and circulation of a solitary wave-II. *Proc. R. Soc. Lond. A.*, 340: 471-493.

Madsen, O. S. (1971). On the generation of long waves. *J. Geophysical Research*, 76(36): 8672-8683.

Madsen, O. S., C. C. Mei and R. P. Savage (1970). The evolution of time-periodic long waves of finite amplitude. *J. Fluid Mech.*, 44: 195-208.

Milgram, J. H. (1970). Active Water Wave Absorbers. *J. Fluid Mech.*, 43: 845-859.

New, A L., P. McIver and D. H. Peregrine (1985). Computation of overturning waves. *J. Fluid Mech.*, 150: 233-251.

Orlanski, I. (1976). A simple boundary condition for unbounded hyperbolic flows. *J. Comp. Physics*, 21: 251-269.

Pennell, S. A. (1987). On a series expansion for the solitary wave. *J. Fluid Mech.*, 179: 557-561.

Pennell, S. A. and C. H. Su (1984). A seventeenth-order series expansion for the solitary wave. *J. Fluid Mech.*, 149: 431.

Peregrine, D. H. (1972). Flow due to a vertical plate moving in a channel. *Unpublished Note.*

Peregrine, D. H. (1983). Breaking waves on beaches. *Annual Review of Fluid Mechanics*, 15: 149-178.

Peregrine, D. H., E. D. Cokelet and P. McIver (1980). The fluid mechanics of waves approaching breaking. In *Proc. 17th Conf. Coastal Engineering*, 512-528.

Press, W. H., B. P. Flannery, S. A. Teukolsky and W. T. Vetterling (1986). *Numerical Recipes.* Cambridge University Press.

Rienecker, M. M. and J. D. Fenton (1981). A fourier approximation method steady water waves. *J. Fluid Mech.*, 104: 119-137.

Roberts, A. J. (1987). Transient free surface flows generated by a moving vertical plate. *Q. J. Mech. Appl. Math.*, 40: 129-158.

Romate, J. E. (1990). The numerical simulation of nonlinear gravity waves. *Engineering Analysis with Boundary Elements*, 7(4): 156-166.

Schultz, W. W. and S. W. Hong (1989). Solution of potential problems using an overdetermined complex boundary integral method. *J. Comp. Physics*, 84: 414-440.

Schwartz, L. W. (1974). Computer extension and analytic continuation of Stokes' expansion for gravity waves. *J. Fluid Mech.*, 62: 553-578.

Seo, S. N. and R. A. Dalrymple (1990). An efficient model for periodic overturning waves. *Engineering Analysis with Boundary Elements*, 7(4): 196-204.

Skourup, J. (1989). *Boundary Integral Equation Model for the Development of Nonlinear Water Waves and Their Interaction with Structures.* Series Paper 47, Tech. Univ. Denmark, Denmark.

Sommerfeld, A. (1949). *Partial Differential Equations in Physics.* Academic Press, New York.

Stansby, P. K. and A. Slaouti (1984). On nonlinear wave interaction with cylindrical bodies: A vortex sheet approach. *Appl. Ocean Research*, 6: 108-115.

Stroud, A. H. and D. Secrest (1966). *Gaussian Quadrature Formulas*, Prentice-Hall, New Jersey.

Svendsen, I. A. (1971). *Mixed boundary value problem for Laplace's equation in domain of arbitrary shape.* Prog. Rep. 23, 33-38. Coastal Engg. Lab., Tech. Univ. Denmark.

Svendsen, I. A. (1985). Physical Modelling of Water Waves. In *Physical Modelling in Coastal Engineering*, ed. R. A. Dalrymple. 13-47. A. A. Balkema, Rotterdam.

Svendsen, I. A. and S. G. Grilli (1990). Nonlinear waves on steep slopes. *J. Coastal Research*, 185-202.

Svendsen, I. A. and U. Putrevu (1991). *Personal Communication.*

Svendsen, I. A. and C. Staub (1981). Horizontal particle velocities in long waves. *J. Geophysical Research*, 86: 4138-4148.

Synolakis, C. E. (1987). The runup of solitary waves. *J. Fluid Mech.*, 185: 523-545.

Tanaka, M. 1986. The stability of solitary waves. *Physics of Fluids*, 29: 650-655.

Tanaka, M., J. W. Dold and D. H. Peregrine (1987). Instability and breaking of a solitary wave. *J. Fluid Mech.*, 185: 235-248.

Ursell, F., R. G. Dean and Y. S. Yu (1960). Forced small amplitude water waves: a comparison of theory and experiment. *J. Fluid Mech.*, 7: 32-52.

Vinje, T. and P. Brevig (1981). Numerical simulation of breaking waves. *Adv. Water Resources*, 4: 77-82.

Yen, S. M. and D. R. Hall (1981). Implementation of open boundary conditions for nonlinear free surface wave problems. In *Proc. 3rd Intl. Conf. on Numerical Ship Hydrodynamics*, 163-176, Paris.

Zaroodny, S. J. and M. D. Greenberg (1973). On a vortex sheet approach to the numerical calculation of water waves. *J. Comp. Physics*, 11: 440-446.

Zienkiewicz, O. C. and K. Morgan (1983). *Finite Elements and Approximation*, John Wiley & Sons, New York.

Zufiria, J. A. and P. G. Saffman (1986). The superharmonic instability of finite-amplitude surface waves on water of finite depth. *Stud. Appl. Maths*, 74: 259-266.